Title	Development of RF carpet type He gas cell and high-precision mass measurement of neutron-rich nuclei at around A = 50 - 60 with MRTOF
Author(s)	飯村, 俊
Citation	大阪大学, 2022, 博士論文
Version Type	VoR
URL	https://doi.org/10.18910/87814
rights	
Note	

Development of RF carpet type He gas cell and high-precision mass measurement of neutron-rich nuclei at around $A =$ 50 - 60 with MRTOF

Shun Iimura

Department of Physics, Graduate School of Science
Osaka University

Abstract

Mass measurements provide important information about nuclear structure, such as the magic number of nuclei. In the mass region far from β-stability line, "new" magic numbers have been discovered in neutron-rich nuclei and have become the subject of intense research in recent years. At RIBF BigRIPS, rare neutron-rich nuclei can be produced at the highest intensity in the world at present. The masses on these nuclei can be measured with high precision using a Multi-Reflection Time-of-Flight mass spectrograph (MRTOF), which can be analyzed in just about 10 milliseconds. However, there was a significant gap between the fast RI beam with several hundreds MeV/nucleon produced by the in-flight technique at RIBF and a slow RI beam with the energy of keV order or less, which is required by the mass measurement with MRTOF. As demonstrated in this thesis, we have overcome this difficulty by developing an RF carpet type helium Gas Cell (RFGC).

In the RFGC development, a newly designed electrode structure has been introduced and the transport efficiencies have been optimized at off-line tests by investigating several conditions. The RFGC has been installed at the downstream of the BigRIPS + ZeroDegree Spectrometer beamline, which has been combined with the MRTOF. On-line experiments were performed symbiotically with the in-beam γ-ray spectroscopy experiments (HiCARI campaign). The HiCARI campaign used fast RI beams of many kinds of nuclides, therefore RI beams with mass numbers from $A = 40$ to $A = 140$ were injected into the system. The performance of the RFGC was evaluated using this wide range of RI beams.

In this commissioning experiment, the masses of more than 70 nuclides have been measured. In particular, in the $A = 50\text{-}60$ region, a new analysis method has been introduced and the masses of 15 neutron-rich nuclei have been determined. Among them, the mass precisions of ^{55}Sc, ^{56}Ti, ^{58}Ti, ^{56}V, ^{57}V, ^{58}V, and ^{59}V have been significantly improved. We have evaluated our results by comparing with previously measured masses. With these updated masses, a detailed systematics of the neutron-separation energies has been studied and the shell structure of $N = 32$ and 34 in Sc, Ti and V isotopes has been discussed.

Table of Contents

1 Introduction

Atomic nuclei consist of protons and neutrons in a bound state by nuclear forces, and there are a wide mass range of nuclei, from light nuclei such as ^{1}H, which consists of only one proton, to superheavy nuclei such as ^{278}Nh, which was recently discovered in Japan [04Mo] and consists of 113 protons and 165 neutrons. There are about 3260 nuclei that have been experimentally confirmed to exist [11Sh], and it is estimated that there are more than 7000 nuclei in total, including those that have yet to be discovered [Ko05]. All isotopes are identified with the number of protons (Z) and neutrons (N) in the nuclear chart as shown in Figure 1.1.

Figure 1.1. Nuclear chart. Data are obtained from JAEA2018 [11Sh] and KTUY05 [05Ko].

The isotopes enclosed by the black and blue squares in Figure 1.1 are the 'stable' isotopes (i.e. they do not spontaneously undergo radioactive decay).
They follow $Z = N$ line until $Z = 20$, after which they move towards higher N (more neutrons in the nucleus). This is because more neutrons are needed to hold the nucleus together with relaxing the repulsion caused by the Coulomb force between the positively charged protons in the nucleus. The Coulomb force is the interaction that causes protons to repel each other,

and its range is infinite. The strong (nuclear) force, which binds nuclei together, is stronger than the repulsive Coulomb force, but its effective range is limited to scales within the size of the nucleus (about 1 fm).

Inside a nucleus, there is an internal nuclear structure of protons and neutrons, similar to the shell structure of an atom. The atomic shell model is used to describe the structure of orbital electrons around the nucleus, with electrons filling with individual energy levels to form a shell. A similar hypothesis is applied to the nucleus in the "nuclear shell model" [49Ma]. Closed shells are formed at the empirical "magic numbers" of 2, 8, 20, 28, 50, 82 and 126. The magic number of protons and neutrons is explained by the single-particle level in the mean field formed by all the nucleons, and the large gap (called the shell gap) makes the separation energy of protons and neutrons particularly high. This magic number is applicable to stable nuclei and nearby isotopes.

1.1 Magicity of neutron rich nuclei

In the recent years, improvements in accelerator facilities have made it possible to produce proton-rich and neutron-rich nuclei, which are located to be far from β-decay stability line, and to reveal the unique nuclear structure of unstable nuclei. In particular, the disappearance of empirical magic numbers (^{32}Mg ($N = 20$)[90Wa] have been observed first, subsequently the disappearance on ^{42}Si($N = 28$)[07Ba]) and ^{64}Cr($N = 40$)[08Ad]) and the appearance of new magic numbers on ^{52}Ca ($N = 32$)[85Hu, 13Wi] and ^{54}Ca ($N = 34$)[13St]) have been observed in the light nuclear regions, and this phenomenon is explained as "shell evolution", which has become one of the most important topics in nuclear physics.

1.1.1 r-process nucleosynthesis

On the other hand, nuclei with magic numbers play an important role in the process of nucleosynthesis.

How, where and when were the elements created? Figure 1.2 shows the abundance ratios of the elements in the solar system, as determined from spectroscopic observations of solar photospheres and the composition of meteorites. It is interesting to note that H is the most abundant and the heavier elements are generally less abundant. suggesting that the synthesis of the element started from protons in the universe. The lighter nuclei are thought to have

been produced by the Big-Bang and stellar nuclear fusion, up to Fe and Ni. The heavier nuclei beyond Fe and Ni are explained to have been created by neutron capture processes. The peaks at ^{88}Sr ($N = 50$), ^{138}Ba ($N = 82$) and ^{208}Pb ($N = 126$) are appeared on Fig. 1.2, which are generated through the slow neutron capture process (s-process). In the s-process, the nucleus captures neutrons on stable isotopes with Z. When the heaviest stable nucleus on the isotopic chain captures a neutron, the radioactive nucleus is produced and β-decays. Then, neutron capture can start on next (Z+1) isotopic chain. This process is supposed to have proceeded slowly over hundreds of millions of years to synthesize the heavy elements up to Pb. Red giant stars are one of the candidates for s-process. As nuclei with neutron magic number strongly bounds, the probability of the neutron capture is reduced. Therefore, and the process has to wait on the nuclei, leading to the formation of the peaks (around I, Te, and Pt) shown in the Fig.1.2.
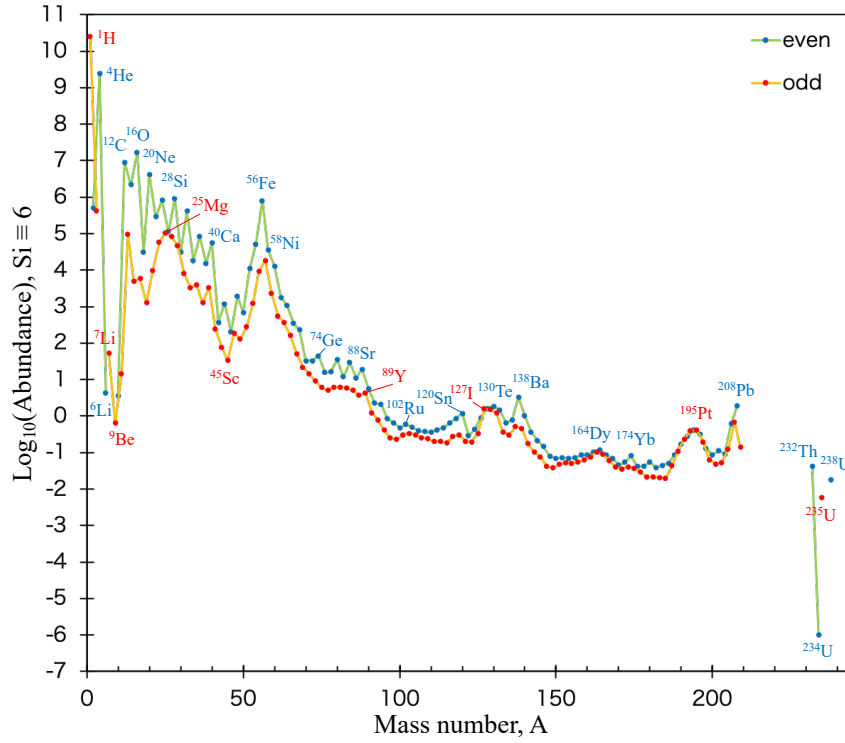

Figure 1.2. Element abundances of the isotopes as a function of mass number on the solar system. Data are obtained from [19Lo]. Blue and red circles indicate nuclides with even and odd mass-numbers, respectively.

The peaks located on to the left side of the s-process peaks (e.g., I, Te, and Pt) are considered to be produced with the 'rapid neutron capture process (r-process)', which proceeds in several seconds in extreme conditions such as supernova and neutron star merger. In high neutron density environments, the neutron capture rate exceeds the β-decay rate, and a lot of radioactive neutron-rich isotopes are produced. After the freezeout of neutron capture reactions, they become stable nuclei with β-decays. In particular, the nuclei with neutron magic number plays a significant role, Because the neutron capture reaction ceases, and the process has to wait for the β decay on a nucleus with a closed shell. Therefore, the r-process is considered to stagnate in neutron-rich nuclei at $N = 82$ and $N = 126$, called as 'waiting point nuclei', and these abundances after their β decay become high. The abundance of the elements depends strongly on the process and their pathways. The models describing the process must reproduce the observed abundances of stable isotopes. Such astrophysical models require the mass of the nuclides to be far from the β-stability line. As experimentally, it is difficult to produce such nuclei, and a mass model with strong predictive power is essential to understanding these processes. Therefore, the experimental data of masses are highly desirable as far away from β-stability line as possible, to enable definitive tests of the mass models and to provide an extended and reliable basis for tuning their parameters.

1.2　The mass of the nucleus

When a nucleus becomes to have a structure of shell closure, its ground state is stabilized relative to that of the neighboring isotopes. Therefore, binding energy measurements, such as precise mass measurements, are the most ideal indicator to search for a shell closed structure. A mass measurement, however, is technically challenging on nuclei far from the β-stability line because it requires the manipulation of the short-lived nucleus for a certain period of time and must be carried out with a high degree of accuracy.

The mass of an atomic nucleus is slightly less than the total mass of its constituent nucleons (the mass of all protons and neutrons). At the beginning of the last century, F. W. Aston [19As] discovered that there was a "mass defect" in the nucleus. He showed that this missing mass was converted into energy to hold the system together. This missing mass is called the binding energy B. The mass of a nucleus is then defined as

$$m(N, Z) = Nm_n + Zm_p - B(N, Z)/c^2 \qquad (1.1)$$

where m_n and m_p are the masses of the neutron and proton respectively, and $B(N, Z)$ is the binding energy of a nucleus with N neutrons and Z protons. To describe this binding energy, a simple model was proposed by von Weizsäcker in 1935 [35We]. This is the famous "liquid drop model". A nucleus has the characteristics of a liquid drop of incompressible nuclear matter. By improving this model, we were able to reproduce the gross features of the nuclear binding energy. Comparing the experimental masses with those of the droplet model, large discrepancies can be seen for several neutron and proton numbers. The nucleus does not only have the properties of a droplet. The discrepancies at the magic numbers indicate that the nuclei are more strongly bound at these numbers, suggesting an internal structure that coexists with the droplet picture.

1.2.1   Methods for mass measurement

There are two types of mass measurement technique: direct and indirect, mass measurement and energy measurement, respectively.

Indirect mass measurements

Indirect mass measurements rely on the Q-values of nuclear reactions and radioactive decays. The Q-value for nuclear decay is the difference in mass between the parent and daughter nuclides. To obtain a mass value from a nuclear decay, it is necessary to link the radioisotope to a known mass. This method has historically been the most common. However, in the case of unstable isotopes, the determination of the final mass can involve a long chain of decays, with possibly accumulation of the uncertainty on each subsequent decay. In addition, the continuous distribution of β-ray energies and also many branches from parent's ground state to daughter's states in β-decays makes it difficult to deduce accurate Q-values.

Direct mass measurements

The inertia mass could be measured more directly from ion motion in electromagnetic fields. The motion of ions (mass m, charge q) in a static magnetic field is followed by,

$$\frac{m}{q} = \frac{B\rho}{v},\tag{1.2}$$

due to the Lorentz force. It represents a flight through a uniform magnetic field B with radius of curvature ρ and ion velocity v. There are several major methods that apply this correlation; TOF-$B\rho$, Storage ring, and Penning trap.

TOF-$B\rho$ method is used in SHARAQ at RIKEN [12Ue], TOFI at LANL [85Wo], and SPEG at GANIL [01Sa]. These are in-flight mass spectrometers that measure mass by time-of-flight t and magnetic rigidity $B\rho$, as determined by the equation,

$$\frac{m}{q} = \frac{B\rho t}{\gamma L},\tag{1.3}$$

where L is the flight-length, γ is Lorentz factor. This is rearranged formula from [Eq. (1.2)]. Despite a low mass resolving power of $R_m (= m/\Delta m) \sim 10^4$, this method can access short lived nuclei with the order $T_{1/2} \sim 1$ µs. Therefore, the masses of unstable nuclei far from the valley of stability can be measured with this method.

Storage ring is used in Rare-RI-Ring at RIKEN [13Ya] and ESR at GSI [87Fr], and HIRFL-CSR at Lanzhou [09Wa], as one of the ways to increase mass resolving power by extending the flight-length. When operating in isochronous mass spectrometry (ISM) mode [00Ha], the revolution time of the ions orbiting in the storage ring is recorded and the mass is determined from the time-of-flight ratio to the reference ion. Despite the fast measurement speed of about 10 µs, it achieves a mass resolving power of $R_m \sim 10^5$. This method is also used for mass measurement of short-lived nuclei. Another method used in a storage ring is to use cold electrons to cool the ions orbiting in the ring and determine the mass from the orbital period of the ions using the Schottky method, so-called Schottky mass spectrometry (SMS) [05Li]. Although this method can increase the mass resolving power up to $R_m \sim 10^6$, it requires thousands of ions for the measurement and the applicable half-life is limited to $T_{1/2} \sim 5$ s due to the long cooling time.

Penning trap mass spectrometry is the presently most accurate method for measuring atomic mass. Relative mass uncertainties achieve 10^{-12} [16My] for stable nuclei and 10^{-9} for unstable nuclei. In Penning trap, a strong, uniform axial magnetic field is used to confine particles radially, and a quadrupole electric field is used to confine them axially. The motion of the ion confined in the magnetic field is given by [Eq. (1.4)] which is a transformation of [Eq. (1.2)],

$$\frac{m}{q} = \frac{B}{\omega_c}. \tag{1.4}$$

The measurement of the cyclotron frequency ω_c provides the atomic mass. Due to the time required for high-precision frequency measurements, it is suitable for measurements of nuclei with relatively long lifetimes down to 100 ms. Frequency measurements require at least several dozen ions and are not available for the small yield of ions. Penning traps have been installed at RI beam facilities all over the world. ISOLTRAP, the first Penning trap mass spectrometry for rare isotopes, was installed at the ISOLDE facility at CERN [96Bo] to provide high precision mass measurements of the ions produced by ISOL. Subsequently, Penning traps were installed at several other facilities, including JYFLTRAP at Jyväskylä [03Ko], CPT at Argonne National Laboratory [97Sa], LEBIT at NSCL/MSU [03Sc] and SHIP-TRAP at GSI [03Si].

Recently, a new type of on-line mass spectrometer has been developed that does not use a magnetic field: **MRTOF** (Multiple Reflection Time-Of-Flight) mass spectrograph [13Pl]. In this instrument, ions are injected into a trap formed by two electrostatic mirrors, which reflect the ions between them. Thanks to multiple reflections, the flight-length can become longer [90Wo]. During this time, the ions are separated according to their mass-to-charge ratio m/q. By measuring the time-of-flight t of the ions emitted from the trap to the detector, the m/q of the ions can be deduced from

$$\frac{m}{q} = 2V \left(\frac{t}{L} \right)^2, \tag{1.5}$$

where V is the effective average potential and L is the flight-length. MRTOF provides a long flight-length in a small space and high mass resolving power ($R_m > 10^5$). Measurement times are on the order of milli-second and this method can be applicable for a single ion. These instruments are ideal for mass measurements of exotic isotopes. Detailed operating principle is described in Chap. 2.2. MRTOF is available at both ISOL and in-flight facilities, e.g., GARIS at RIKEN [13It], ISOLTRAP at ISOLDE [12Wo], TITAN at TRIUMF [19An], FRS at GSI [15Di], CPT at Argonne [16Hi] and JYFLTRAP at Jyväskylä [20Pe].

1.3 $A = 50\text{-}60$ neutron rich nuclei

For high-precision measurements of neutron-rich nuclei, the superconducting Radioactive Isotope Beam Separator (BigRIPS) at RIBF/RIKEN is the best choice since it can provide most intense unstable nuclear beams in the world. Furthermore, these short-lived nuclei are suitable for quick and accurate mass measurement by using MRTOF. However, it is impossible to directly use the high-energy beams provided from BigRIPS with MRTOF. We have therefore developed a Radio-Frequency carpet-type ion guide Gas Cell (RFGC) in order to convert the high energy beam into a low-energy high-quality ion beam. In the autumn of 2020, the developed RFGC system was coupled to MRTOF and transported to operate behind the ZeroDegree spectrometer at the downstream of BigRIPS, where the continuous operation and testing of the combined system have been carried out. The system was ready for the online operation just before the start of the 2020 winter campaign of the in-beam γ-ray experiments [12Do] of the new HiCARI project [21Wi], which enables the first online commissioning of new our setup (called ZD-MRTOF) in parasitic operation. The 2020 HiCARI campaign had been carried out with five experiments in November and another two in December. During this commissioning run, mass measurements covering the mass number range from 40 to 140 were carried out. More than 70 neutron rich nuclei have been measured (see in Chap. 3.3.2). In particular, the author has responsible for the analysis of the masse measurement on neutron rich nuclei at around mass number $A = 50\text{–}60$, where new magic numbers ($N = 32, 34$) have been reported.

The first description of the new sub-shell $N = 32$ arose from a study of the β-decays of ^{53}K, ^{52}Ca and ^{53}Sc [85Hu]. This was followed by TOFI mass measurements [85Wo], which showed systematically strong binding energies at $N = 32$ [90Tu, 94Se, 98Ba]. β-decay spectroscopy studies at NSCL extended to the isotopes of Sc, Ti, V and Cr, providing further evidence for a sub-shell at $N = 32$ and suggested $N = 34$ sub-shell at ^{54}Ca [01Pr, 03Ma, 04Li]. In-beam γ spectroscopy of ^{54}Ca at RIKEN confirmed the $N = 34$ shell effect in ^{54}Ca, although on a smaller effect than the $N = 32$ effect in ^{52}Ca [13St], and which was later supported by mass spectrometry results [18Mi]. In the neighboring isotopic chains, mass spectrometry results and γ-ray studies have supported the persistence of $N = 32$ sub-shells in Ar, K and Sc isotopes [15Ro, 15Xu, 15St], and have suggested a rapid weakening of the $N = 34$ subshell gap in pf-shell nuclei at $Z > 20$ [17St]. On the other hand, low-lying excitation energies [99Ha, 03So, 08Ad, 09Ao], quadrupole collectivities [10Lj, 13Cr], and

atomic masses [12Na, 16Me, 18Mo] have been measured in Cr - Fe, and these experimental results consistently have suggested the deformation at around $N = 40$ on $Z = 24\text{-}26$, even though $N = 40$ is known as a sub-shell magic with spherical shape.

In this thesis, I present the development of RFGC combined with MRTOF (ZD-MRTOF). Through the development, we have demonstrated efficient and systematic mass measurements on neutron-rich nuclei provided from BigRIPS at RIKEN. Therefore I also present the evolution of the shell structure of the 34 sub-shells revealed by the systematic mass measurement of Sc, Ti, V, and Cr isotopes at around $N = 32, 34$ by using ZD-MRTOF.

2 Experimental method and devices

This chapter introduce an overview of the experimental method, the experimental devices and their operation principles.

2.1 Production of radioactive isotopes

Radioactive isotopes (RIs) can be produced via several kinds of nuclear reactions depending on the kinetic energy range. In the energy range close to the Coulomb barrier, fusion and transfer reactions can be useful, and in the higher energy range above the Fermi velocity, fragmentation and fission become the main sources of the production. Here we introduce the fragmentation and fission methods, which are suitable for the production of neutron-rich nuclei at the medium to heavy mass region.

Fragmentation of Projectiles and Targets

Unstable nuclei are produced with fragmentation due to scattering between nuclei above the Fermi energy of the nucleus. Fragmentation reaction is represented by the two-step process of abrasion-ablation [75Hu]. Fragments are kinematically concentrated in the forward direction, the energy and angular spread distributions are small, and the mean velocity of the projected fragment is close to that of primary beam [89Mo]. The fragments produced cover the full range of elements below the heavier collision partners [91Ga]. Projectile fragments are can be separated in-flight separators, while target fragments can be separated in ISOL (Isotope Separator On-Line) facilities.

Fission of Heavy Nuclei

Fission of heavy nuclei produces medium mass (around $A = 90$ and 160, uranium fission case) isotopes with neutron-rich side. The distribution of elements in the induced-fission products depends on the mass and excitation state of the fissile nucleus. Induced-fission reactions can be generated with low and high energy beams. In general, the phase space of fission products is much larger than that of fragmentation products. A target of heavier elements such as a uranium can be applied in ISOL facilities, while fast heavy ion beams and light element targets are used in in-flight separators. In latter case, the fission is called

as in-flight fission.

2.1.1 BigRIPS

For our experiment, the projectile fragmentation and in-flight fission were selected as the production reaction of neutron rich RIs of our interest. The RIs produced with high energy heavy ion beams (~ 350 MeV/nucleon) can be separated with an in-flight RI separator, named as BigRIPS, at RI beam factory (RIBF) of RIKEN [95Ge]. The BigRIPS is characterized by a large ion optical acceptance (Angular acceptance: 80 mrad/horizontal, 100 mrad/vertical), a two-stage structure, and excellent particle identification capability. It consists of 14 superconducting triplet quadrupoles (STQs) with large apertures and high magnetic fields, and six room-temperature dipoles with a bending angle of 30 degrees, as shown in Fig. 2.1. The beamline of BigRIPS has seven foci, denoted as F1-F7; the total length of BigRIPS is 78.2 m, and the length of the second stage (F3-F7) is 46.6 m long. The large acceptance allows not only the collection of projectile fragmentation of various heavy ion beams, but also the efficient collection of RIs produced with in-flight fission of ^{238}U beams. In-flight fission of fissile beams is known to be an excellent mechanism for producing a wide range of neutron-rich nuclei far from stability [97Be]. the BigRIPS is designed with a large acceptance to take advantage of the excellent features of in-flight fission. The first stage of BigRIPS generates and separates RI beams, and the second stage analyzes and identifies nuclei event by event. The momentum resolution of the second stage is designed to be high enough to identify the RI beam without measuring the total kinetic energy.
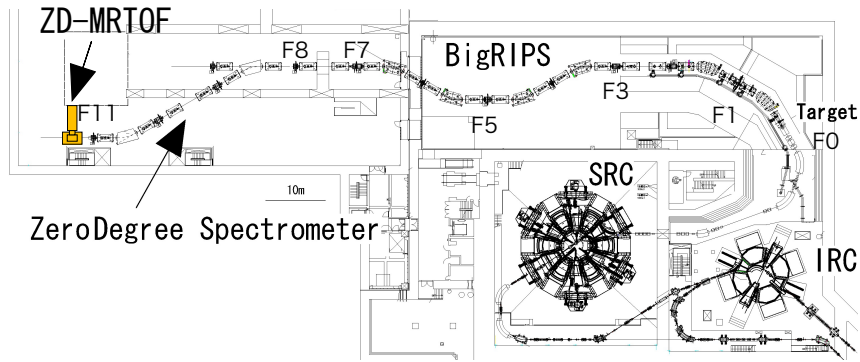

Figure 2.1. Schematic view of BigRIPS Separator and ZeroDegree Spectrometer [95Ge].

The focal plane chambers at the foci are equipped with beamline detectors (e.g. plastic scintillators, PPAC, and so on) and devices used to tune BigRIPS and to diagnose and identify particles in the RI beam. Particle identification is performed in the second stage of BigRIPS, which allows measurements under low background conditions. The particle identification method is based on the TOF-$B\rho$-ΔE method, in which the fragment's time of flight (TOF), magnetic rigidity ($B\rho$), and energy loss (ΔE) are measured with the beamline detectors to estimate the fragment's mass-to-charge ratio (A/Q) and atomic number (Z). TOF is measured between two thin plastic scintillators located at F3 and F7, and ΔE is measured at F7 using a multi-sampling ion chamber (MUSIC) or a stack of silicon detectors. The $B\rho$ is measured using two sets of position-sensitive parallel plate avalanche counters (PPAC) at F3 and F5, and in the second half of the second stage using the PPAC detectors at F5 and F7. Particle identification is confirmed by detecting delayed γ-rays emitted after the short-lived isomers decay in fragments by using a germanium detector at F7 or another focal plane downstream. By observing the γ-rays associated with isomers, unambiguous particle identification can be achieved. This technique is called isomer tagging [95Gr]. More details on particle identification can be found in references [08Oh] and [10Oh].

2.1.2   ZeroDegree spectrometer

The ZeroDegree spectrometer (ZDS) is located at the downstream of BigRIPS as shown in Fig. 2.1. It is designed as a two-bend achromatic system with anti-mirror symmetry, consisting of two dipoles and six STQs. The focal planes are labeled F8-F11 (Figure 2.1). The magnets of the ZDS are the same design as the magnets of the BigRIPS. The object point of ZDS is at F8, where the secondary target is located. The middle focus at F9 and F10 is momentum dispersive, and the final focus at F11 is fully achromatic. The same design of beamline detectors and devices as the BigRIPS are installed in the focal plane chambers. By using these detectors, PID was performed based on the TOF-$B\rho$-ΔE method as for BigRIPS, and beam purity and energies at F11 were obtained.

Our experimental device was installed at the downstream of the ZDS at F11. This made it possible to perform, e.g., in-beam experiments at F8 and to perform our experiment at F11 in parallel. A secondary RI beam that does not contribute to the reaction at F8 and also a tertiary RIs as the reaction residual at F8 are injected into our system. This method can allow us to perform two experiments during the same beam time, leading to efficient operation accelerator experiments in time constraints.

2.2 MRTOF

Continuing advances for multiple-reflection time-of-flight mass spectrograph (MRTOF) have played an vital role in the fast and accurate measurement of short-lived unstable nuclides produced at radioactive isotope beam facilities worldwide. Since its invention [90Wo], a lot of efforts have been devoted to improve the performance, leading to new opportunities such as the resolution and separation of isobars and isomeric states, and the precise measurement of previously unknown nuclear masses.

2.2.1 Principle

The basic principle of MRTOF is to reflect ions repeatedly between two (usually concentric) electrostatic ion mirrors, with the aim of focusing the ions to a TOF deflector with a TOF distribution as narrow as possible after their long flight path. To this end the ion optical aberrations be minimized, where one of the crucial ingredients for the MRTOF system is the distribution of mirror voltages forming a characteric shape. On one hand, these potentials are optimized to keep the radial ion optically small, which intuitively means that the radial expansion of the ion beam is kept as small as possible at all positions to approach a one-dimensional system. One important development in this context was the introduction of strong negative voltages at certain positions in the system (negative ion optical lens) [03Wo.], which also serves for radial confinement in general.

Here, we introduce how to connect 'atomic mass' with 'time-of-flight' in general. A scenario is given in which an ion starting from an initially field-free region with zero energy is accelerated by an accelerating voltage E_0 for a distance of δx_0 at the time origin and starts its flight. The initial kinetic energy K_0 of the ion with charge q is,

$$K_0 = qE_0\delta x_0. \tag{2.1}$$

In reality, switching transitions take a finite amount of time, however, it is argued in [20Ro] that the systematic uncertainties caused by them are negligible in this measurement.

In the case of an ion with initial energy K_0 at position x_0 traveling in the electrostatic field, the kinetic energy $K(x)$ at position x satisfies the following equation. The kinetic energy $K(x)$ at position x of an ion in one-dimensional motion in an electrostatic field

14

$E(x)$ under the initial conditions (kinetic energy K_0, position x_0) satisfies,

$$K(x) = K_0 + q \int_{x_0}^{x} E(x)\, dx. \tag{2.2}$$

The time-of-flight TOF to reach the detector can be calculated from the TOF integral from the initial position x_0 to the detector x:

$$
\begin{aligned}
TOF &= \int_{x_0}^{x} \frac{dx}{\sqrt{\dfrac{2K(x)}{m}}} \\
&= \int_{x_0}^{x} \frac{dx}{\sqrt{\dfrac{2\left\{ qE_0\delta x_0 + q\int_{x_0}^{x} E(x)\, dx \right\}}{m}}} \\
&= \sqrt{\frac{m}{q}} \times \int_{x_0}^{x} \frac{dx}{\sqrt{2\left\{ E_0\delta x_0 + \int_{x_0}^{x} E(x)\, dx \right\}}} \\
&= \sqrt{\frac{m}{q}} \times \text{Const.}.
\end{aligned}
\tag{2.3}
$$

Thus, the TOF is proportional to $\sqrt{m/q}$, and the constant component depends only on the geometry and the distribution of the electrostatic field. By measuring the time-of-flight of ions of well-known masses as reference at the same time, the constant component cancels out and the mass is determined by the following

$$m = q\frac{m_{ref}}{q_{ref}} \left(\frac{TOF}{TOF_{ref}} \right)^2, \tag{2.4}$$

where m_{ref}, q_{ref}, and TOF_{ref} are well-known mass, charge, and time-of-flight, respectively.

In the MRTOF system, the ions are reflected between a pair of electrostatic mirrors, which not only provide a long flight path, but also minimize the time spread of the ions. Designing the shape of the mirror potential to cancel out the energy dispersion of the ions, energy isochronous conditions can be achieved and mass resolving power can be maximized. A schematic of the energy isochronous behavior is shown in the lower part of Figure 2.2.
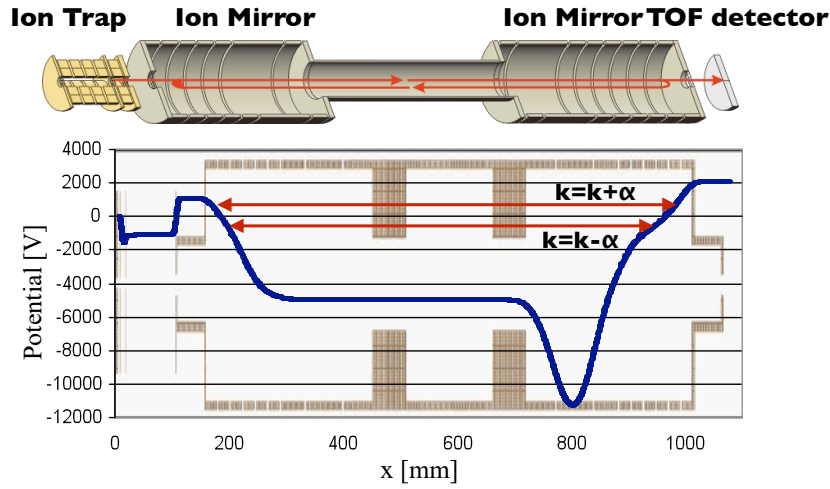
Figure 2.2. Schematic view of MRTOF in the upper panel, which consist of two ion mirrors and an ion trap and a TOF detector, and conceptual view of energy isochronous behavior in the lower panel inside the MRTOF.

The potential gradient of each mirror allows higher energy ions $(k + \alpha)$ to take a slightly longer path than lower energy ions $(k - \alpha)$, thus removing the energy dependence of the time-of-flight.

In order to manipulate ions in the MRTOF, the mirror switching technique is used as shown in Fig. 2.3. Firstly, the potential of injection mirror is switched off to allow ions to enter into the system (a), and when they are sufficiently far from injection mirror, the mirror potential is raised up to trap them. After sufficient numbers of the reflection of ions between two mirros (b, c), the ejection mirror potential is switched off and the ions are ejected from the MRTOF, passing through the mirror to the detector (d, e).
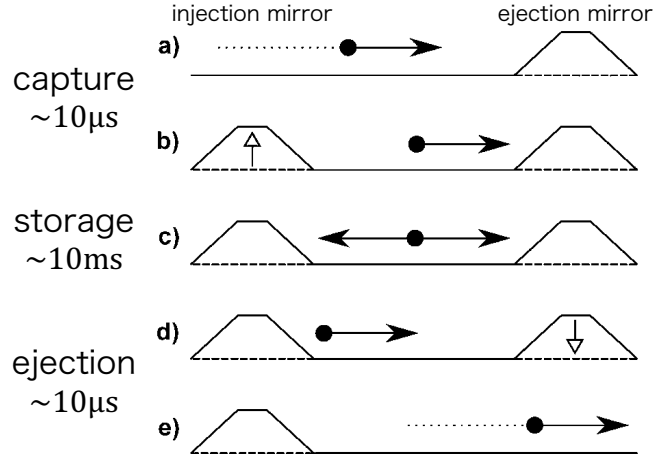
Figure 2.3. Schematic of mirror swithing method for MRTOF. The potential of the left and right mirrors are changed to allow to inject and eject of ions.

2.2.2 Device and Operation

New MRTOF mass spectrograph has been developed under a collaboration of RIKEN, KEK and so on. The new device has a similar design and operation to the setup in GARIS-II reported in [14Sc]. In the following, the current electrode configuration and measurement scheme are shown (See Fig. 2.4).
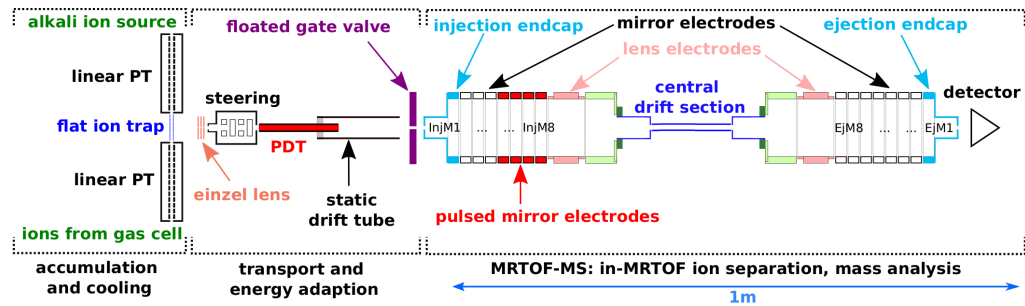

Figure 2.4. Electrode configuration of the MRTOF setup [22Ro].

Ions are continuously injected into a linear Paul trap (linear PT) for accumulation and bunching, and then transported to a planar Paul trap, called a flat ion trap (FT) for further collisional cooling in a dilute helium environment. The cooled ions are ejected vertically from the flat ion trap (TDC start) and accelerated in the transfer section between the flat ion

17

trap and the MRTOF. After passing through the lens and steering unit, a pulsed drift tube (PDT) is used to adapt the energy of the ions. The ions are trapped by fast switching of the bias of the first mirror electrode (injection end cap). They are reflected back and forth for a selected number of cycles and then released by fast switching of the bias of the last mirror electrode (ejection endcap). After leaving the ejection end cap, the ions reach a fast ion impact detector (ETP, MagneToF) and the impact time is digitized with a 100 ps precision multi-hit time-to-digital converter (FAST ComTech, MCS6).
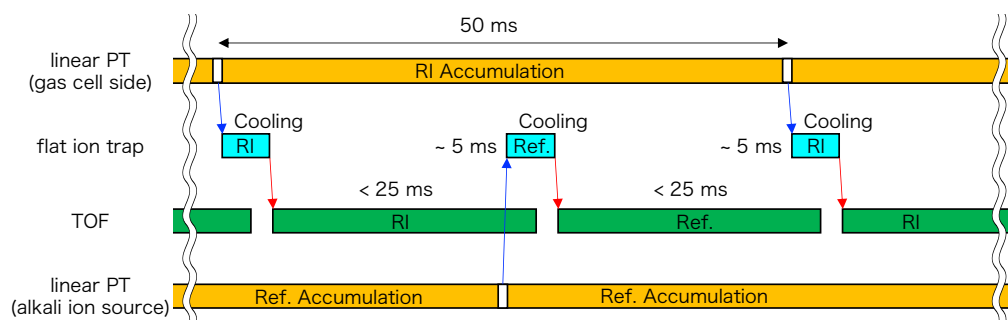

Figure 2.5. Conceptual view of time sequence of TOF measurements.

All time-of-flight mass spectrographs, including MRTOF, require at least one reference mass in order to derive unknown masses from measured time-of-flight and to track time-of-flight shift (called as TOF drift) in high precision mass measurement instruments. Ideally, the reference mass should be an isobar of the chemical species of interest to avoid higher order effects associated with TOF and mass. Furthermore, the intensity of the reference ions must be high enough to follow the TOF drift. For on-line experiments, such a suitable reference ion is not always available, therefore an external ion source is required ("alkali ion source" in Fig. 2.4). Thermal ion sources that can provide alkali ions and alkaline earth ions (Li+, Na+, K+, Ca+, Rb+, Cs+) are used. The flat ion trap allows ions to be injected from the opposite side of the analyte to the ion injection, as shown in Fig. 2.4. Figure 2.5 shows the time sequence for TOF measurements of ions from the gas cell and from the reference ion source. Ions including radioactive isotopes from the gas cell are accumulated in linear PT in 50 ms, and are ejected to the FT. And then, the ions are injected into MRTOF and the TOFs are measured in 25 ms period (or less). After completing the TOF measurement of ions from the gas cell, ions from the reference ion source are injected into MRTOF and the TOFs are measured subsequently. Even during the TOF measurements of

both ions from the gas cell and from the reference ion source, ions from the gas cell are accumulated continuously in the linear PT as shown in Fig. 2.5.

The MRTOF, operating by above-mentioned mechanism, requires the analyte to be injected into the linear PT with a low energy beam (less than few eV/q). However, BigRIPS beams have high energy (several hundred MeV/nucleon), therefore RFGC is introduced to convert them to high quality and low energy beams.

2.3 RFGC

BigRIPS can produce a wide range of unstable nuclei, while the RI beam has high energy (~ 200 MeV/nucleon) and has a large energy spread in phase space. On the other hand, slow RI beams with low energy (~ several keV) and small emittance are essential to measure the mass of nuclei with high precision using the MRTOF. We have introduced the Radio Frequency carpet type helium Gas Cell (RFGC), which converts a high-energy beam into a low-energy and high-quality beam. The RFGC consists of an energy degrader and helium gas catcher cell as the stage for stopping a high energy beam, and RF carpets and a quadrupole RF ion guide (QPIG) as the stage for the transportation and extraction of low energy ion beam (see Figure 2.6).
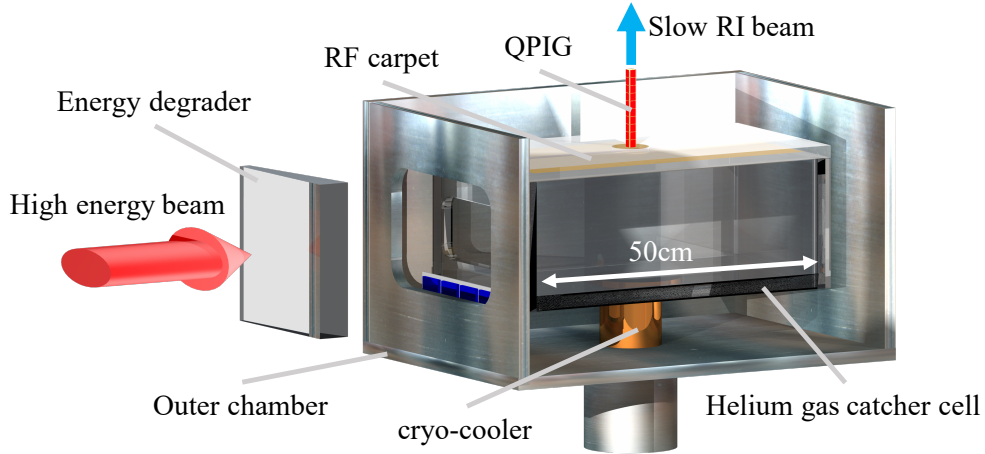

Figure 2.6. Schematic view of RFGC.

2.3.1 Degrader

The typical beam energy behind ZDS is 100-200 MeV/nucleon. In order to stop such relativistic energy fast beams with relativistic energy in the He buffer gas, a degrader is essential, and the thickness must be precisely optimized. Therefore, a rotatable degrader system has been introduced. A SUS or Al degrader with a thickness of 0.1-7.0 mm has been installed with a stepping motor in front of the outer chamber as shown in Fig 2.7. The stepping motor has a high resolution of 0.0072 degree per a step, allowing the fine tuning of the effective degrader thickness.
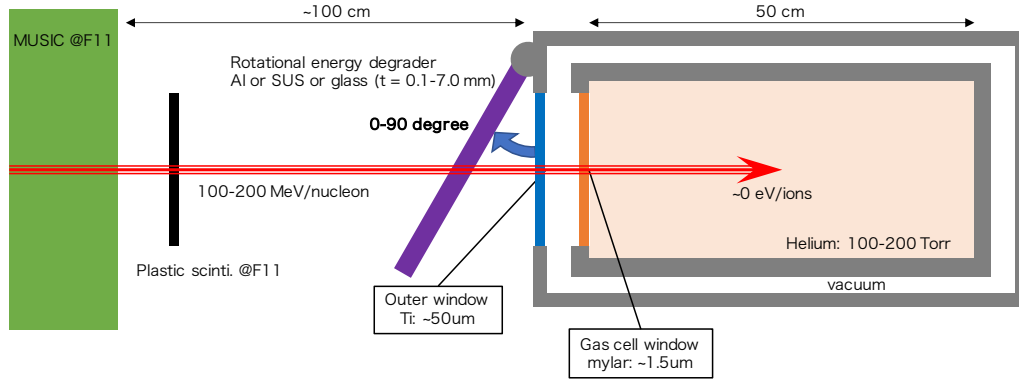
Figure 2.7. Schematic for energy degrader system.

2.3.2 Ion survival in buffer gas

The RI beams provided with BigRIPS is delivered to F11 with a certain charge state. In the process of decelerating to thermal energy in a material, they pick up electrons from the material and their charge state changes toward neutral. Finally, the charge state of the thermalized ions is determined by the competition with the ionization energy of the surrounding material. By using helium gas, it is possible to increase the probability of survival as an ion without neutralization. For example, the literature [06De] shows that the survival probability of Rn ions in helium gas is up to about 30%.

2.3.3 RF ion guide

In this section, we introduce a manipulation technique for transporting and extracting ions thermalized in helium gas. Normally, ions move toward electrodes with low electric potential and are adsorbed there. They cannot be kept in space (this restriction is known as Earnshaw's theorem). However, it can be trapped in space by using magnetostatic (Penning trap) or dynamic electric fields (Paul trap). In particular, the Paul trap, which can be implemented only with electrodes and a power supply, has advantages of the easy operation and space saving.

2.3.3.1 *Paul trap*

W. Paul invented a method to stably trap ions near the center to four electrodes, of applying a high-frequency electric field with mutually inverted phase as shown in the Fig. 2.8. The equation of motion of the ions (mass m, charge q) in buffer gas is given by

$$m\ddot{\boldsymbol{r}} + \frac{q}{\mu}\dot{\boldsymbol{r}} = -q\nabla\Phi(\boldsymbol{r},t), \tag{2.5}$$

where $\mu = \mu_0 P_0/P$ is the ion mobility in gas at pressure P, P_0 is the atmospheric pressure, μ_0 is the ion mobility under P_0 and Φ is the potential. Introducing the gas dumping factor $D = q/\mu m$, [Eq. (2.5)] is

$$\ddot{\boldsymbol{r}} + D\dot{\boldsymbol{r}} + \frac{q}{m}\nabla\Phi = 0. \tag{2.6}$$

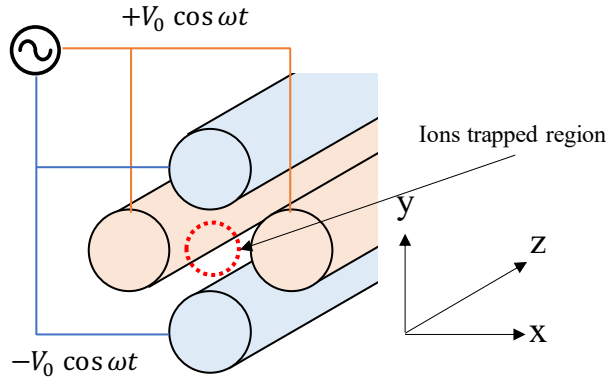The RF electric field of Paul trap can be approximated as an RF quadrupole electric field, as shown in Fig. 2.8.

Figure 2.8. Cross-sectional view of Linier Paul trap (Quadruple RF ion trap)

Then, the quadrupole potential Φ and field $\boldsymbol{E}$ is approximated by

$$\Phi(\boldsymbol{r},t) = V_0 \frac{x^2 - y^2}{r_0{}^2}\cos\omega t \tag{2.7}$$

$$\boldsymbol{E}(\boldsymbol{r},t) = -\nabla\Phi = \frac{V_0}{r_0{}^2}\begin{pmatrix} -x \\ y \end{pmatrix}\cos\omega t = \boldsymbol{E}(\boldsymbol{r})\cos\omega t\,, \tag{2.8}$$

where r_0 is radius of a circle inscribed inside the quadrupole electrodes.

The effective electric field is estimated by using the pseudo-potential in the quadrupole field as shown in Fig. 2.8. Divide the motion of an ion into a mean-motion part and a micro-vibration term,

$$\boldsymbol{r} = \tilde{\boldsymbol{r}}(t) + \boldsymbol{\rho}(t) = \tilde{\boldsymbol{r}}(t) + \alpha\boldsymbol{E}(\boldsymbol{r})\cos(\omega t + \beta)\,, \tag{2.9}$$

where constant α is determined by substituting [Eq. (2.9)] for [Eq. (2.6)]. Thus, micro-vibration term is expressed by

$$\boldsymbol{\rho}(t) = -\frac{q}{m\omega} \frac{\boldsymbol{E}(\boldsymbol{r})}{\sqrt{\omega^2 + D^2}} \cos(\omega t + \beta), \tag{2.10}$$

where β is a delay component caused by gas dumping and satisfies

$$\tan\beta = D. \tag{2.11}$$

Time-average force over one period due to the RF electric field gradient is

$$\tilde{\boldsymbol{F}}(\tilde{\boldsymbol{r}}) = q\langle \boldsymbol{E}(\tilde{\boldsymbol{r}})\cos\omega t + \boldsymbol{\rho}(t)\,\nabla\boldsymbol{E}(\tilde{\boldsymbol{r}})\cos\omega t\rangle_{\text{time average}}$$

$$= -\nabla\boldsymbol{E}^2(\tilde{\boldsymbol{r}})\frac{q^2}{4m}\frac{1}{\omega^2 + D^2}. \tag{2.12}$$

If we regard the time-averaged force as caused by the pseudo-potential U_{eff},

$$U_{\text{eff}}(\tilde{\boldsymbol{r}}) = \frac{q^2}{4m}\frac{1}{\omega^2 + D^2}\boldsymbol{E}^2(\tilde{\boldsymbol{r}}), \tag{2.13}$$

Substituting [Eq. (2.8)], we get,

$$U_{\text{eff}}(\tilde{\boldsymbol{r}}) = \frac{q^2 V_0{}^2}{4m(\omega^2 + D^2)r_0{}^2}\left(\frac{r}{r_0}\right)^2. \tag{2.14}$$

The parabolic potential traps ions at around the center of the Paul trap. This pseudo-potential method was introduced by H. Dehmelt in the [67De].

2.3.3.2 RF carpet

In the case of the quadrupole linear Paul trap, the pseudopotential energy is given by [Eq. (2.14)], and when this is extended to multipoles ($2n$-poles, see Fig. 2.9), the pseudopotential energy $U_{\text{eff}}(r)$ is

$$U_{\text{eff}}(r) = \frac{q^2 n^2 V_0{}^2}{4m(\omega^2 + D^2)r_0{}^2}\left(\frac{r}{r_0}\right)^{2n-2}. \tag{2.15}$$

This equation was obtained in the same way as Dehmelt's time averaging method [09We]. Let us consider the case where n is sufficiently large in this equation. In this case, the potential is steep near the electrodes and flattens out near the center, and changes to a box shape as a whole. In order to calculate the behavior near the electrode, the following variable transformation is applied as

$$r \to y: y = r_0 - r. \tag{2.16}$$

Here, we introduce pitch 'a', the distance between neighboring electrodes, as shown in Figure 2.9,
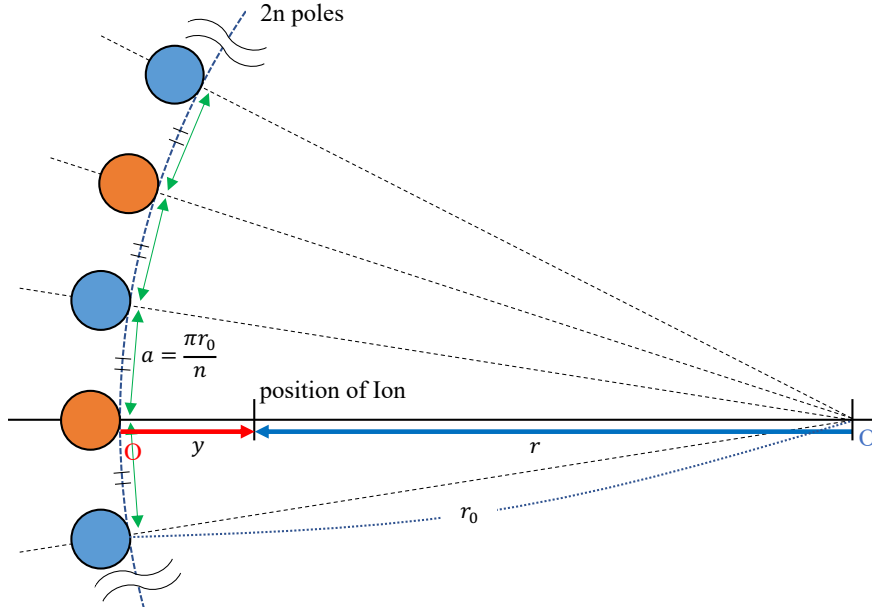
$$a = \frac{\pi r_0}{n}. \tag{2.17}$$

Figure 2.9. Cross sectional view of a multipole RF trap.
A coordinate transformation from r to y is shown.

When n is sufficiently large, the electrode configuration can be regarded as almost flat at the vicinity of the electrodes (see Fig. 2.10 (a)), and $U_{\text{eff}}(y)$ is ecpressed as,

$$U_{\text{eff}}(y) = \frac{\pi^2 q^2 V_0{}^2}{4m(\omega^2 + D^2)a^2} \lim_{n \to \infty} \left(1 - \frac{\pi y}{na}\right)^{2n-2}$$

$$= \frac{\pi^2 q^2 V_0{}^2}{4m(\omega^2 + D^2)a^2} \exp\left(-\frac{2\pi}{a} y\right). \tag{2.18}$$

This indicates that an exponential repulsive potential is generated around the electrode. Furthermore, by applying a constant voltage lower than the surroundings to the electrodes, an electrostatic field (pushing electric field) E_0 is superimposed in the direction of the electrodes (-y direction) and the potential becomes

$$U_{\text{eff}}(y) = \frac{\pi^2 q^2 V_0{}^2}{4m(\omega^2 + D^2)a^2} \exp(-\frac{2\pi}{a} y) + qE_0 y. \tag{2.19}$$

For example, when the parameters above mentioned are set at the values as shown in Fig. 2.10, the potential becomes as shown in Figure 2.10 (b) and a minimum point is created. This allows the ions to be trapped without hitting the electrodes, and this ion trapping device is called an RF carpet.
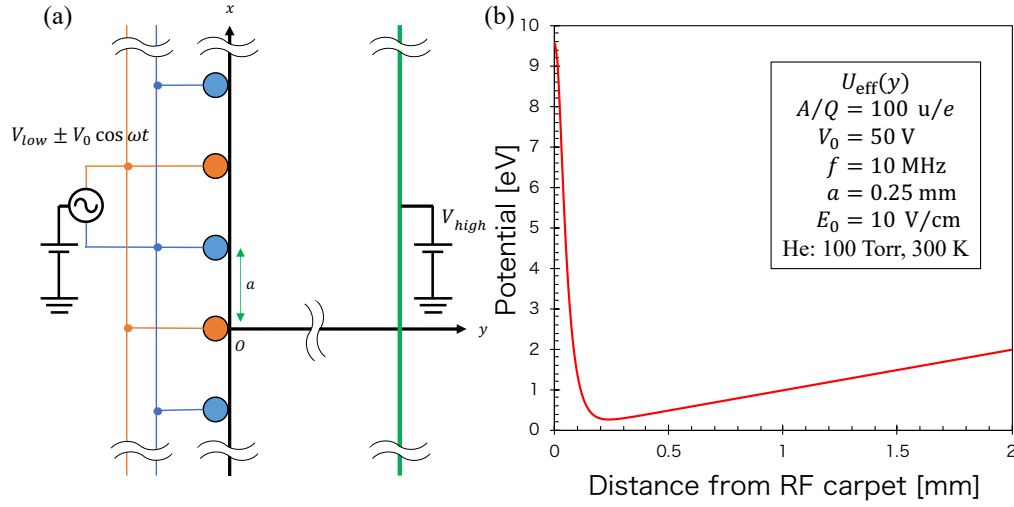
Figure 2.10. (a) Schematic of the cross-sectional view of a radiofrequency (RF) carpet and (b) typical potential energy U_{eff}. In addition to the RF voltages V_0 to create a repelling force, a static voltage V_{low} and V_{high} are applied to create an attracting force with strength E_0 which pushes the ions towards the carpet.

Since the RF carpet actually consists of a series of striped electrodes on a two-dimensional surface, the exact potential as a function of distance from the carpet cannot be obtained analytically, but a better analytical expression of the electric field by boundary condition approximation has recently been derived [11Sc]. This approximation, although more complicated, is equivalent to [Eq. (2.19)], except for the very vicinity of the electrode ($y \ll a$).

There are two methods for transporting ions trapped on the RF carpet surface in arbitrary directions: the electrostatic field gradient (DC mode) or the audio-frequency (AF) traveling wave (AF mode) is superimposed on the RF signal, and the combined signal is applied on the RF carpet (RFC).

3 Development for RFGC

We have developed a Radio-Frequency carpet-type ion guide Gas Cell (RFGC) at a SLOW RI beam facility (SLOWRI) in RIKEN RIBF. This RFGC is the first equipment to extract the unstable nuclei provided in BigRIPS as high-quality slow RI beams.

3.1 Design of RFGC

Neutron-rich nuclei of our interest provided with BigRIPS have low intensities and short lifetimes. Therefore, the key is to extract rare RIs from the gas cell efficiently and quickly. After the energy degradation, the energy spread of RI becomes larger, compared with the energy acceptance of the gas cell in the case of a fast RI beam provided with BigRIPS. In this case, if the conventional RFGC [05Ta], in which a RF carpet was located at the downstream of the gas cell and on the beam axis, is adopted, (1) the average extraction time can become large, (2) the RF carpet can be charged up by the direct hitting with the fast RI beam, causing a malfunction, and (3) the distortion on the electric field in the gas cell will be enhanced by the space charge effect of the large number of He ions caused by the beam energy loss due to the long survival time of He ions in the gas cell. In order to solve these problems, a gutter structure (Fig. 3.1) along the beam axis was selected for efficient and quick collection of stopped RIs inside the gas cell. The gutter structure consists of three parts: DC electrode arrays, a couple of 1st RF carpet, and a 2nd RF carpet. Ions stopped in the buffer gas are firstly attracted to the 1st RF carpet by the electric field formed by the DC electrodes arrays (red equipotential lines in Fig. 3.2 (a)), then transported to the 2nd RF carpet by the RF and the electrostatic field applied to the 1st RF carpet (DC mode). And then they are transported to the exit hall on the 2nd RF carpet by the RF and traveling electric wave applied to the 2nd RF carpet (AF mode). The ions coming out of the exit hole are transported to the downstream (MRTOF side) by the QPIG. This structure is called as a gutter structure because it is similar to the way that rain (ion) falling on a roof (1st RF carpet) is transported into a rain gutter (2nd RF carpet). This structure allows; (1) faster extraction time because the exit hole is located at the center of the gas cell, (2) to avoid direct beam impact on the carpet, and (3) to suppress the electrostatic field distortion because the distance to transport for numerous He ions can be shortened.
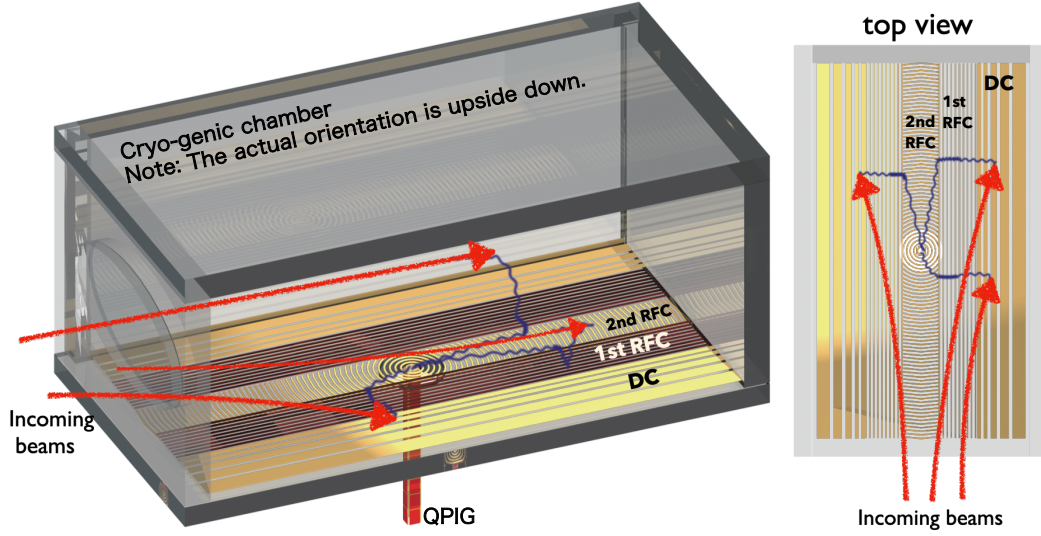
Figure 3.1. Bird eye view (left) and top view (right) of the schematic electrodes structure of RFGC. The incoming ions are stopped and thermalized in the buffer gas and are collected on the 1$^{\text{st}}$ RF carpet (RFC) by the electrostatic field generated by the DC electrodes array (DC). As the ions approach the 1$^{\text{st}}$ RFC surface, they are guided by the RF ion guide method (DC mode) to the gap between the two 1$^{\text{st}}$ RFCs. And then they are ejected through the gap and are attracted to the 2$^{\text{nd}}$ RFC by the electrostatic fields formed by the 1$^{\text{st}}$ and 2$^{\text{nd}}$ RFCs. Using the ion surfing method (AC mode), ions are transported to the exit hole by a travelling wave with superimposed RF and AF. On arrival at the exit hole, the ions are again attracted to the QPIG and are taken out of the gas cell.

Furthermore, this method has the advantage that the He ions produced by the energy loss of the beam can be killed on the 1$^{\text{st}}$ RFC due to the lighter atomic mass of the He ions. This can be understood by approximating [Eq. (2.18)] under high gas pressure conditions ($D \gg \omega$), where the repulsive effective electric field from the RF carpet is

$$E_{\text{eff}}(y) = -\frac{1}{q}\nabla U_{\text{eff}}(y)$$

$$= \mu \cdot \frac{m}{q} \cdot \frac{\pi^3 V_0^2}{2a^3}\exp\left(-\frac{2\pi}{a}y\right), \tag{3.1}$$

and the lighter the mass of the ion, the more difficult to trap them.

The ion surfing method used in the 2nd RFC (AF mode) has a higher transport speed than the conventional RF ion guide method (DC mode), but it is more sensitive to space charge. For this reason, the two methods are used selectively.

3.1.1　DC electrode array

A large area RF carpet is required in order to collect the ions stopped in a gas cell with the large volume. However, if the carpet becomes larger, the capacitance also becomes larger. As the result, a sufficient RF voltage and RF resonance frequency cannot be achieved. Therefore, DC electrodes array were introduced to focus the ions on a relatively small area of RF carpet.

Figure 3.2 (a) shows the equipotential surface inside RFGC to guide the ions toward the RF carpet section. We selected the potential shape which is proportional to the reciprocal of the distance x ($\propto 1/x$).

In order to reproduce such electric field, the DC electrode array was designed with changing the width of each electrode as shown in Fig. 3.2 (c). The blue line in Fig. 3.2 (c) shows the potential generated with a constant voltage step between adjacent electrodes. The red line shows the $\propto 1/x$ potential on the DC section and the $\propto x$ potential on the 1st RF carpet section. The SIMION [00Da] simulations confirm that among the three potentials ($\propto 1/x$, $\propto x$, and $\propto \log(x)$), the $\propto 1/x$ potential on DC electrodes array produces the best focusing on the 1st RFC area.
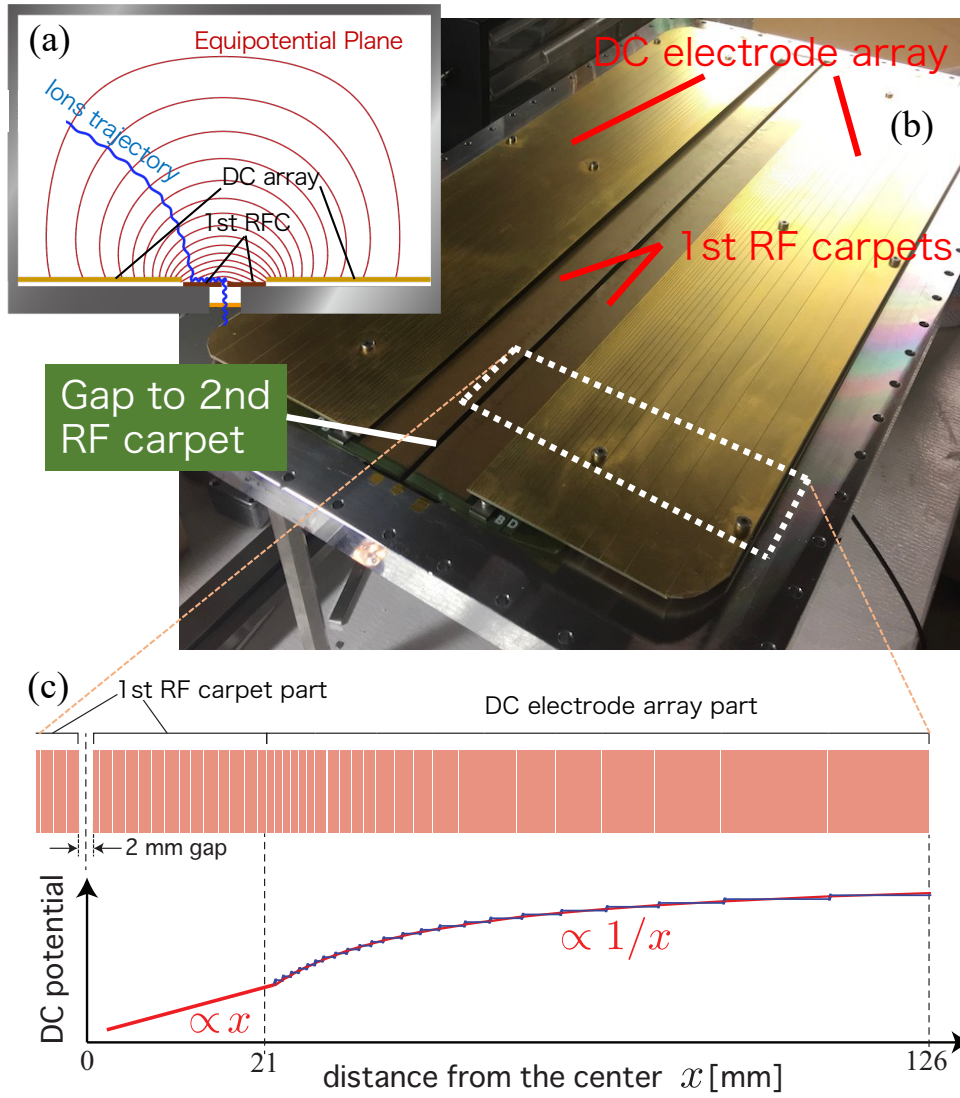
Figure 3.2. (a) Equipotential surface perpendicular to the beam axis, calculated by SIMION [00Da]. (b) Photo is the designed DC electrode array and the 1st RFC. (c) Geometry and DC potential configuration of the 1st RFC and the DC electrode array are shown with their potentials.
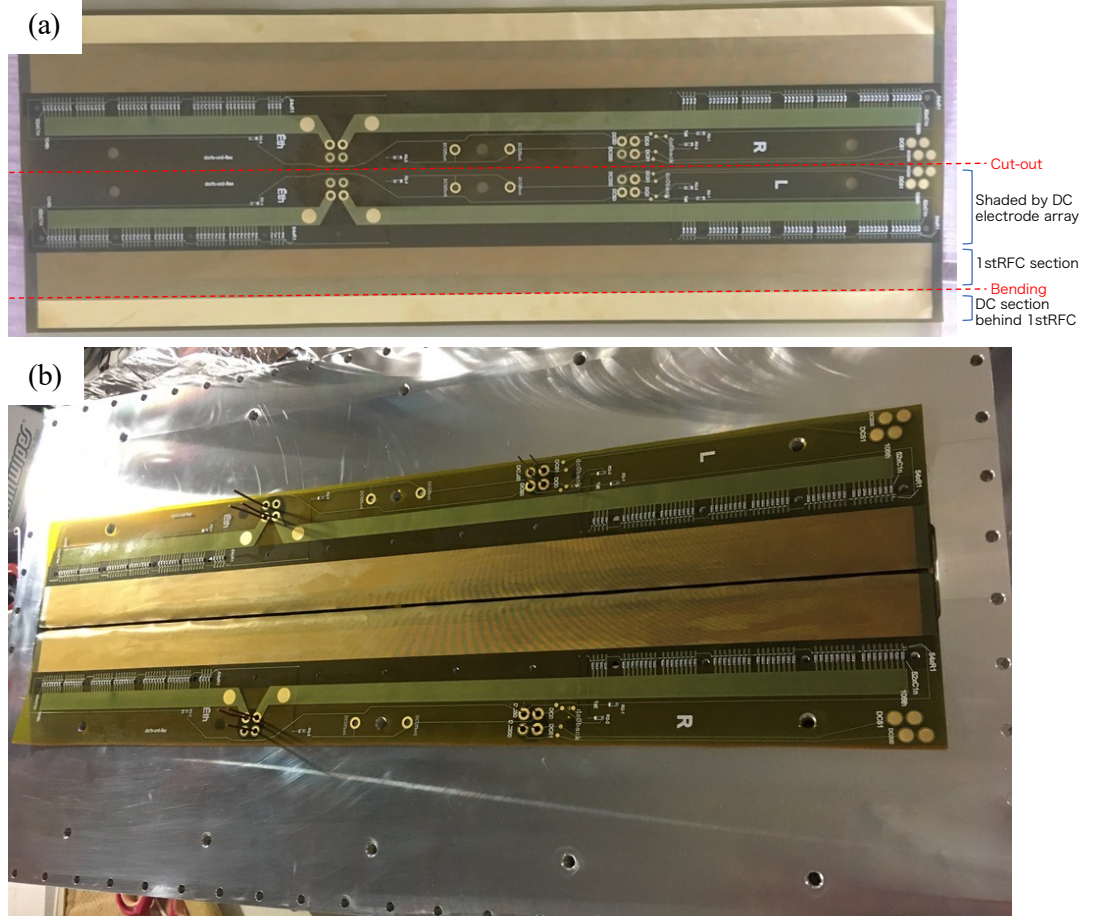
3.1.2 1st RF carpet

Figure 3.3. Photo of the 1st RFC (a) before and (b) after assembly.

The 1st RFC consists of a carpet section, a DC section, and a resistor divider circuit section as shown in the Fig. 3.3(a). For the installation, the 1st RFC is cut at the cut-out line in the Fig.3.3(a) and split into two parts, one on the left side along the beam axis and the other on the right side. The 1st RFC folded at the bending line is installed on the lid of RFGC. The 1st RF carpet section is 485 mm long and 25 mm wide with striped electrodes of 0.32 mm pitch and 0.16 mm spacing. The DC section is a single 15 mm × 485 mm electrode located behind the 1stRCF (facing the 2ndRFC at 5mm spacing). The DC electrode plays a crucial role for creating pushing electric fields to the 2ndRFC.

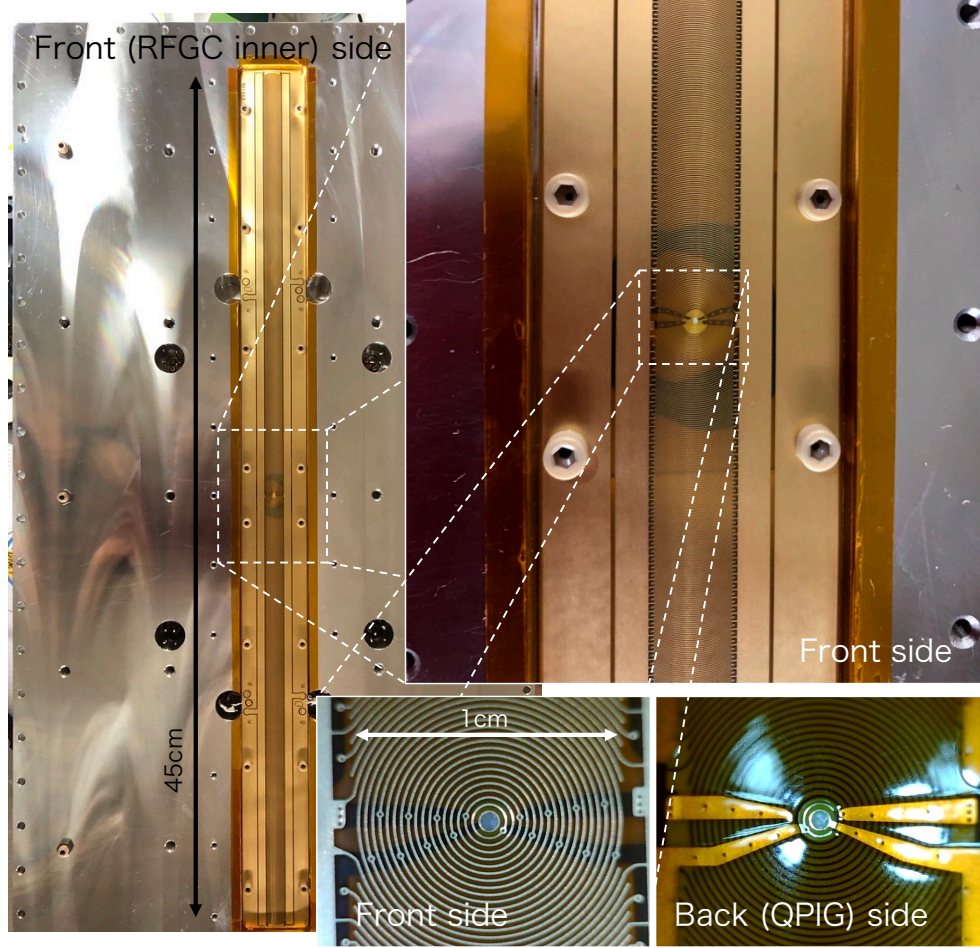### 3.1.3   2nd RF carpet

Figure 3.4. Photo of 2nd RFC after assembly.

The second-stage RFC consists of concentric ring electrodes with a pitch of 0.25 mm and a width of 0.1 mm. The RF section of the 2nd RFC are 485 mm long and 10 mm wide as shown in Fig. 3.4. An exit hole of 0.65 mm diameter is located at the center of the 2nd RFC. Ions are collected on the 1st RFCs and transported to the inner edge of the pair of the 1st RFCs. After being attracted to the 2nd RFCs with a DC electric field, the ions are transported to the exit hole with a transport method called as "ion surfing", which combines a two-phase radio-frequency electric field with a four-phase audio-frequency (AF) electric field. Behind the exit hole, a segmented quadrupole ion beam guide (QPIG) is installed. The ions are transported with this QPIG into the high vacuum region via a differential pumping stage.

3.1.4   QPIG

The QPIG consists of a 135 mm long quadrupole flat electrode with 2 mm width and 3 mm spacing ($= 2r_0$), which is divided into 35 segments to generate an electrostatic field gradient for the ion transportation to the downstream. Figure 3.5 shows a schematic view and photos of QPIG. The ions arriving at the exit hole of the 2nd RFC are attracted to the QPIG with the DC electric field and the gas flow, then trapped in the radial direction with the RF quadrupole electric field and manipulated to the axial direction with the DC electric field gradient. In this experiment, the end of the QPIG is connected to the front side of liner Paul trap (fRT), which is the injection port of the MRTOF system.
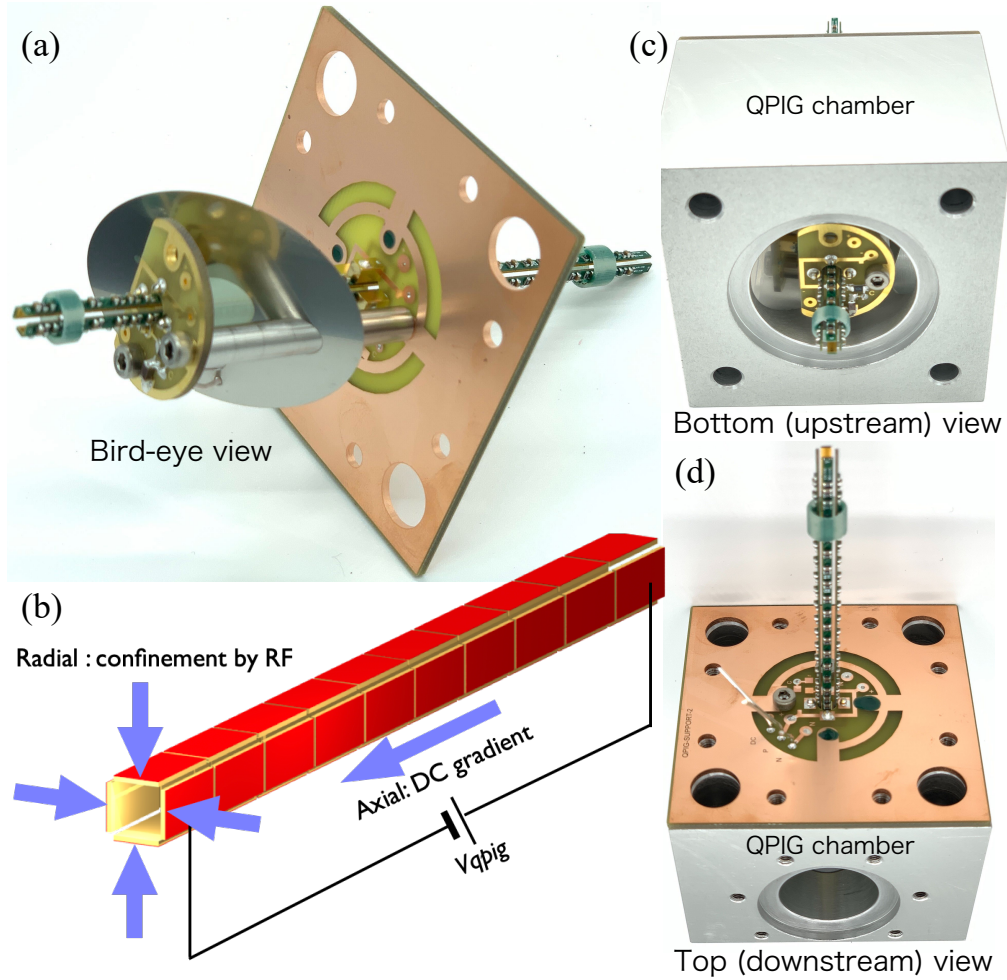

Figure 3.5. Photo of QPIG (a,c,d) and schematic of electrode structure (b).

Figure 3.6 shows the picture of the RFGC, where the RFCs are mounted on the ceiling inside the RFGC (See the inset of Fig. 3.6). A chamber in which the QPIG is installed is located on the top of the RFGC. The QPIG chamber has the first and second stage of the differential pumping rooms and the outer chamber of RFGC becomes the third stage.
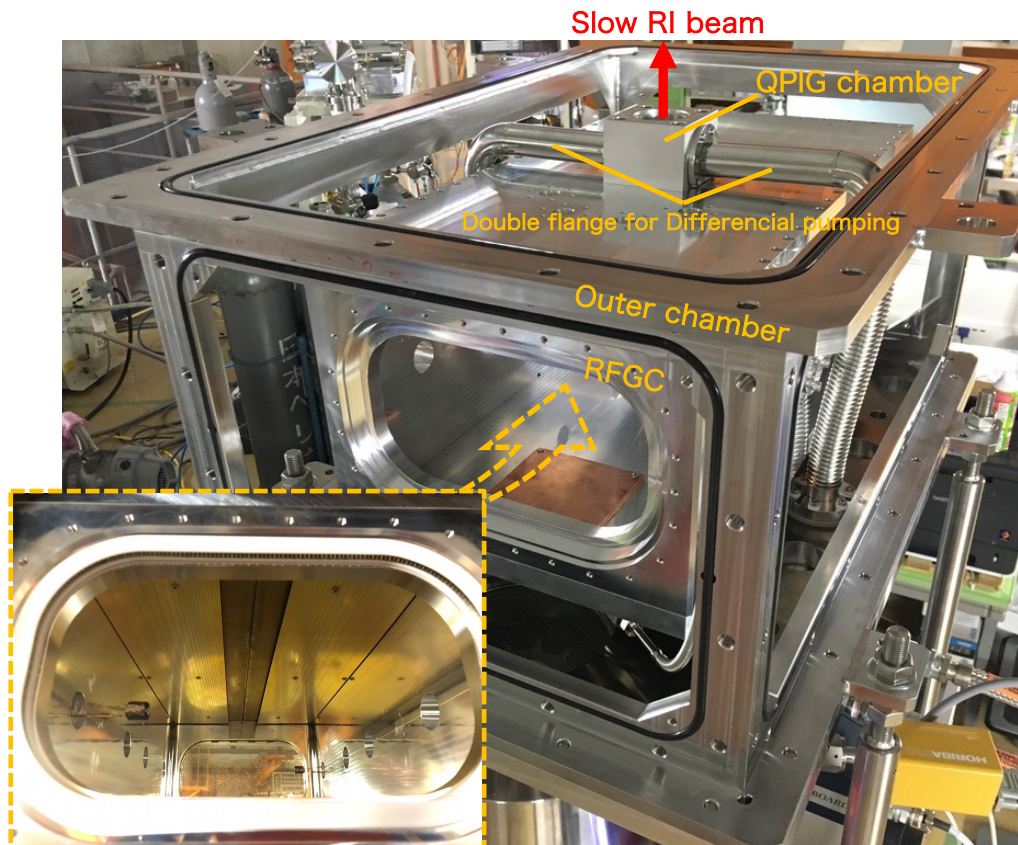

Figure 3.6. Photo of whole structure of RFGC. The RFGC is enveloped in the outer chamber for thermal insulation and the QPIG chamber is installed on top of the RFGC.

3.2   Off-line experiment

  The transport performance of the RFCs was tested using surface ionization Cs and K ion sources installed on the inner wall of the gas cell (See Fig. 3.7). The transport efficiency was evaluated with measuring the ion current with each electrode as a Faraday cup.
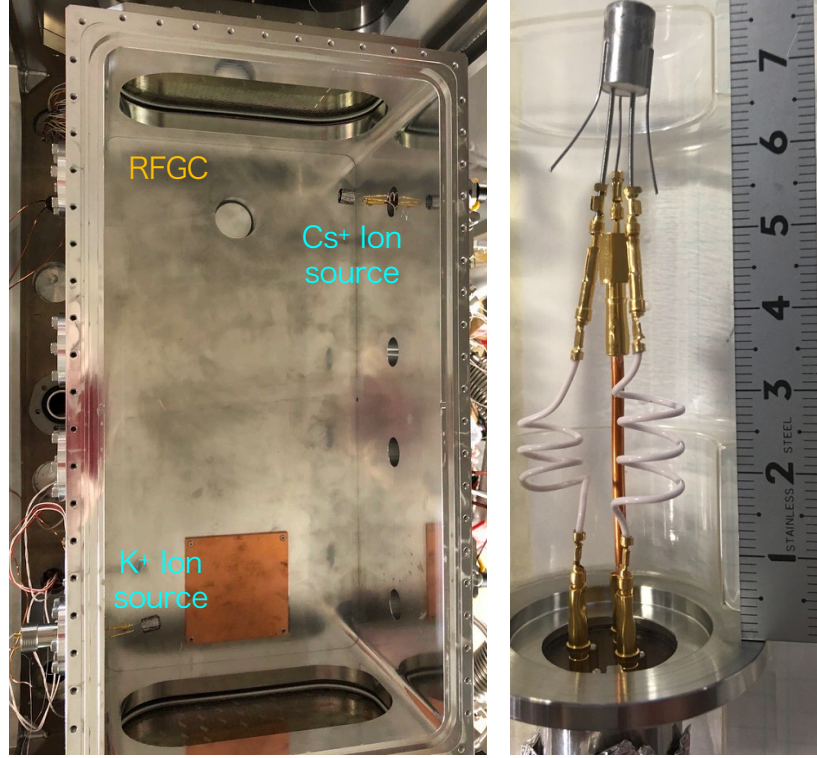

Figure 3.7. Photo of the ion sources before (right) and after (left) installation.

3.2.1   Experimental setup

  The role of the 1st RFC is to carry ions to the 2nd RFC and the ions are guided to the exit hole with a use of the 2nd RFC. at first the 1st RFC was used as a Faraday cup to measure the ion current collected in the 1st RFC using a picoampere meter (See Fig. 3.8), and then transported ions through the 1st RFC where RF and DC fields were applied. In later case, the 2nd RFC was used as a Faraday cup to measure the ion current through 1st RFC. The transport efficiency for the 1st RFC defines as the ratio between the current measured in the 2nd RFC and the one measured in the 1st RFC. Typical voltages applied on each electrodes
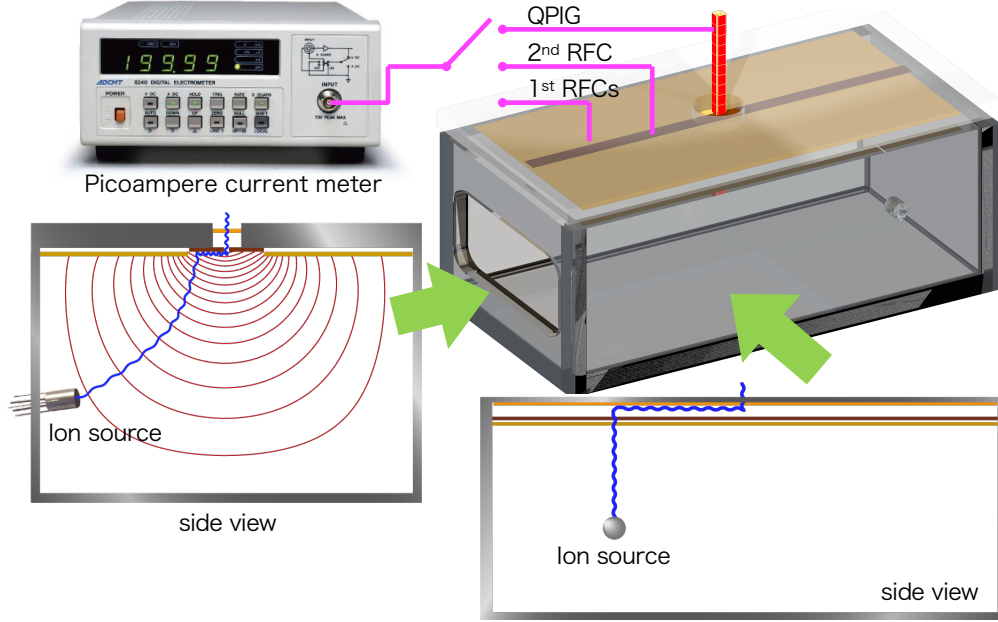
are shown in Table 3.1.

Figure 3.8. Sketch of the experimental setup at off-line experiment with an ion trajectory (blue line) and equipotential surfaces (red lines).

Table 3.1. One of the optimized electric fields parameters in offline experiment.

name	DC voltage	description	RF voltage
$V_{\text{IonSource}}$	+200 V	K^+ Ion source heater: 2.8A (1.7 Ω)	
V_{GasCell}	+175 V	RFGC chamber	
$V_{\text{DCarray}}^{\text{outer}}$	+140 V	Outermost electrode on DC electrode array	
$V_{\text{DCarray}}^{\text{inner}}$	+70 V	Innermost electrode on DC electrode array	
$V_{\text{1stRFC}}^{\text{outer}}$	+50 V	Outermost electrode on 1$^{\text{st}}$ RFC	
$V_{\text{1stRFC}}^{\text{inner}}$	+40 V	Innermost electrode on 1$^{\text{st}}$ RFC	130 V_{PP}(8.1 MHz)
$V_{\text{1stRFC}}^{\text{back}}$	+39 V	Behind of 1$^{\text{st}}$ RFC, face to face with 2$^{\text{nd}}$ RFC	
V_{2ndRFC}	+17 V	2$^{\text{nd}}$ RFC, AF signal: 10 V_{PP}(75 kHz)	90 V_{PP}(9.9 MHz)
$V_{\text{QPIG}}^{\text{up}}$	+17 V	Upstream edge on QPIG electrodes	
$V_{\text{QPIG}}^{\text{down}}$	+10 V	Downstream edge on QPIG electrodes	300 V_{PP}(6.7 MHz)
$V_{\text{FaradayCup}}$	±0 V	Faraday cup connected to picoammeter	

3.2.2 Results

Figure 3.9 shows the result of the obtained transport efficiency for the 1st RFC as a function of the RF voltages applied to the 1st RFC in three different helium gas pressures. The transport efficiency reached ~80% or more at each pressure.
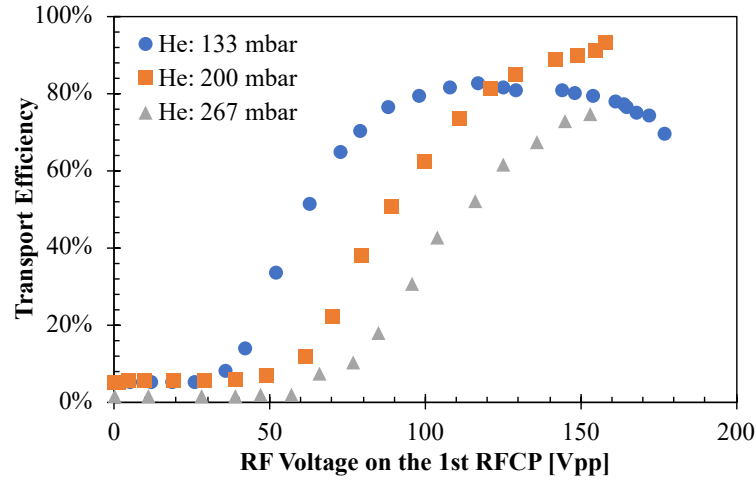

Figure 3.9. Transportation test results for the 1st carpet in three different helium gas pressures; 133, 200, and 267 mbar. In this test, the drag DC field on the 1st RFC, the extraction DC field between the 1st and the 2nd RFCs were 4 and 20 V/cm, respectively, with each RF frequency of ~5 MHz.

In an online experiment, the total extraction efficiency was determined by the product of stopping, ion survival, and transport efficiencies. In order to stop RI beam more efficiently, heavier species of buffer gas have been investigated. Figure 3.10 shows the result of the measured transport efficiency for three kinds of buffer gases. The gas pressures of neon (55 mbar) and argon (31 mbar) were adjusted so that the beam would be stopped with the same efficiency as that achieved for 133 mbar of helium. It was found that helium (133 mbar) and neon (55 mbar) gases gave comparable transport efficiencies at a certain RF voltage. On the other hand, with a higher pressure for neon, i.e., equal to the gas pressure of helium, the transport efficiency in neon gas was observed to be four times lower. In addition to these results, considering that the ion survival probability in helium is 1.3 times higher than that in neon, as shown previously [06De], the total efficiency in helium gas can become the highest value.
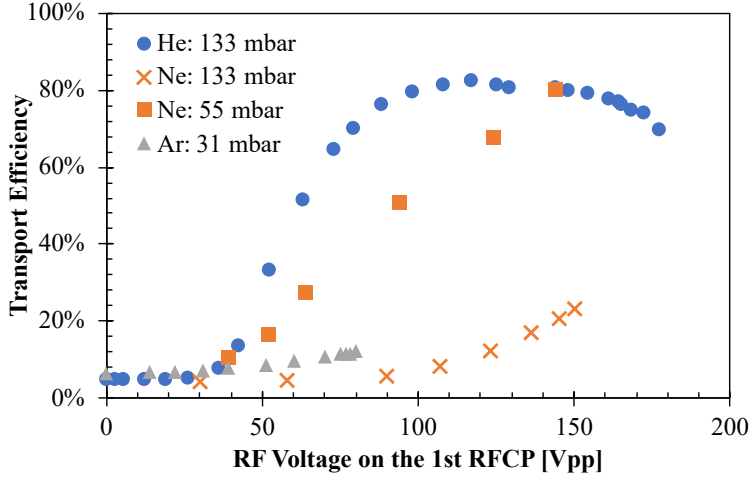
Figure 3.10. Transportation test results for the 1st RCF with Cs ions in three kinds of gas species: Ar, Ne (high and low pressures), and He. In this test, the drag DC field on the 1st RFC, the extraction DC field between the 1st and the 2nd RFCs were 4 and 20 V/cm, respectively, with each RF frequency of ∼5 MHz.

Figures 3.11 and 3.12 show the results of the test with Cs^+ ions and K^+ ions at different RF frequencies in He gas at 133 mbar. A higher transport efficiency was achieved comparing to conventional RFCs [19Ta]. The plots shows that a higher RF voltage is required to transport lighter ion at the similar frequency, which can be interpreted straightforwardly from the repulsive force of RF expressed in [Eq. (2.19)]. At voltages higher than that at the peak efficiency, an unstable behavior caused with a discharge during the ion current measurement was observed, which seemed to disturb the ion transport.
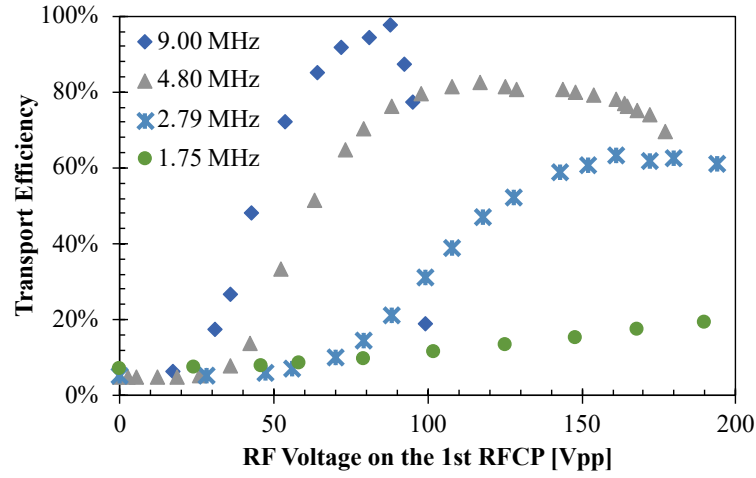
Figure 3.11. Transportation test results for the 1st RFC with Cs ions at four different RF frequencies; 1.75, 2.79, 4.8, and 9 MHz. In this test, the drag DC field on the 1st RFC, the extraction DC field between the 1st and 2nd RFCs were 4 and 20 V/cm, respectively, with He gas pressure of 133 mbar.
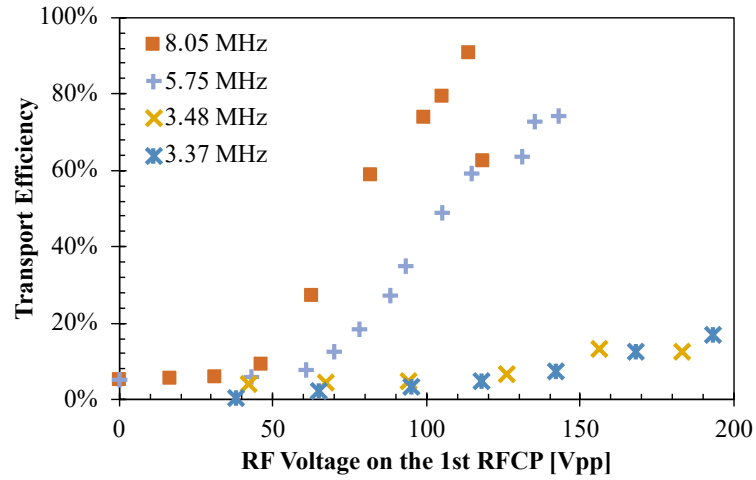

Figure 3.12. Transportation test results for the 1st carpet by K^+ ions in four different RF frequencies; 3.37, 3.48, 5.75, and 8.05 MHz. In this test, the drag DC field on the 1st RFC, the extraction DC field between the 1st and 2nd RFCs were 4 and 20 V/cm, respectively, with He gas pressure of 133 mbar.

Finally, the results of the transport efficiency for the 1st and 2nd RFCs are shown in Fig. 3.13, where the test results in He gas at 133 mbar are shown as a function of the AF voltage

at va ... as ratio
betw ... cup and
the c ... ere 103
Vpp ... een the
1st a ... r the 1st
and 2nd RFCs was achieved at about 90% on an AF frequency of 125 kHz. Above the AF
frequency of 125 kHz, there was a sharp decrease in the AF signal from 12 to 15 Vpp, which
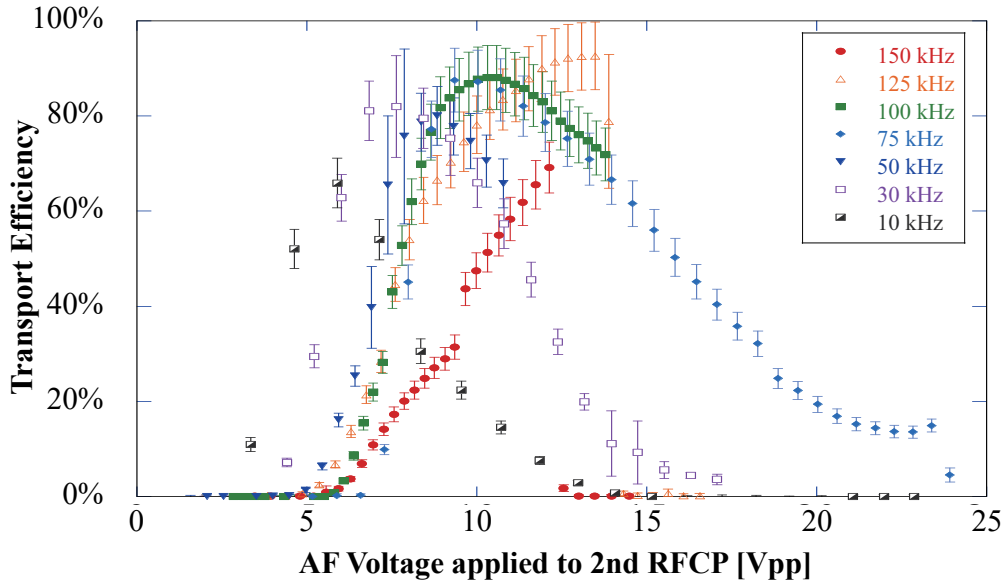was attributed to the large disturbance of the AF signal by the AF/RF coupling circuit.

Figure 3.13. Transportation test results for the 1st and 2nd RFCs with Cs^+ ions
as a function of AF voltages at various AF frequencies. In this test, the RF
voltages applied to the 1st and 2nd RFCs were 103 Vpp at 8.15 MHz and 111
Vpp at 10.06 MHz, respectively. The push DC field between the 1st and 2nd
RFCs was ~40 V/cm. He gas pressure was 133 mbar at room temperature.

4 On-line experiment

In autumn 2020, the RFGC was coupled to MRTOF system and installed in the BigRIPS experimental area at the final focal plane (F11) of the ZeroDegree beamline (ZDS) at the RIBF High Energy Facility, where continuous optimization and tests of the combined system were carried out. (ZD-MRTOF, see in Fig. 4.1).
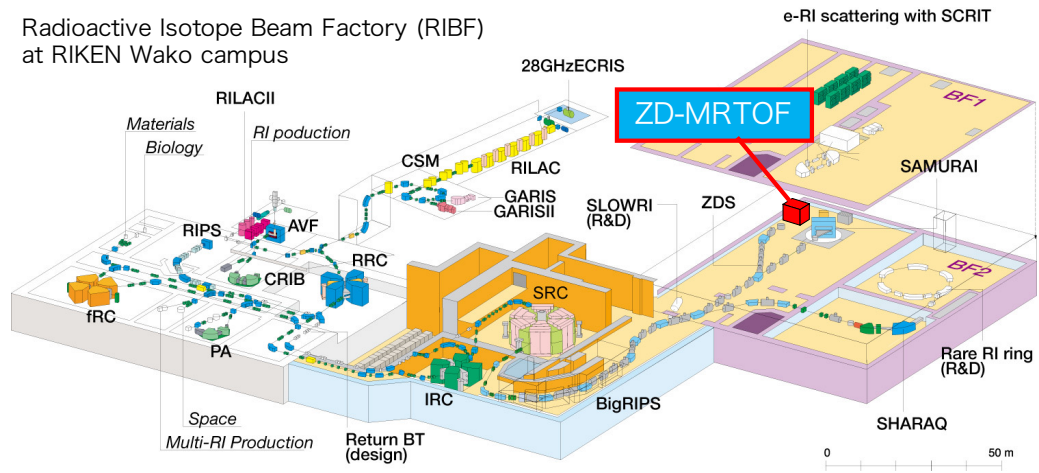

Figure 4.1. Bird eye view of RIBF.

The system was ready to operate on-line just before the start of the 2020 winter campaign of in-beam γ-ray experiments [12Do, 16Do] of HiCARI project [18Do, 21Wi], which enabled us the first on-line commissioning of the new ZD-MRTOF setup in parasitic operation. The 2020 HiCARI campaign consist of seven different experiments. This on-line commissioning of mass measurements were perform for nuclei in different areas of the nuclear chart (see Fig. 4.2).
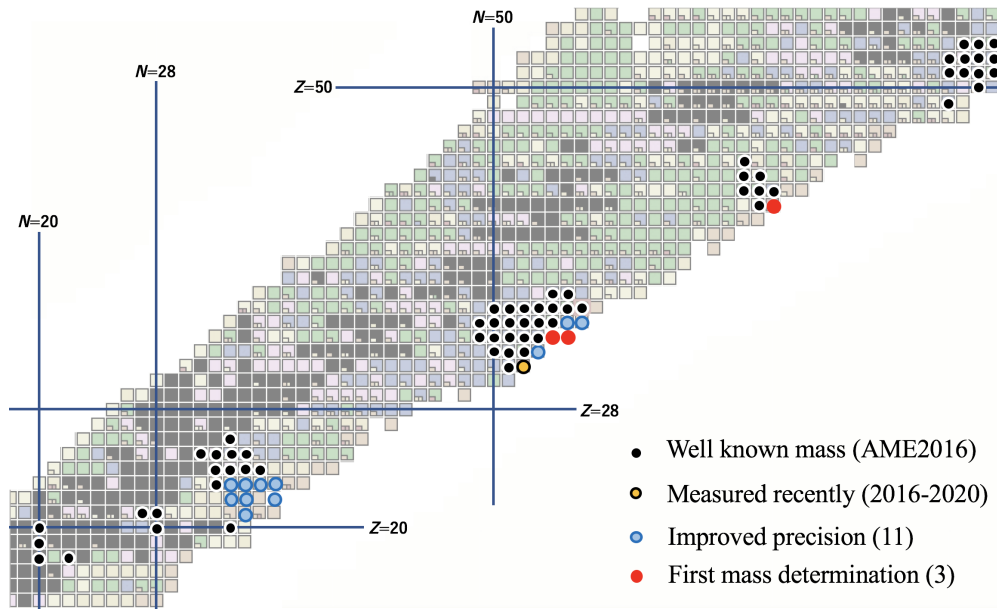
Figure 4.2. Mass measurements with the ZD-MRTOF system during on-line commissioning experiment (adapted from [21Ro]).

The radioisotopes were produced by in-flight fission of a 345 MeV/nucleon uranium beam from the RIKEN superconducting ring cyclotron (SRC) accelerator. The main production of RIs was carried out on primary beryllium targets of 5 to 11 mm thickness, depending on the isotope requested. The reaction products were separated in a BigRIPS separator and selectively delivered to a HiCARI detector array at F8 (See in Sec. 2.1). After passing through the secondary reaction target and the HiCARI detector, the reaction products were transported to the ZDS, where they were partially stopped in the RFGC. An example of a PID plots obtained with a ZDS is shown in Fig. 4.3.
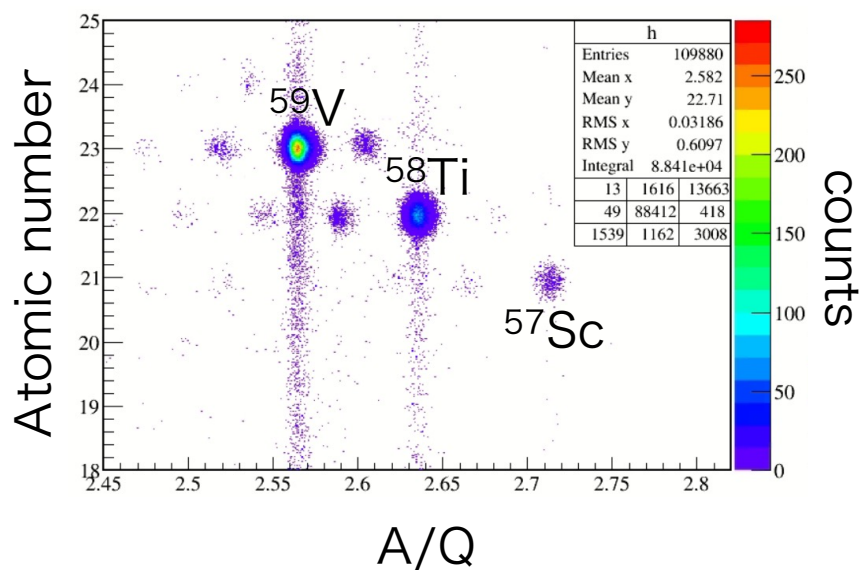
Figure 4.3. Particle identification plot of atomic number vs. mass/charge (A/Q) by using ZDS. Isotopes ^{59}V, ^{58}Ti, and ^{57}Sc are identified.

Figure 4.4 shows our experimental setup at on-line commissioning experiment. The reaction products stopped in the He gas were extracted mainly as monovalent ions and/or molecular sidebands of radioisotopes from the gas cell. The ions were transported to the MRTOF system where the masses of the isotopes were determined with high precision. The ZD-MRTOF consists of a rotatable energy degrader, RFGC, a beam monitor detector (Si detector) , a radio-frequency quadrupole (RFQ)-based low-energy beamline (QPIG, Twin linear Paul trap, and Flat ion trap), and MRTOF. The voltages applied to each electrode was optimized for each mass region, and Table 4.1 shows the voltages for the ^{58}TiOH$^+$ data taking run.

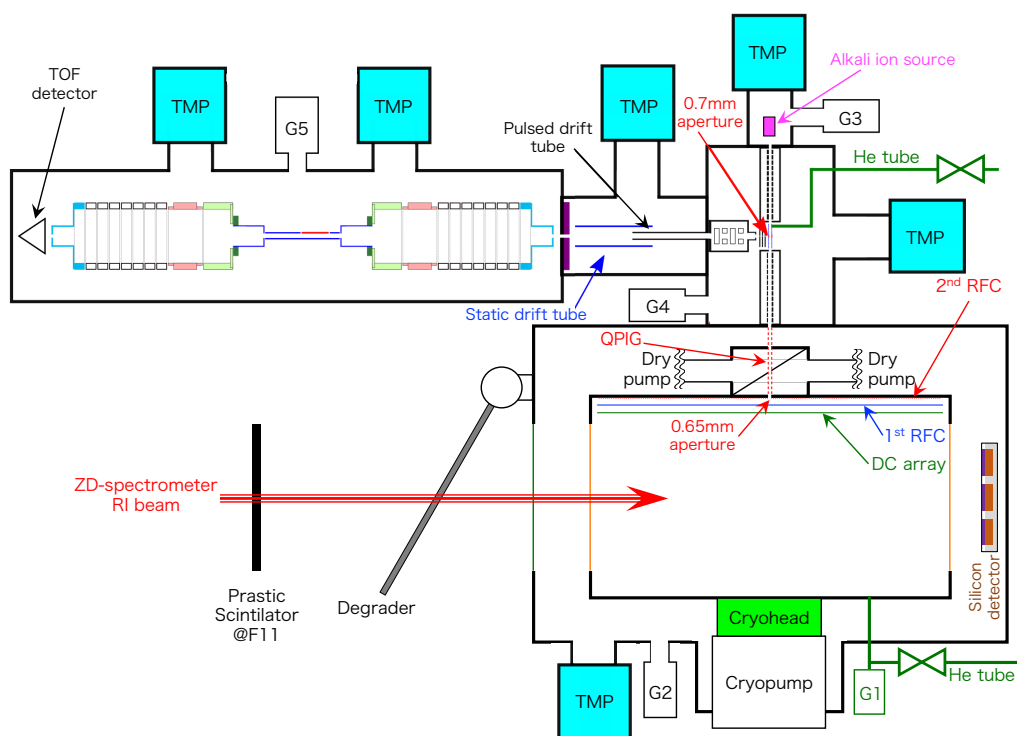**Figure 4.4.** Schematic of ZD-MRTOF system during on-line commissioning.

Table 4.1. One of the electric fields parameters during on-line experiment.

name	DC voltage	description	RF voltage
V_{GasCell}	+94 V	RFGC chamber	
$V_{\text{DCarray}}^{\text{outer}}$	+94 V	Outermost electrode on DC electrode array	
$V_{\text{DCarray}}^{\text{inner}}$	+69 V	Innermost electrode on DC electrode array	
$V_{\text{1stRFC}}^{\text{outer}}$	+59 V	Outermost electrode on 1$^{\text{st}}$ RFC	130 V$_{\text{PP}}$(8.1 MHz)
$V_{\text{1stRFC}}^{\text{inner}}$	+45 V	Innermost electrode on 1$^{\text{st}}$ RFC	
$V_{\text{1stRFC}}^{\text{back}}$	+15 V	Behind of 1$^{\text{st}}$ RFC, face to face with 2$^{\text{nd}}$ RFC	
V_{2ndRFC}	+10 V	2$^{\text{nd}}$ RFC, AF signal: 10 V$_{\text{PP}}$(75 kHz)	90 V$_{\text{PP}}$(9.9 MHz)
$V_{\text{QPIG}}^{\text{up}}$	+9 V	Upstream edge on QPIG electrodes	300 V$_{\text{PP}}$(6.7 MHz)
$V_{\text{QPIG}}^{\text{down}}$	+0 V	Downstream edge on QPIG electrodes	
$V_{\text{fLPT}}^{\text{up}}$	−5 V accumulation, cooling +20 V ejection to FT	Upstream edge on LPT electrodes for gas cell (front) side	480 V$_{\text{PP}}$(3.2 MHz)
$V_{\text{fLPT}}^{\text{middle}}$	−10 V accumulation, cooling +10 V ejection to FT	Middle part of LPT electrodes for gas cell (front) side	
$V_{\text{fLPT}}^{\text{down}}$	0 V accumulation, cooling −2.5 V ejection to FT	Downstream edge on LPT electrodes for gas cell (front) side	
V_{FT}	~0 V	Flat ion trap for MRTOF mass measurement, see [22Ro] for details	640 V$_{\text{PP}}$(3.0 MHz)
$V_{\text{rLPT}}^{\text{down}}$	30 V accumulation, cooling −1 V ejection to FT	Downstream edge on LPT electrodes for alkali ion source (rear) side	200 V$_{\text{PP}}$(2.6 MHz)
$V_{\text{rLPT}}^{\text{middle}}$	−22 V accumulation, cooling 8 V ejection to FT	Middle part of LPT electrodes for alkali ion source (rear) side	
$V_{\text{rLPT}}^{\text{up}}$	6.7 V accumulation 20 V cooling, ejection to FT	Upstream edge on LPT electrodes for alkali ion source (rear) side	

5 Data analysis and results

5.1 Performance of RFGC

Table 5.1 shows the efficiencies for several RI species with PID: the total efficiency ($\varepsilon_{\mathrm{total}}$) of each RI was calculated as the ratio of the count rate observed after MRTOF to the count rate before RFGC by plastic scintillator. The stopping efficiency ($\varepsilon_{\mathrm{stop}}$) is the fraction of RIs stopped by the RFCG and was evaluated using LISE++ [08Ta] based on the measured energy distribution of each RI. With the application of monochromatic beam optics in the future [20Ch], $\varepsilon_{\mathrm{stop}}$ is expected to be improved by a factor of 5 or more.

Table 5.1. Total efficiencies ($\varepsilon_{\mathrm{total}}$) measured with the detectors on ZDS and the MRTOF. Stopping efficiencies ($\varepsilon_{\mathrm{stop}}$) were calculated from LISE^{++} with experimental beam-energy distribution of RI. The transport efficiencies ($\varepsilon_{\mathrm{trans}}$) correspond to ion transmission from the gas cell to MRTOF.

Nuclide (ions)	$\varepsilon_{\mathbf{total}}$	$\varepsilon_{\mathbf{stop}}$	$\varepsilon_{\mathbf{trans}}$
$^{134}\mathrm{Sb}^+$	1.1 %	9.1 %	12 %
$^{137}\mathrm{Te}^+$	1.3 %	9.2 %	14 %
$^{88}\mathrm{Se}^+$	0.33 %	3.4 %	10 %
$^{90}\mathrm{Se}^+$	0.36 %	2.0 %	18 %
$^{85}\mathrm{As}^+$	0.16 %	3.6 %	4 %
$^{55}\mathrm{ScOH}^+$	0.0007 %	2.9 %	0.02 %
$^{48}\mathrm{CaOH}^+$	0.014 %	3.2 %	0.44 %

The transport efficiency ($\varepsilon_{\mathrm{trans}}$) was obtained by dividing $\varepsilon_{\mathrm{total}}$ by $\varepsilon_{\mathrm{stop}}$. Note that $\varepsilon_{\mathrm{trans}}$ includes not only RFGC but also ion guide, ion trap and MRTOF transmission. As shown in Table 5.1, a reasonable $\varepsilon_{\mathrm{trans}}$ of more than 10% was obtained for many RIs. The $\varepsilon_{\mathrm{trans}}$ depends on several factors, including the incident beam intensity, which contributes to the space-charge effect [05Ta], the mass-to-charge ratio, which affects the stability of the RF trap [20Ta], the half-life, which leads to decay losses, and the chemical properties of the incoming species due to impurities in the He gas. These molecular formations can be suppressed by further cooling of the RFGC. Improved performance was confirmed by the

experience of the cryogenic gas cell in GARIS II [17Sc] .

Also, Fig. 5.1 shows the intensity of measured RIs at MRTOF as a function of the temperature on the RFGC. We used high purity He gas (G1 grade) and the He gas was further purified to sub-ppb levels with a heated getter gas purifier (MonoTorr, PS4-MT15). However, residual impurities, e.g., emitted from the chamber wall when RI beams are injected into the RFGC, can reduce the efficiency by molecular formation or neutralization of the target ions. Therefore, further purification was performed by a use of cooling the RFGC. In this experiment, the RFGC was cooled down to 180 K.
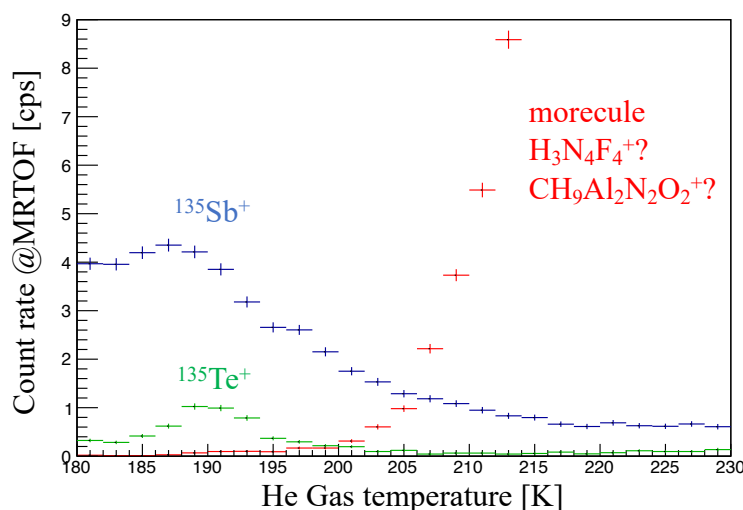
.

Figure 5.1. He gas temperature dependency of count rate of ^{135}Te$^+$, ^{135}Sb$^+$, and molecular ions at MRTOF.

As shown in Fig. 5.1, it was observed that as the temperature increased, the number of ions of interest decreased and the number of contaminant molecules increased. It is also interesting to note that the slight decrease below 190 K may suggest a branching towards 2^+ charge state from single charge of RIs of interest [17Sc].

Through this on-line commissioning we have been able to evaluate various performances and have found that there is a room for the improvement such as cooling performance on

the RFGC. We are currently developing a longer gas cell (1.5 m length) and our knowledge obtained here will be adopted for the development of the longer gas cell.

5.2 Mass of neutron-rich nuclei with $A = 50\text{-}60$

5.2.1 TOF mass measurement

The exact formula for the relation between mass and TOF, introduced in Chap. 2, is

$$m_x = q_x \frac{m_r - q_r m_e}{q_r} \left(\frac{t_x - t_0}{t_r - t_0}\right)^2 + q_x m_e. \tag{5.1}$$

The m_x and m_r are atomic mass of interest and reference, q are charge of each ion, m_e is electron mass. The binding energy of the electron is on the order of a few eV, which is negligible given the current measurement accuracy. The t_x and t_r are the TOF of the analyte and reference ions respectively, and t_0 is a constant offset due to the circuits of the data acquisition system.

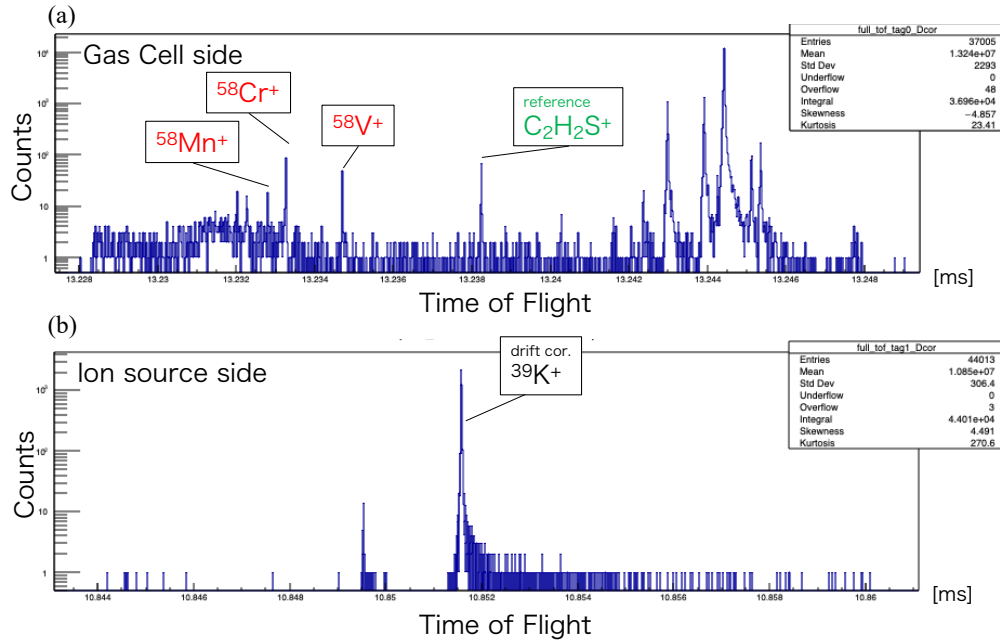Figure 5.2 shows an example of the TOF spectrums we obtained in the experiment.

Figure 5.2. An example of the TOF spectra obtained in the online experiment (a) for RIs extracted from RFGC and (b) for K+ from the off-line ion source. Those spectra were obtained by sequential measurement with 25 ms intervals.

5.2.2 TOF Drifting

In the case of long-term measurements, time fluctuation can occur on a TOF spectrum (as shown in Fig. 5.3). Typical sources of the time fluctuation are thermal expansion and contraction of the MRTOF spectrometer, drifting of voltages from the power supplies depending on temperature, and the fluctuations of voltages due to the limits in the stability of the power supplies. In order to obtain precise flight time, the time fluctuation was corrected by the following method.
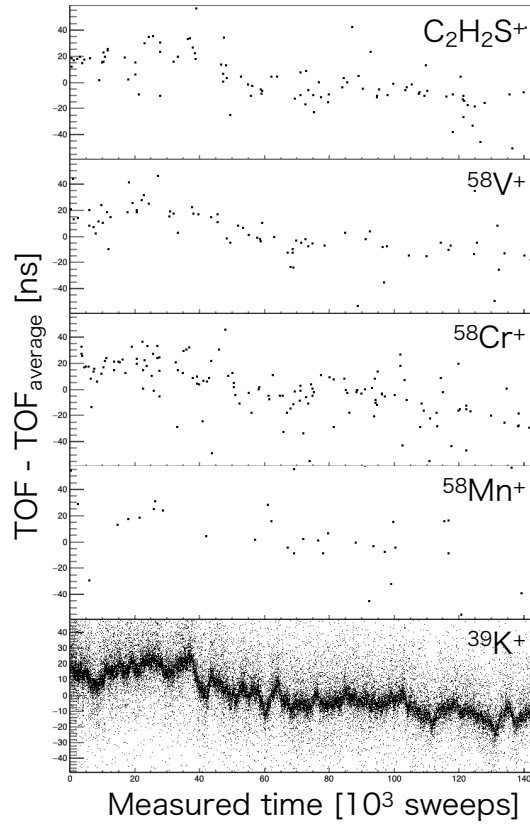

Figure 5.3. Example of TOF drift.

5.2.2.1 Drift correction method

The TOF drift was corrected by using the flight time of reference ions which were provided from the off-line alkali ion source as mentioned before. The correction was performed as the following steps.
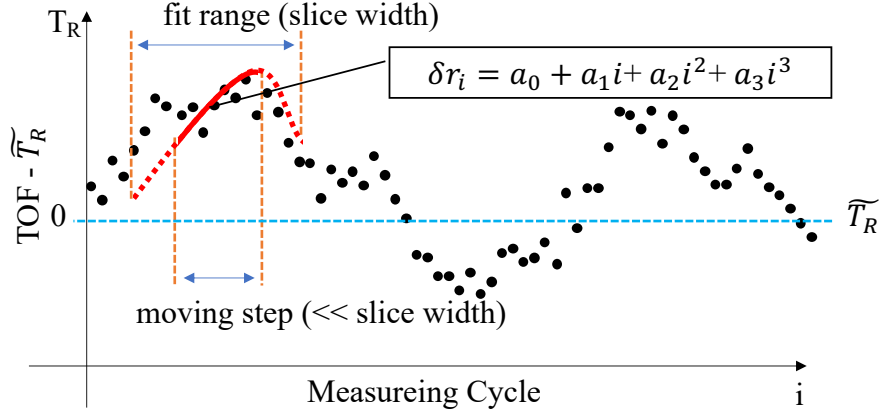
Figure 5.4. Schematic diagram of the drift correction algorithm.

Step 1. The average time of flight $\widetilde{T_R}$ from the raw data of the drift-tracking ion's peak was deduced (In Fig. 5.3 case, drift-tracking ion is $^{39}K^+$ from alkali ion source).

Step 2. Each TOF of the drift-tracking ion T_{R_i}, which was subtracted $\widetilde{T_R}$, was plotted as a function of the measuring cycle i with every 25 ms interval, as shown in Fig. 5.4. The χ-square fitting for a suitable width, indicated as 'slice width' in Fig. 5.4, was done using a polynomial function of i up to third order

$$\delta r_i = f(i) = a_{i0} + a_{i1}i + a_{i2}i^2 + a_{i3}i^3$$

Step 3. The procedure from step1 to step2 was repeated until end of the each run, shifting by the step width ("moving step" in Fig. 5.4) with keeping the slice width, similar as running (moving) average calculation. N (= [Total cycles] / [moving step]) iterations are completed.

Step 4. As the correction factor δr_i has been obtained for all cycles, the TOF drift is corrected for each i-th cycle using the following formula,

$$T_{Xcor_i} = T_{X_i} \left(1 + \frac{\delta r_i}{\widetilde{T_R}}\right)^{-1} , \quad \left(\because \ \frac{T_{Xcor_i}}{\widetilde{T_R}} \approx \frac{T_{X_i}}{\widetilde{T_R} + \delta r_i} = \frac{T_{X_i}}{T_{R_i}}\right), \tag{5.2}$$

where T_{X_i} and T_{Xcor_i} are all TOF raw and corrected data of i-th cycle, respectively.

An example of the result of the correction is shown in Fig. 5.5. The figure shows TOF

spectra for ^{39}K$^+$ ions provided from the alkali ion source (Show in Fig. 4.4), during one-hour measurement. Fig. 5.5 (a) and (b) shows the TOF spectrum without the drift correction and with the drift correction, respectively, using the slice width of 500 cycle and the moving step of 10. The full width of half maximum (FWHM) was improved from 30 ns to 7 ns after the drift correction, leading to the improvement of mass resolving power $R_m(= \frac{TOF}{2\Delta TOF_{\text{FWHM}}})$ with a factor of 4.
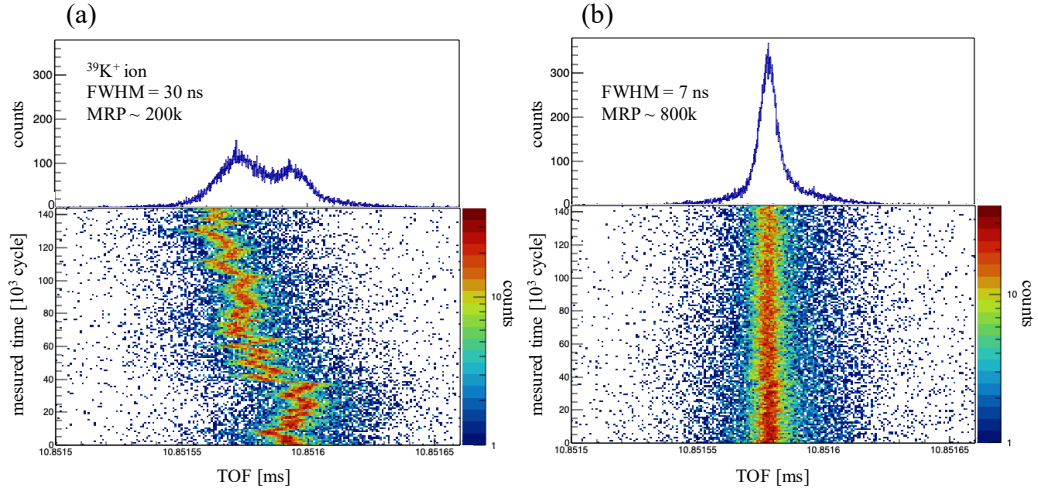

Figure 5.5. An example for the drift correction for the TOF spectrum of K$^+$ ions from the off-line ion source (a) without the correction and (b) after the drift correction.

Using the same correction factor of $\delta r_i / \widetilde{T_R}$ obtained by the method mentioned above, the correction of [Eq. (5.2)] was adopted for all flight time of ions extracted from RFGC during the same run. Figure 5.6 shows an example for TOF spectra for RIs extracted from RFGC without the drift correction (a) and with the correction (b), respectively. The time resolutions are clearly improved after the drift correction.
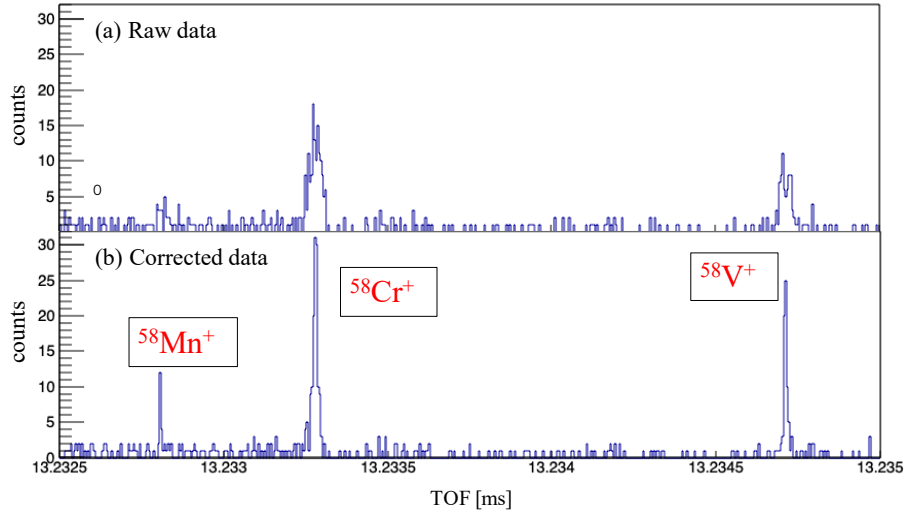
Figure 5.6. TOF spectrum (a) before and (b) after drift correction.

5.2.2.2   Systematic study for drift correction method

In general, this correction method depends on the slice width. Fig 5.7 shows obtained mass resolving power using reference ions of $^{39}K^+$ as a function of the slice width.

As shown in Fig. 5.7, the MRP obtained using the polynomial functions is better, compared with the one by our previous method. Also, in the previous method, a fine tuning for the slice width is required. By using more than second-order polynomial functions, good corrections can be provided in a wide range from 400 to 1000 slice width. We have selected to use 3rd order polynomial function and 500-600 slice width for the analysis of all TOF data.
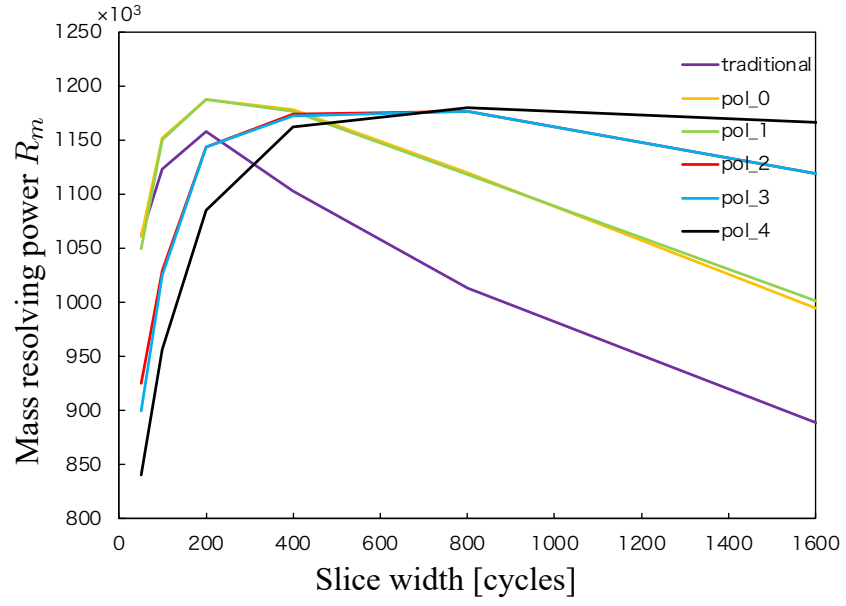
Figure 5.7. Mass resolving power R_m obtained using reference $^{39}K^+$ ions from alkali ion source, as a function of the slice width. The colored lines show the MRP by the previous method using just an averaged value for a certain slice width and the ones using polynomial functions from 0th to 4th order with the fixed moving step of 10 cycles.

5.2.3 TOF peak fitting

After the drift correction, TOF spectra for ions extracted from RFGC are shown in Fig. 5.6. In general, the shape of the peak measured with MRTOF is deviated from the gaussian distribution. This distortion can be considered to be the reflection of the initial energy distribution, the evolution in phase space of the position and energy due to multi-reflections in the mirror potential and so on. Thus, Johnson's S_U distribution [49Jo], which has skewness and kurtosis as parameters in addition to the location and width parameters, is empirically selected as a fitting function of the peak. This distribution is often used to fit a mass difference for charm meson decays [21Aa]. The function formula is

$$f_{\text{peak}}(x) = \left(1 + \left(\frac{x-\mu}{\lambda}\right)^2\right)^{-\frac{1}{2}} \exp\left[-\frac{1}{2}\left\{\gamma + \delta\sinh^{-1}\left(\frac{x-\mu}{\lambda}\right)\right\}^2\right]. \qquad (5.3)$$

x is a variable, and $\mu, \lambda, \gamma,$ and δ are the parameters for location, width, skewness, and kurtosis, respectively. In addition to this function, we select the equation for the background as a linear function,

$$f_{\text{BG}}(x) = a_0 + a_1 x. \qquad (5.4)$$

The actual fitting function is normalized within the fitting range as a probability density function and is expressed as follows.

$$k_{\text{SNR}} \times \text{PDF}\left[f_{\text{peak}}(x)\right] + (1 - k_{\text{SNR}}) \times \text{PDF}\left[f_{\text{BG}}(x)\right], \qquad (5.5)$$

whrere $\text{PDF}[f(x)]$ means that the function $f(x)$ is normalized within a fitting range, and k_{SNR} is a coefficient between 0 and 1, which indicates the signal-to-noise ratio.

We used the unbinned maximum log-likelihood method for the peak fitting. The algorithm was written using the RooFit package [03Ve] of the ROOT library [97Br], and global fitting was performed simultaneously for several analyte peaks and one mass reference peak (usually isobaric molecular ion), in which all the parameters were floated and the shape parameters of γ and δ were given as common parameters. When isobaric ion's peaks are fitted, the width parameter (λ) was also taken as a common parameter. An example of peak fitting is shown in Fig. 5.8.
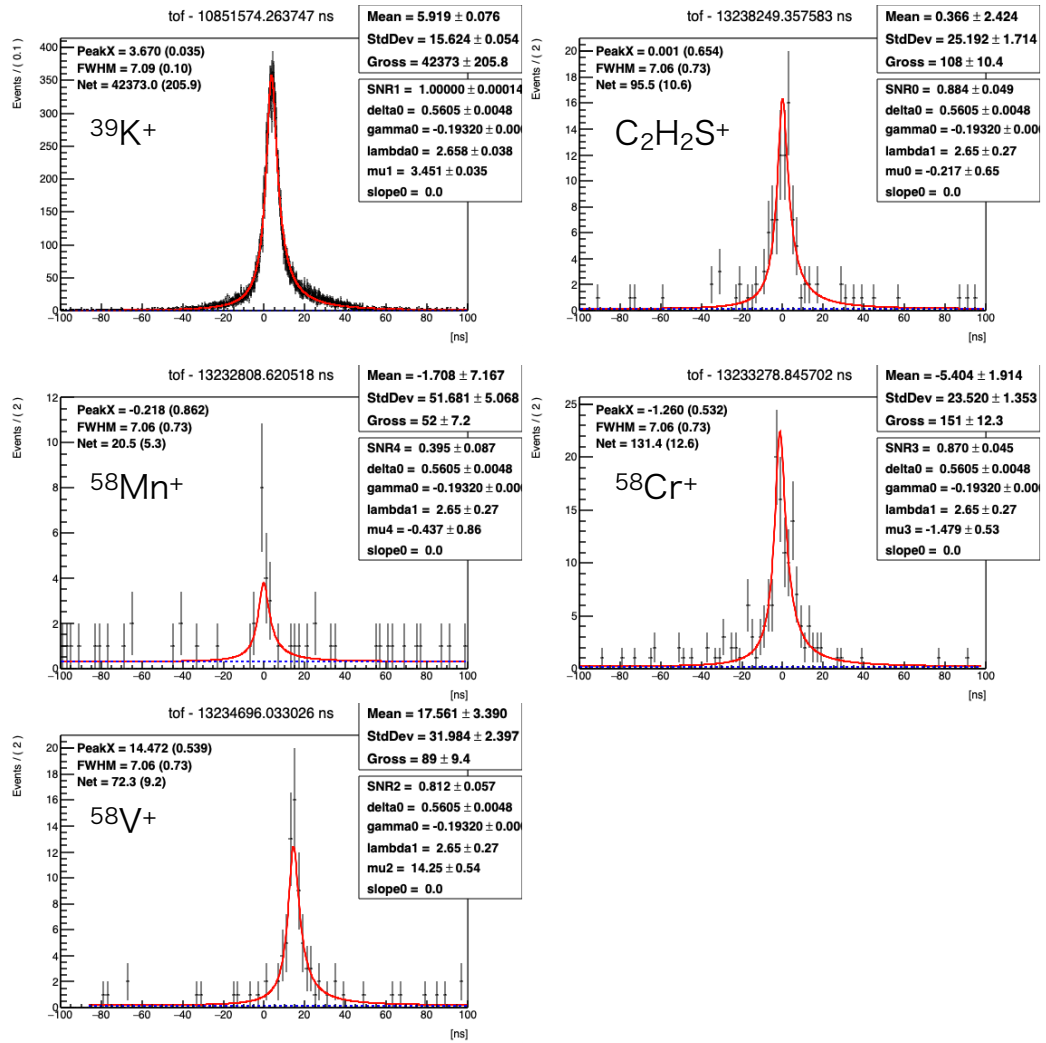
Figure 5.8. Plots of the TOF spectrum with the unbinned likelihood global fitting results. The center of '0 ns' on the horizontal axis is determined by use of the literature value of $C_2H_2S^+$ molecule. The TOF value of $C_2H_2S^+$ is used as a reference for the conversion from TOF to atomic mass.

Using [Eq. (5.1)], the mass can be obtained as shown in the following table 5.2.

Table 5.2. Each TOF obtained by fitting and masses deduced by [Eq. (5.1)]. The t_0 was 170 (3) ns, determined from both $C_2H_2S^+$ and K^+ TOFs.

Ion	TOF [ns]	Mass excess [keV]
$C_2H_2S^+$	13238249.36 (65)	reference [21Hu]
$^{58}V^+$	13234710.51 (54)	-40312.6 (69)
$^{58}Cr^+$	13233277.59 (53)	-52002.2 (69)
$^{58}Mn^+$	13232808.40 (86)	-55829.4 (88)

The error σ_{m_x} is deduced with the following equation,

$$\sigma_{m_x} = \sqrt{\left(\frac{\partial m_x}{\partial t_x}\sigma_{t_x}\right)^2 + \left(\frac{\partial m_x}{\partial t_r}\sigma_{t_r}\right)^2 + \left(\frac{\partial m_x}{\partial m_r}\sigma_{m_r}\right)^2 + \left(\frac{\partial m_x}{\partial t_0}\sigma_{t_0}\right)^2 + \left(\frac{\partial m_x}{\partial m_e}\sigma_{m_e}\right)^2}, (5.6)$$

where σ_{t_x} and σ_{t_r} are peak fitting errors of the analyte and reference ions originated from their statistics, σ_{m_r}, σ_{t_0}, and σ_{m_e} are the uncertainty of reference mass from the literature [21Hu], the error of TOF offset t_0, and the uncertainty of electron mass [21Hu], respectively. It should be noted that t_0 and its error σ_{t_0} are determined from TOFs of two molecular ions.

Table 5.3. Typical error components of [Eq. (5.6)] .

Component	Deviation [keV]
$\frac{\partial m_x}{\partial t_x}\sigma_{t_x}$	7.0
$\frac{\partial m_x}{\partial t_r}\sigma_{t_r}$	5.3
$\frac{\partial m_x}{\partial m_r}\sigma_{m_r}$	1.3×10^{-3}
$\frac{\partial m_x}{\partial t_0}\sigma_{t_0}$	1.0×10^{-2}
$\frac{\partial m_x}{\partial m_e}\sigma_{m_e}$	1.2×10^{-11}
σ_{m_x}	8.8

Typical values of the error components are given in the Table 5.3. Those values are on the mass on ^{58}Mn$^+$ using C$_2$H$_2$S$^+$ as a mass reference in Table 5.2. As main error components are the statistical errors associated with the peak fitting of the analyte and reference ions, error components of isobaric molecular ion, σ_{m_r} and σ_{t_0} are negligible. However, the σ_{m_r} becomes non-negligible in case of reference ion with less accuracy of mass in the literature [21Hu], such as ^{55}Sc$^+$ as mentioned in Sec. 6.1.

5.2.4 Experimentally determined masses with errors

In the on-line experiment, the TOF of analyte ion was different for each run because the mirror voltage and other parameters on MRTOF were adjusted run by run. Therefore, the data for each run were analyzed independently even though same isotope. For example, Fig. 5.9 shows the result of the experimentally determined mass of ^{58}Cr isotope for each run. In order to obtain the final result of mass $\bar{x}$, the weighted average was adopted, which was calculated by the following equation,

$$\bar{x} = \frac{\sum w_i x_i}{\sum w_i}, \qquad (w_i = \sigma_i^{-2}). \tag{5.7}$$

The error was calculated by the following weighted standard deviation formula.

$$\sigma = \sqrt{\frac{\sum w_i (x_i - \bar{x})^2}{(n-1)\sum w_i}} \tag{5.8}$$

Table 5.4 shows our experimental values of masses on isotopes of interest. For further details of the analysis for isotopes as shown in Appendix 1.
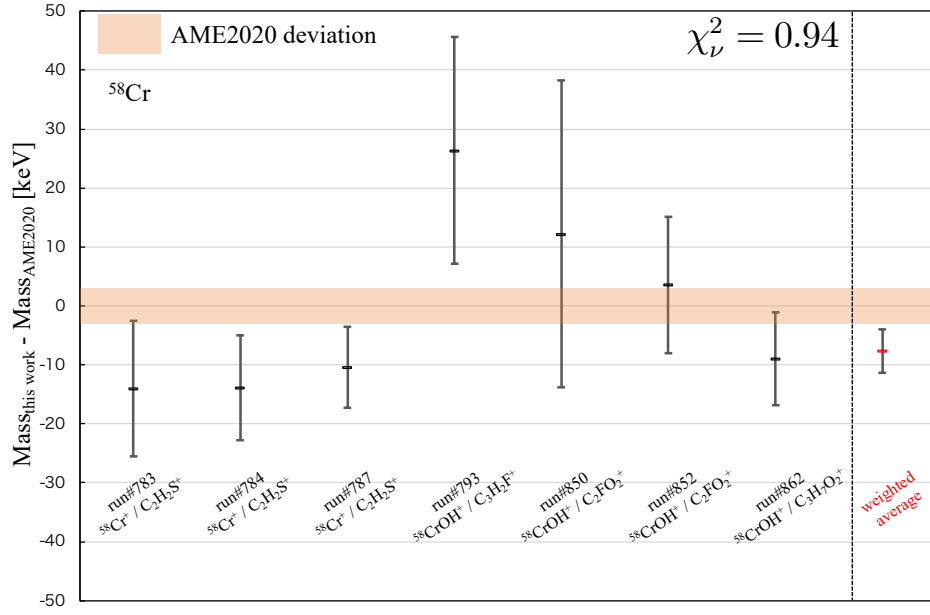
Figure 5.9. Masses obtained for each run (7 points on the left) for ^{58}Cr isotope and their weighted average (red point).

Table 5.4. Result of the mass measurements. Ions of interests and reference ions are analyte ions and mass references for mass calibrations, respectively. The stable nuclide of H, C, N, O, F, S, and Ar expressed in the reference ion are ^{1}H, ^{12}C, ^{14}N, ^{16}O, ^{19}F, ^{32}S, and ^{40}Ar, respectively.

Nuclide	Mass excess (keV)	Ions of interrest	Reference ion [21Hu]
^{55}Sc	-30853 (28)	^{55}ScOH$^+$	^{55}TiOH$^+$
^{56}Ti	-39408 (7)	^{56}Ti$^+$	N_4^+
^{58}Ti	-31442 (4)	^{58}TiOH$^+$	$C_3H_2F^+$, $C_2FO_2^+$, $C_3H_7O_2^+$
^{55}V	-49146 (92)	^{55}VOH$^+$	^{55}TiOH$^+$
^{56}V	-46260 (6)	^{56}V$^+$	N_4^+
^{57}V	-44383 (15)	^{57}V$^+$	ArOH$^+$
^{58}V	-40306 (6)	^{58}V$^+$, ^{58}VOH$^+$	$C_2H_2S^+$, $C_3H_2F^+$, $C_2FO_2^+$, $C_3H_7O_2^+$
^{59}V	-37802 (3)	^{59}V$^+$, ^{59}VO$^+$, ^{59}VOH$^+$	^{59}Cr$^+$, $C_3HF_2^+$, $C_2FO_2^+$, $C_3H_7O_2^+$, CS_2^+
^{56}Cr	-55295 (5)	^{56}Cr$^+$	N_4^+
^{57}Cr	-52536 (12)	^{57}Cr$^+$	ArOH$^+$
^{58}Cr	-51999 (4)	^{58}Cr$^+$, ^{58}CrOH$^+$	$C_2H_2S^+$, $C_3H_2F^+$, $C_2FO_2^+$, $C_3H_7O_2^+$
^{59}Cr	-48105 (5)	^{59}CrOH$^+$	CS_2^+
^{57}Mn	-57496 (15)	^{57}Mn$^+$	ArOH$^+$
^{58}Mn	-55829 (6)	^{58}Mn$^+$	$C_2H_2S^+$
^{59}Mn	-55525 (5)	^{59}Mn$^+$	^{59}Cr$^+$

6 Discussion

6.1 Comparison with AME2020

The analysis shown in the previous chapter has resulted in the determination of the masses on 15 nuclides. Table 6.1 shows our experimental values of the mass excess on isotopes of interest, the values from AME2020 [21Hu], and the differences between our values and ones from AME2020. These differences are shown in Fig. 6.1.

Table 6.1. Result of the mass measurements, with comparison of the values from the AME2020 [21Hu]. Mass excess, Literature and Difference indicate our experimental values, the values from AME2020 [21Hu] and the differences between our values and the ones from AME2020, respectively.

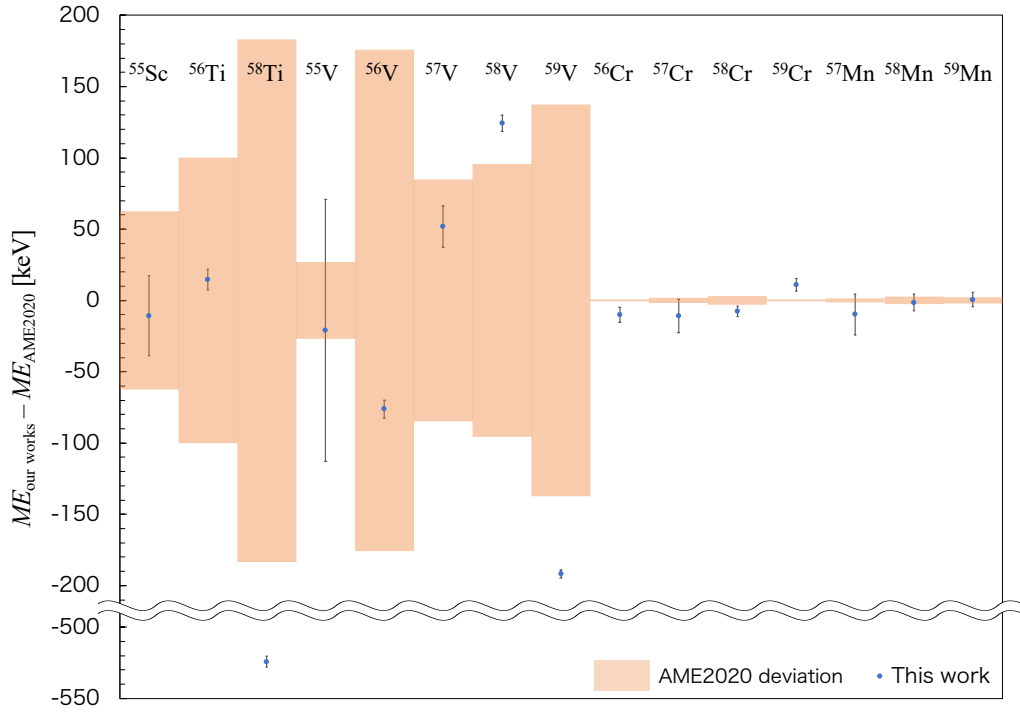| Nuclide	Mass excess (keV)	AME2020 (keV)	Diffrence (keV)
^{55}Sc	-30853 (28)	-30840 (60)	-11 (66)
^{56}Ti	-39408 (7)	-39420 (100)	15 (100)
^{58}Ti	-31442 (4)	-30920 (180)	-524 (180)
^{55}V	-49146 (92)	-49125 (27)	-21 (96)
^{56}V	-46260 (6)	-46180 (180)	-76 (180)
^{57}V	-44383 (15)	-44440 (80)	52 (81)
^{58}V	-40306 (6)	-40430 (100)	124 (100)
^{59}V	-37802 (3)	-37610 (140)	-192 (140)
^{56}Cr	-55295 (5)	-55285.1 (0.6)	-10 (5)
^{57}Cr	-52536 (12)	-52525.0 (1.9)	-11 (12)
^{58}Cr	-51999 (4)	-51991.8 (3.0)	-8 (5)
^{59}Cr	-48105 (5)	-48115.9 (0.7)	11 (5)
^{57}Mn	-57496 (15)	-57486.3 (1.5)	-10 (15)
^{58}Mn	-55829 (6)	-55827.6 (2.7)	-1 (6)
^{59}Mn	-55525 (5)	-55525.3 (2.3)	1 (6)

Figure 6.1. Mass differences between our values and the ones from AME2020[21Hu].

As shown in Fig. 6.1, our experimentally determined values of $^{56-59}$Cr and $^{57-58}$Mn are consistent with ones on AME2020 within the uncertainties, which have been already obtained with high precision within several keV. Experimental value in this work of ^{55}V has relatively low precision with 92 keV due to the low statistics for the setting of BigRIPS+ZDS. The one of ^{55}Sc (with 28 keV precision) has also relatively low precision since the reference ion of ^{55}TiOH including a radioactive isotope does not have relatively high precision, but the precision of our value is improved with a factor of two, compared with one in AME2020. Masses of other ^{56,58}Ti and ^{56,57,58,59}V were determined within improved errors of roughly one order of magnitude, compared with those in AME2020, due to our high precision mass measurement with MRTOF. The precisions on seven nuclides of ^{55}Sc, ^{56}Ti, ^{58}Ti, ^{56}V, ^{57}V, ^{58}V, and ^{59}V have been significantly improved. Also, it is interesting that our experimental values of ^{58}Ti, ^{58}V and ^{59}V are deviated from ones on AME2020, over the uncertainties on AME2020 as shown in Fig. 6.1. Those differences are 0.52 MeV for ^{58}Ti, 0.12 MeV for ^{58}V and 0.19 MeV for ^{59}V, respectively. It is noted that ^{58}Ti and ^{59}V were

not measured and the precision of ^{58}V was relatively large with TITAN-MRTOF [21Du]. These deviations are discussed in Sec. 6.3.

6.2   Blind analysis

In order to confirm the correctness of this new analysis procedure in this work, two persons, the author and Dr. M. Rosenbusch had performed the analysis simultaneously and independently. Dr. Rosenbusch used a different analysis method. The drift correction in his procedure was the traditional method (see in Chap. 5.1), and the peak fitting was performed by using a function obtained from sampling the reference ion peak in the same TOF spectrum. The peak position, peak width, and peak height of the sampling function were set as free parameters when fitting the most intense peak of mass reference ion. The peak width was then fixed for fitting other peaks in the same spectrum.
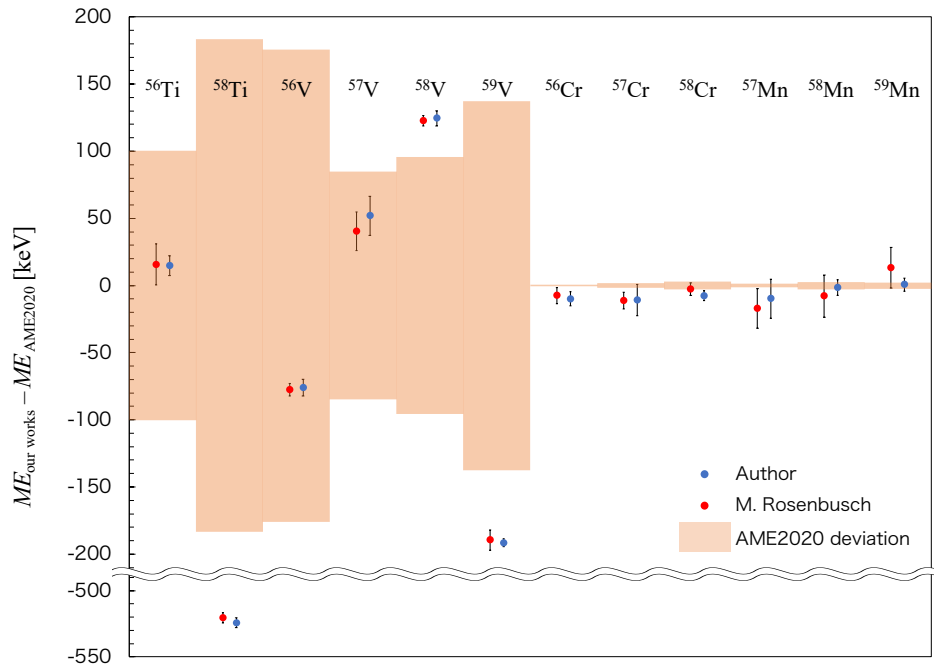

Figure 6.2. Comparison of determined mass by independent analysis procedures. Red and blue circles indicate the masses obtained by Dr. M. Rosenbusch, and the author, respectively.

A comparison of the mass excesses obtained by two independent analyses is shown in Fig. 6.2. The masses obtained from the two independent analyses are consistent within one sigma,

and there are no systematic error. Therefore, the determination process of masses in our analysis are confirmed.

6.3   Deviations on ⁵⁸V, ⁵⁹V, and ⁵⁸Ti from previous measurements

In this experiment, the masses on ^{58}V, ^{59}V, and ^{58}Ti are disagreement with the ones over the uncertainties on AME2020 [21Hu]. The masses on the AME were evaluated from the experimental values that had been measured previously. Figures 6.3, 6.4, and 6.5 shows the comparisons on mass excesses experimentally obtained by previous studies and ours, for ^{58}V, ^{59}V, and ^{58}Ti, respectively.
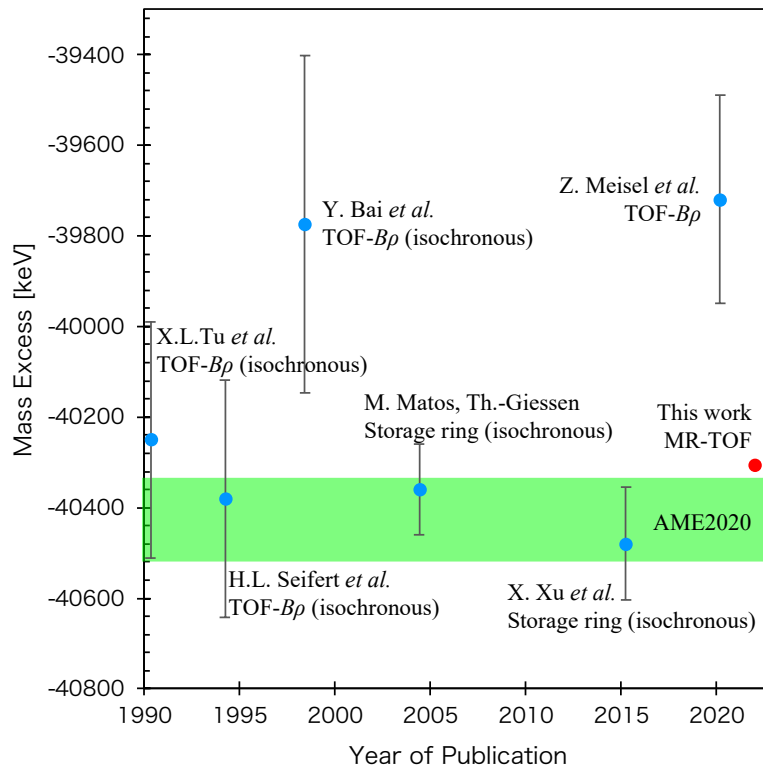

Figure 6.3. Comparisons of ^{58}V mass excesses with all previous measurements (blue circles) from [90Tu,94Se,98Ba,04Ma,15Xu,20Me], AME2020 (green band) and in this work (red circle).

The comparison of the ^{58}V mass excesses is shown as function of the year of publication in Fig. 6.3. The AME2020 combines the results by TOFI method in Los Alamos

[90Tu,94Se,98Ba], by GSI storage-ring (isochronous) measurements [04Ma], by IMP storage-ring (isochronous) measurements [15Xu], and by NSCL TOF measurements [20Me].

Mass excess of ^{58}V, as shown in Fig. 6.3, can be categorized into two groups: the differences from AME are about from -60 to 180 keV, and about from 650 to 710 keV. Our result belongs to the former group and are in particularly good agreement with one from Los Alamos [94Se] and one from GSI [04Ma] with error bar. On the other hand, it was about 590 keV lighter than the NSCL result [20Me].
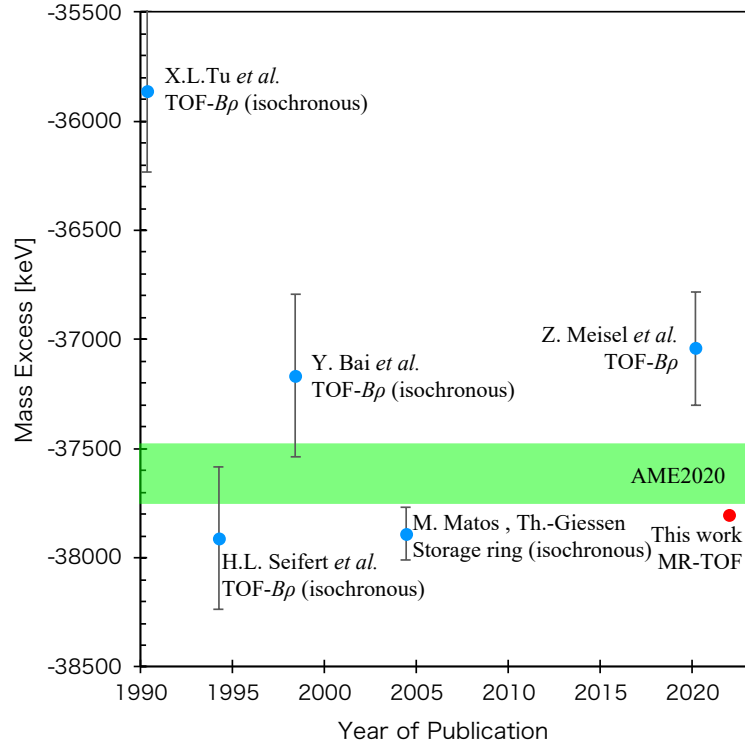

Figure 6.4. Comparisons of ^{59}V mass excesses with all previous measurements (blue circles) from [90Tu,94Se,98Ba,04Ma,20Me], AME2020 (green band) and in this work (red circle).

The comparison of the ^{59}V mass measurements is shown in Figure 6.4. The AME was evaluated using the mass excess in References of [90Tu,94Se,98Ba,04Ma,20Me].

Most of mass excess of ^{59}V also can be categorized into two groups: the differences from

the AME are about from -300 to -270 keV and about from 440 to 580 keV, except for Los Alamos in 1990 [90Tu]. Similarly, our result belongs to the former group and are in good agreement with those of Los Alamos [94Se] and GSI [04Ma]. On the other hand, it is about 760 keV lighter than the NSCL result [20Me].
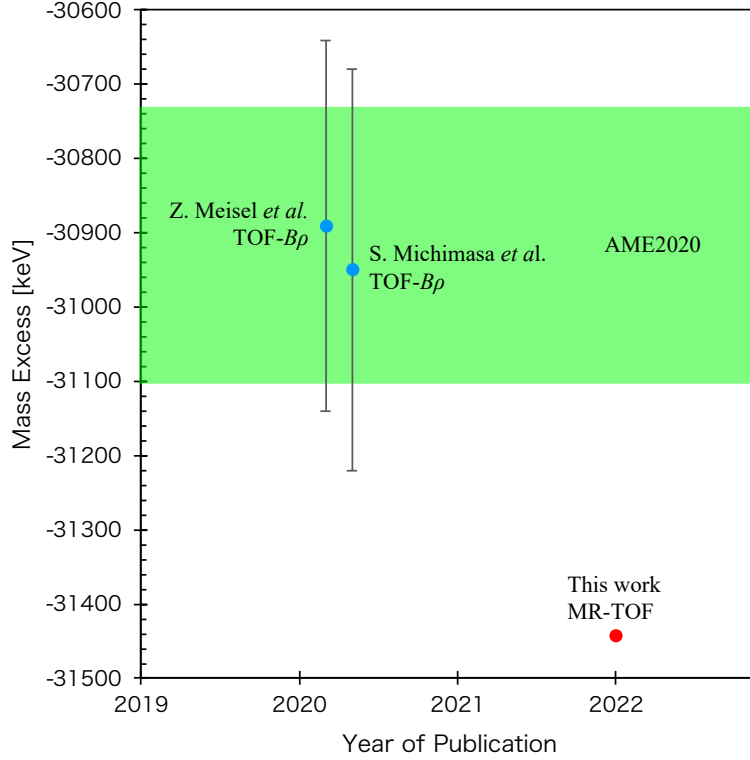

Figure 6.5. Comparisons of ^{58}Ti mass excesses with all previous measurements (blue circles) from [20Me,20Mi], AME2020 (green band), and in this work (red circle).

The mass of ^{58}Ti was measured in 2020 for the first time at the NSCL TOF measurement [20Me] and the RIKEN RIBF TOF measurement [20Mi], and the AME was evaluated with these two reported values. The two results are in good agreement within error bar, which leads to a small weighted error estimated on the AME.

Our result is about 530 keV lighter than the AME, which is the similar trend compared to NSCL [20Me] with the same TOF-$B\rho$ method shown at ^{58,59}V mentioned above.

As a summary of these deviations on ^{58,59}V and ^{58}Ti, our experimental results are consistent

with previous measurements except for ones by recent TOF-$B\rho$ measurements [20Me, 20Mi]. In general, the TOF-$B\rho$ method uses an isotope with a well-known mass as reference, causing a larger uncertainty towards the neutron-rich side. Furthermore, the required TOF resolution is also severe, where 1 ns time difference corresponds to mass difference of about 1 MeV.

6.4 Neutron sub-shell $N = 32$, 34 in pf-shell

Most of the uncertainties in the mass values (or MEs) obtained in this work are below 28 keV, which lead the improvements up to about one order of magnitude compared to the reported uncertainties in AME2020[21Hu]. The nuclides with updated uncertainties (in red) are shown in the nuclear chart in Fig. 6.6. The present results allow a detailed discussion in the isotopes of Sc, Ti, and V with $N = 32$ and 34 by using two-neutron separation energies S_{2n} and one-neutron separation energies S_n.

Proton number	N=31	N=32	N=33	N=34	N=35	N=36	N=37
24	^{55}Cr 0.23 keV	^{56}Cr 0.6 keV	^{57}Cr 1.9 keV	^{58}Cr 3.0 keV	^{59}Cr 0.7 keV	^{60}Cr 1.1 keV	^{61}Cr 1.9 keV
23	^{54}V 11 keV	^{55}V 27 keV	^{56}V 180 keV ↓ **6 keV**	^{57}V 80 keV ↓ **15 keV**	^{58}V 100 keV ↓ **6 keV**	^{59}V 140 keV ↓ **3 keV**	^{60}V 180 keV
22	^{53}Ti 2.9 keV	^{54}Ti 16 keV	^{55}Ti 29 keV	^{56}Ti 100 keV ↓ **7 keV**	^{57}Ti 210 keV	^{58}Ti 180 keV ↓ **4 keV**	^{59}Ti Unknown
21	^{52}Sc 3 keV	^{53}Sc 18 keV	^{54}Sc 14 keV	^{55}Sc 60 keV ↓ **28 keV**	^{56}Sc 260 keV	^{57}Sc 180 keV	^{58}Sc 190 keV
20	^{51}Ca 0.5 keV	^{52}Ca 0.7 keV	^{53}Ca 40 keV	^{54}Ca 50 keV	^{55}Ca 160 keV	^{56}Ca 250 keV	^{57}Ca Unknown

Proton number (vertical axis) — Neutron number (horizontal axis)

Figure 6.6. Mass uncertainties of neutron rich calcium, scandium, titanium, and vanadium isotopes on part of nuclear chart. Black and red numbers are the uncertainties from AME2020[21Hu] and ones in this work, respectively.

6.4.1 Two-neutron separation energy and empirical shell gap

Two-neutron separation energy (S_{2n}), defined in [Eq. (6.1)], reveals the behavior of the interrelated shells,

$$
\begin{aligned}
S_{2n}(Z,N) &= [m(Z,N-2) + 2m_n - m(Z,N)]c^2 \\
&= B(Z,N) - B(Z,N-2) \\
&= ME(Z,N-2) - ME(Z,N) + 2(m_n - u),
\end{aligned}
\tag{6.1}
$$

where m, m_n, B, ME, and u are atomic mass, neutron mass, binding energy, mass excess, and atomic mass unit, respectively. In [Eq. (6.1)], the neutron separation energy is directly derived from the mass difference between the isotopes. From a systematic trend of the S_{2n} of a certain isotope chain, a rapid drop of S_{2n} represents a shell closure where the binding of the next two neutrons becomes suddenly weak, and a flat behavior of S_{2n} indicates the shell structure does not change very much.

Figure 6.7 shows the S_{2n} on each isotopic chain of N = 27 - 44 and Z = 19 - 26. The colored dots and lines except for red ones indicate the experimental data evaluated in AME2020 and recent experimental data [20Me, 20Mi], and red ones indicate experimental data including our experimental values. The S_{2n} decreases with increasing neutron number and the binding energy becomes weaker towards the neutron drip line as a general trend. The large kinks appear at canonical magic number N = 28 on the chains from Z = 19 (K) to 23 (V) appear. Also, clear kinks appear at sub-magic number N = 32 and $Z \sim$ 20 (Ca) isotope with proton magic number.

In Fig. 6.7, theoretical calculation are also plotted. This calculation indicated by dashed line in Fig. 6.7 is the microscopic theoretical calculation with the valence-space formulation of the in-medium similarity renormalization group (VS-IMSRG). This prediction was used for the comparisons with experimental values in latest mass measurements on Sc isotopes in [21Le]. This model roughly reproduces trends of S_{2n} on those isotope chains.
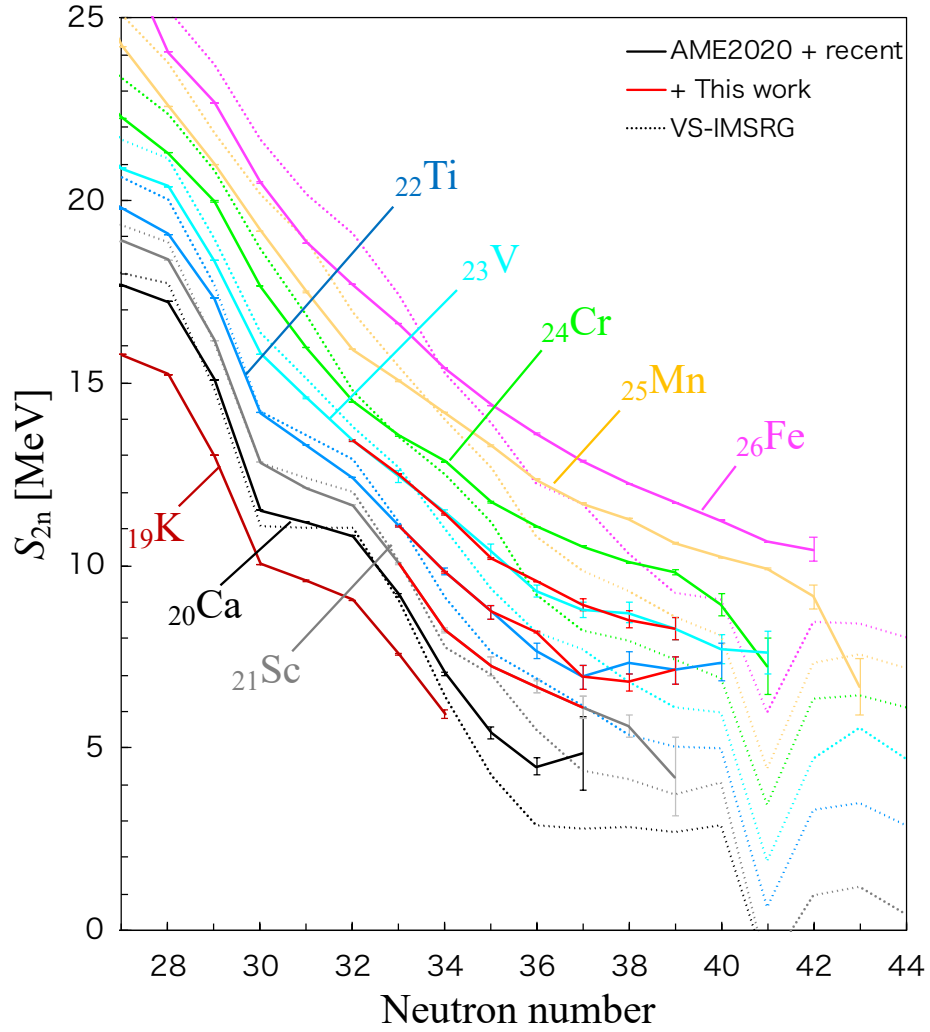
Figure 6.7. Two neutron separation energies of neutron-rich K, Ca, Sc, Ti, V, Cr, Mn, and Fe region as function of neutron number. Each line color show isotopic chain of each element. Solid lines are experimental values by AME2020[21Hu] included recent measurements [20Me,20Mi], Red line is updated value by this work. Dotted lines and dashed lines are theoretical models VS-IMSRG [21St] and LZU [19Ma],
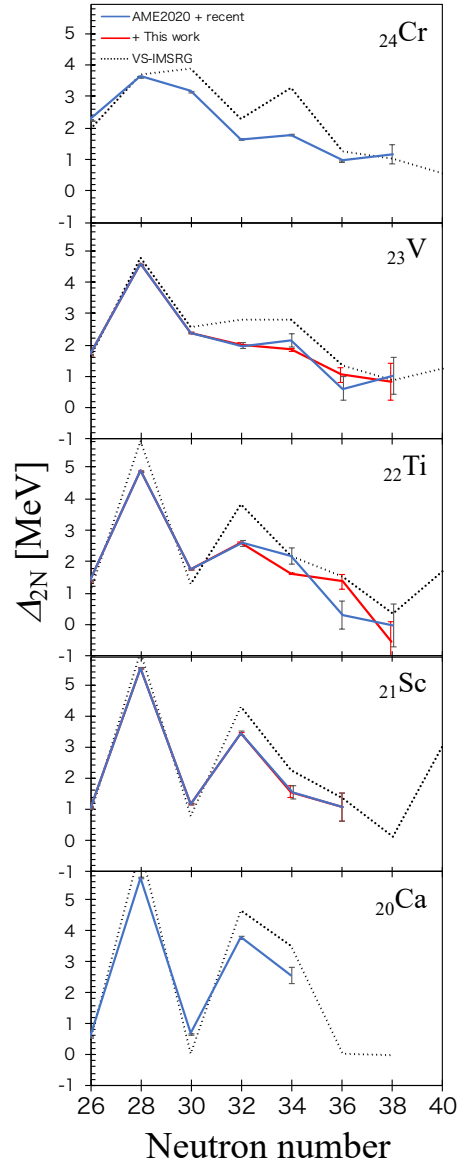
Figure 6.8. Empirical shell gap Δ_{2n} of neutron-rich Ca, Sc, Ti, V, and Cr isotopes. Data is from AME2020 [21Hu] + recent [20Me,20Mi] (blue) with our data (red) as function of neutron number. Dotted line represents theoretical calculations on the model of VS-IMSRG [21St].

In order to investigate the shell gap by using the two-neutron separation energy, the empirical neutron-shell gap (Δ_{2n}) is defined by the following equation,

$$\Delta_{2n}(Z,\ N) = S_{2n}(Z,\ N) - S_{2n}(Z,\ N+2)$$
$$= 2B(Z,\ N) - B(Z,\ N-2) + B(Z,\ N+2). \qquad (6.2)$$

As can be seen from the [Eq. (6.2)], Δ_{2n} indicates the systematic changes of the slopes of S_{2n}. This is often used to identify shell effects. The Δ_{2n} results for the isotopes in this study are shown in Fig. 6.8 as a function of neutron number and in Fig. 6.9 as a function of proton number, respectively, together with the theoretical model of VS-IMSRG [21St].

In Fig. 6.8, in all isotopes, a strong shell effect for experimental and theoretical Δ_{2n} is seen at $N = 28$, the classical magic number. For Ca, the height of experimental Δ_{2n} peak at $N = 28$ is about 6 MeV and is close to zero at $N = 26$ and $N = 30$. The height of peaks up to 4 MeV are also observed at $N = 32$ and 3 MeV at $N = 34$. Thus, for Ca isotopes, the closed shell effects are clearly seen at $N = 28$, $N = 32$, and 34 [18Mi].

For Sc isotopes as shown in Fig. 6.8, experimental Δ_{2n} are updated on $N = 32$ and $N = 34$ in this work (red line). Those data are well consistent with the values from AME2020 (blue line). Therefore, the peak of the shell gap on $N = 32$ and no existence of the peak on $N = 34$ for Sc isotopes, which were discussed in ref. [21Le], are confirmed in this work.

For Ti isotopes, experimental Δ_{2n} are updated from $N = 32$ to $N = 38$ in this work (red line). On $N = 32$, the peak of the shell gap is clearly observed, however the height of the peak is 2.6 MeV, lower than ones in Ca and Sc, and higher than ones in V, Cr, Fe, as shown in Fig. 6.9. Therefore, closed shell behavior still remains on $N = 32$ in Ti isotope. Also, at around $N = 34$, the peak shape (parabola shape) is seen in the Δ_{2n} from AME2020 (blue line), however in our updated Δ_{2n} the shape is vanished and monotonic drops toward $N = 38$ is observed. Therefore, no existence of the closed shell effect on $N = 34$ in Ti isotope is suggested. The updated Δ_{2n} on $N = 34$ in Ti is 1.6 MeV, which is similar to ones in Sc, V, Cr and Fe as shown in Fig. 6.9. This also supports the vanishment of closed shell effect on $N = 34$ in Ti isotopes.

For V isotopes, experimental Δ_{2n} are updated from $N = 32$ to $N = 38$ in this work (red line). The updated Δ_{2n} has a monotonic drop toward $N = 40$, suggesting no existence of closed shell effect on $N = 32$ and 34. It should be noted that the Δ_{2n} around $N = 34$ from the AME2020 (blue line) data has large errors in Ti and V, making it difficult to understand the detailed structure. In the present data, the Δ_{2n} at $N = 34$ are obtained with higher

precision and are slightly smaller in both cases relative to AME2020 values, clearly suggesting the disappearance of the closed shell effect on $N = 34$ in Ti and V.
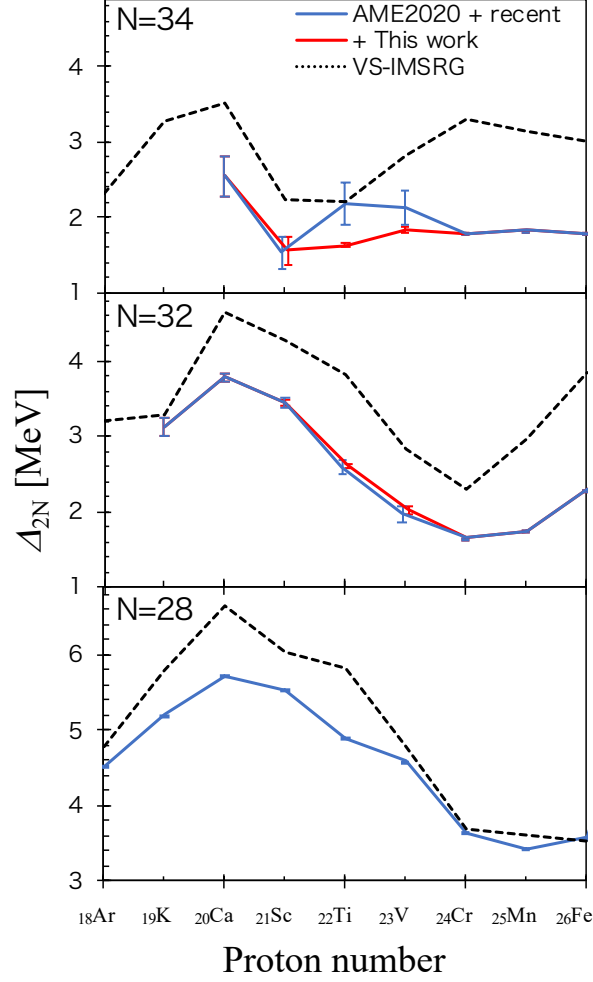

Figure 6.9. Empirical shell gap Δ_{2n} for isotones with the canonical magic number of $N = 28$, the new magic $N = 32$, and 34. Data is from the AME2020 [21Hu] with recent measurements [20Me, 20Mi] (blue line), and with our work (red line). The theoretical calculation on the model of VS-IMSRG is indicated by dotted lines.

On the other hand, theoretical calculation on the model of VS-IMSRG (dotted line) is also shown in Fig. 6.8 and 6.9. The VS-IMSRG calculation, although it cannot reproduce S_{2n} so much in Fig. 6.7, can reproduce zigzag pattern well. However, VS-IMSRG calculation

often overestimates the experimental values in Fig. 6.8 and 6.9. The differences between experimental and theoretical values in nuclei with $N = 32\text{-}38$ are roughly 1 - 2 MeV. Especially, large overestimation appears on V and Cr isotopes.

6.4.2   One neutron separation energy and neutron pair correlation

In order to extract further information on nuclear structure systematically by using improved experimental masses, one-neutron separation energy (S_n) and paring energy deduced from S_n are discussed in this section. S_n is defined as follows

$$S_n(Z,N) = [m(Z,N-1) + m_n - m(Z,N)]c^2$$
$$= B(Z,N) - B(Z,N-1)$$
$$= ME(Z,N-1) - ME(Z,N) + m_n - u. \tag{6.3}$$

As well as the two-neutron separation energy, this is also a quantity obtained directly from mass. Figure 6.10 shows the S_n on each isotopic chain of $N = 27$ - 44 and $Z = 19$ (K) $- 26$ (Fe). The colored lines except for red ones indicate the experimental data taken from AME2020 [21Hu] and recent experimental data [20Me,20Mi], and red ones indicate those experimental data + our experimental values.

Figure 6.10. One neutron separation energies of neutron-rich K, Ca, Sc, Ti, V, Cr, Mn, and Fe isotopes as a function of neutron number. Each line color shows isotopic chain of each element. Solid lines are experimental values by AME2020 [21Hu] included recent measurements [20Me,20Mi]. Red lines are updated values in this work.

The S_n decreases with increasing neutron number and the binding energy becomes smaller towards the neutron drip line ($S_n = 0$) as a global trend. The local trends show a zigzag pattern depending on the even-odd number of neutrons. This trend indicates that the binding energy increases with neutron pairing.
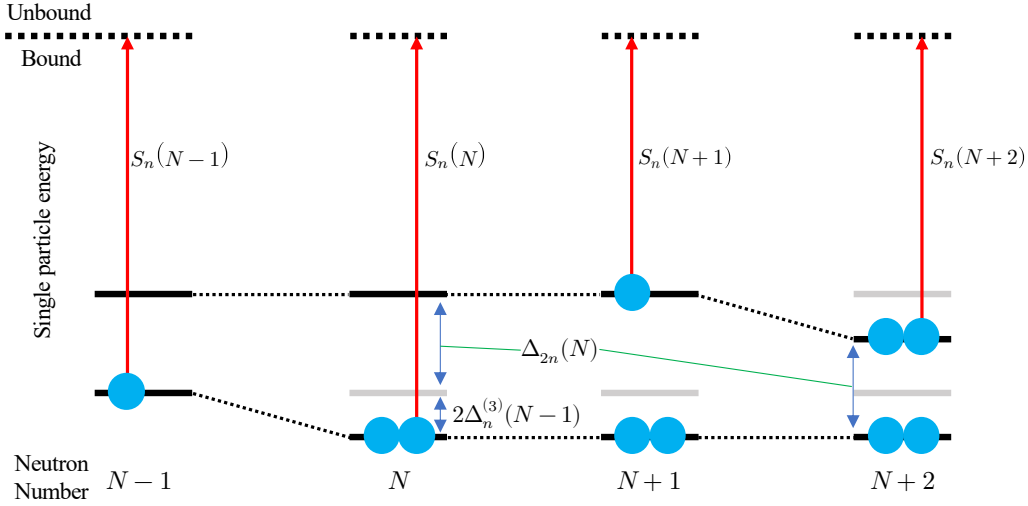

Figure 6.11. Schematic drawing of single particle energy for neutron and relationship between neutron separation energies and paring energies.

Figure 6.11 shows a schematic drawing of the neutron single-particle energy and the relationship between neutron-separation energies and neutron paring energies. As shown in Fig. 6.11, the Fermi level of the nucleus approaches the unbound level with increasing neutron number, thus the overall systematics of S_n decreases, however, due to pairing interaction, ground state energy at $N = \text{even}$ is lower than that at $N - 1$, therefore a zigzag pattern is observed. Here, $\Delta_n^{(3)}$ corresponds the pairing gap parameter, which is expressed as the difference in neutron separation energy by the following equation,

$$\Delta_n^{(3)}(Z, N) = \frac{(-1)^N}{2}[2B(Z, N) - B(Z, N - 1) + B(Z, N + 1)]$$

$$= \frac{(-1)^N}{2}[S_n(Z, N) - S_n(Z, N + 1)]. \tag{6.4}$$

The $\Delta_n^{(3)}$ is experimentally extracted from odd-even staggering (OES) of binding energies (B) by three-point filter [98Sa]. In the reference [02Hi], $\Delta_n^{(3)}(N = \text{odd})$ is

presented as the best suited method for the extraction of paring gap parameters from experimental data. The $\Delta_n^{(3)}(N = \text{odd})$ for the isotopes of Ca, Ti, V, Cr, Fe in this work are shown in Fig. 6.12(a) as a function of neutron number together with the theoretical calculations [21St,19Ma].
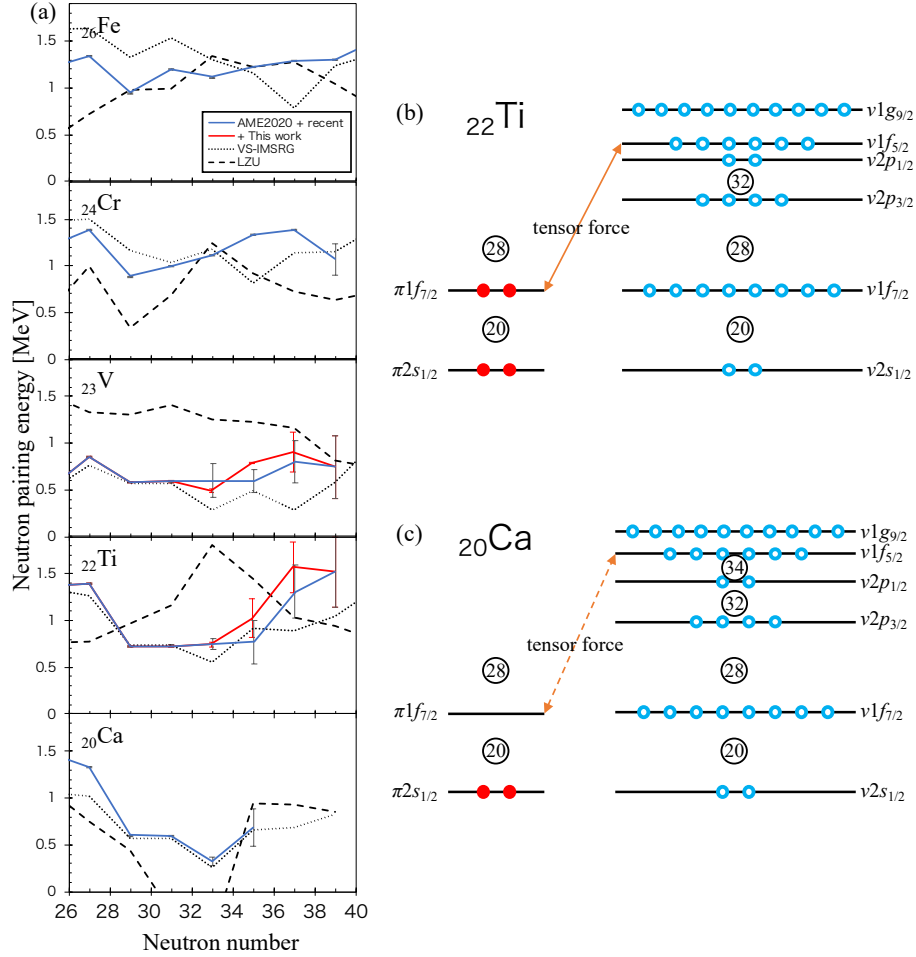

Figure 6.12. (a) Neutron paring parameters $\Delta_n^{(3)}$ of neutron-rich Ca, Ti, V, Cr, and Fe isotopes taken from AME2020 [21Hu] including recent measurements [20Me,20Mi] (blue) and our data (red) as a function of neutron number (N = odd). Dotted lines and dashed lines are theoretical calculations on the models of VS-IMSRG [21St] and LZU [19Ma], respectively. Also, schematic illustrations of single-particle orbitals are shown for (b) Ti and (c) for Ca, respectively. The arrows indicate the attractive tensor force.

In Fig. 6.12 (a), for Ti and V isotopes, the updated $\Delta_n^{(3)}$ are provided from $N = 33$ - 37 in this work. In both cases, the uncertainties for $\Delta_n^{(3)}$ are largely improved, compared to the previous values, as shown in Fig. 6.12(a). Although no increase of previous $\Delta_n^{(3)}$ (blue line) was observed on $N = 35$ for Ti and V isotopes. An onset of the increase on the improved $\Delta_n^{(3)}$ has been clearly seen for the first time. And both cases of Ti and V, the increase of $\Delta_n^{(3)}$ are seen toward $N = 40$ in Fig. 6.12(a). On the other hand, the $\Delta_n^{(3)}$ of Ti isotopes at around $N = 40$ have higher values compared with Cr isotopes. However, the uncertainties of $\Delta_n^{(3)}$ of Ti isotopes at around $N = 40$ are still large for detailed discussion. This behavior has the potential to reveal shell evolution through comparison with microscopic theoretical calculations such as shell models. In next chapter, we will discuss the outlook of this issue.

7 Conclusion

 Nuclear magic numbers have been found on nuclei close to β-stability line. However, in neutron-rich nuclei, magic numbers disappear and new magic numbers appear, which has become the subject of intense research in recent years. At present neutron-rich nuclei can be produced at the highest intensity in the world at RIBF BigRIPS. Masses on these nuclei can be measured with high precision using MRTOF, which can be analyzed in just a few milliseconds. MRTOF mass measurement requires a slow RI beam with the energy of keV, although RI beam with several hundreds of MeV/nucleon provided by RIBF. In order to solve this challenge, we have developed the RFGC. And through our developments for RFGC and MRTOF which have been newly installed at RIBF BigRIPS as shown in this thesis, we have demonstrated efficient mass measurements with high precision.

 In our RFGC development, a newly designed electrode structure has been introduced and the transport conditions have been optimized at off-line tests. The transport efficiencies of more than 80% have been achieved for each electrode section by investigating conditions such as the gas pressure, RF frequency, and RF amplitude. The RFGC has been installed at the downstream of the BigRIPS beamline, which has been combined with the MRTOF. On-line experiments were performed symbiotically with the in-beam γ-ray spectroscopy experiments (HiCARI campaign), and many nuclei with $A =$ 40-140 were injected into our system. As the result, the transport efficiency of about 18 % in maximum was achieved for all system including RFGC and MRTOF. The robustness of the new electrode structure was confirmed by almost keeping the efficiency even at beam intensities above 8 kcps injection.

 Masses on more than 70 nuclides have been measured at the on-line experiment. In $A =$ 50-60, masses on 15 neutron-rich nuclei have been measured. Among them, the mass precisions of ^{55}Sc, ^{56}Ti, ^{58}Ti, ^{56}V, ^{57}V, ^{58}V, and ^{59}V have been significantly improved with several 10 keV or less uncertainties. Also, determined masses on ^{58}Ti, ^{58}V and ^{59}V have been deviated from values beyond the uncertainties in AME2020. Experimentally determined masses in this work with high precision enables to study the systematics of neutron separation energies. The empirical shell gaps Δ_{2n} evaluated from S_{2n} indicates that the peak at $N =$ 32 for Ti isotopes is clearly observed, suggesting a closed shell behavior at

$N = $ 32 for Ti isotopes. On the other hand, no peaks at $N = $ 34 for Sc, Ti and V isotopes are observed, suggesting no energy gap of $N = $ 34 while large shell gap at $N = $ 34 appears in Ca isotopes. Also, on the paring effect is discussed by $\Delta_n^{(3)}$ deduced from updated S_n, the onsets of the increasements at $N = $ 35 for Ti and V isotopes are clearly observed, supporting no energy gap at $N = $ 34. Our developed RFGC and MRTOF system enabled to systematical study of shell gap at $N = $ 32, 34 and paring effect as proton number changes from $Z = $ 20 to 23, with $N = $ 28 - 40.

8 Outlook

As mentioned in Sec. 6.4.2, the pairing energies of Ti isotopes at around $N = 40$ have higher values compared with Cr isotopes.

Here, we show experimental excitation energies of the first 2+ ($E(2_1^+)$) on Ca, Ti, Cr, Fe and Ni isotopes in Fig. 8.1. The $E(2_1^+)$ values on Cr and Fe isotopes gradually decrease toward $N = 40$. The similar tendency can be seen on Ti isotopes.

Figure 8.1. Experimental excitation energies of the first 2^+ state ($E(2_1^+)$) on Ca, Ti, Cr, Fe and Ni from NNDC On-Line Service [21NN].

Recently, $E(2_1^+)$ on ^{62}Ti ($N = 40$) was observed which is indicated by the plotted point on $N = 40$ of Ti in Fig. 8.1, and the author suggests a deformed ^{62}Ti ground state [20Co]. Also, the author suggests that configuration mixing between neutron fp and gd orbitals.

On the other hand, as shown in Fig. 6.12, the $\Delta_n^{(3)}$ of Ti isotopes at around $N = 40$ have higher values compared with Cr isotopes. Also, S_{2n} and Δ_{2n} indicate strong stabilities in the vicinity of ^{62}Ti as can be seen in Fig. 6.7 and 6.8. S. Michimasa et al., who have measured most exotic Ti isotopes to date, suggests that the strong stabilities in the vicinity of ^{62}Ti are affected by the Jahn-Teller effect [20Mi]. However, the experimental values of masses at around ^{62}Ti ($N = 40$) still have large uncertainties with about 200-500 keV. In order to obtain

the conclusion, we need further precise measurements on masses in the vicinity of ^{62}Ti. It is noted that the half-lives of Ti isotopes in the vicinity of ^{62}Ti are too short to measure the masse with our current RFGC/MRTOF system. Therefore, for the high precision mass measurement in the vicinity of ^{62}Ti, Rare RI Ring (R3) can be available at RIBF.

Further systematic mass measurements on neutron- and proton-rich radioactive isotopes are ready now. We have plans to perform mass measurements with our RFGC/MRTOF system in the regions as shown in the figure 8.2. We expect that these comprehensive mass measurements not only will provide information of detailed nuclear structure in each region, but also can provide impacts on the understanding of nucleosynthesis in the universe.

Figure 8.2. Regions for plans of mass measurements with our RFGC and MRTOF system in nuclear chart.

Acknowledgement

This thesis is not the result of only three years' work, but of several decades of on-going research and development. I am happy to have had the opportunity to make the first precise mass measurements at the new RIKEN RIBF facility, which has opened a new door to precision spectroscopy of exotic nuclei. I would like to thank all the people who have contributed to this story. Unfortunately, it would take many pages to introduce them all, and my memory is quite unprecise.

I would like to thank all RIKEN and KEK SLOWRI collaboration. It was really an exciting and precious time at Nishina center. I would like to start with Aiko Takamine of the SLOWRI team, who not only gave me tremendous experience and knowledge of RF handling techniques and gas cell developments, but also took great care of me, sometimes gently, sometimes harshly, and with a lot of jokes. I am also grateful to Marco Rosenbusch for instructing me all about mass measurement techniques through MRTOF and for his friendly advice and discussions on measurement and analysis methods. Hironobu Ishiyama has provided us with the best research environment as the SLOWRI team leader, and has helped me a lot in my thesis correction and conference preparation, and has even supported my promotion. I would also like to express my great appreciation to Michiharu Wada. It has been an irreplaceable asset for me to be able to research and development with Wada-san who is fascinating as a physicist and as one person. Also, I would like to thank Dongsheng Hou, Chen Sidong, Wenduo Xian, Izumi Yoshida, Sota Kimura, Peter Schury, Toshitaka Niwase, Tetsu Sonoda, Takao Kojima, Yuta Ito, Jiajian Liu, Shuxiong Yan, Yoshikazu Hirayama, Machiko Izawa, Yutaka Watanabe, Hiroari Miyatake, Takashi Hashimoto, Jun-young Moon, Momo Mukai, Satoshi Ishizawa, Kevin Murray, Tik Tsun Yeung, Shunji Nishimura, Sarah Naimi, Hermann Wollnik, Koura Hiroyuki, Shinichiro Michimasa, and all other members.

My warmest thanks also go to the members of the Nuclear Experiment Laboratory at Osaka University. Atsuko Odahara has been a great mentor to me since I was a master's student, and Odahara-san has given me a lot of valuable suggestions in physics discussions. Takahiro

Appendix

A. 1. TOF spectra of On-line experiments

Here we present some of the results of the experiments that could not be introduced in the body of thesis. Fig. A.1.-A.4. are Selected 4 runs out of 21 runs in total during the beam of mass number A = 50-60 region.
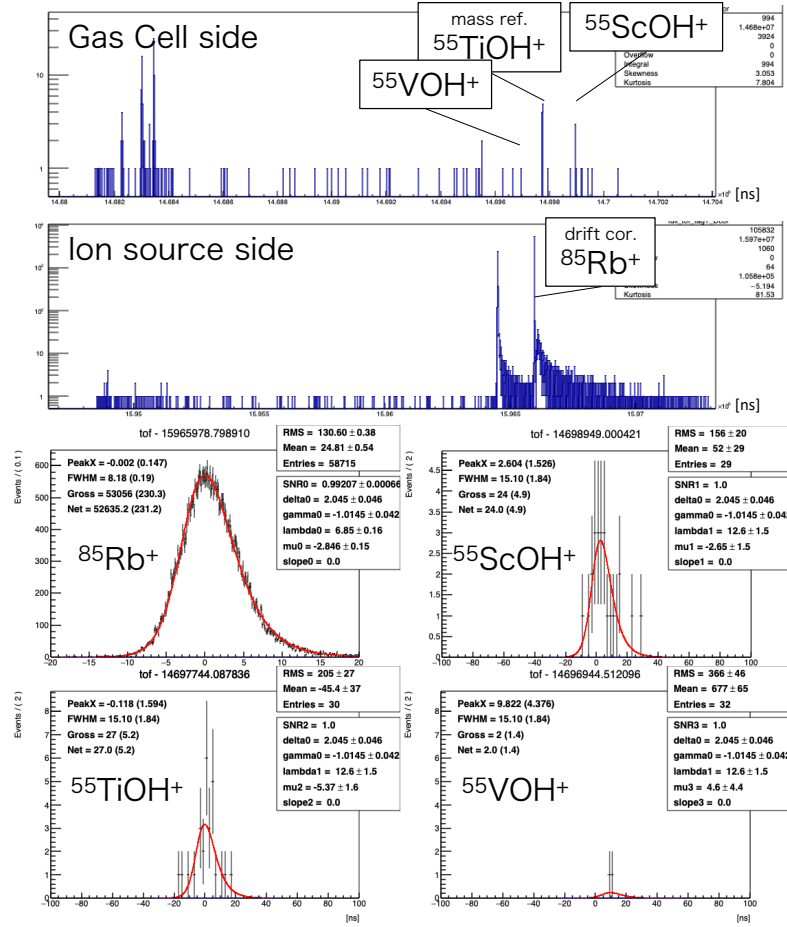

Figure A.1. TOF full spectrum obtained in the online experiment. These spectra were measured sequentially, alternating at 25 ms intervals between RFGC side and ion source side (upper panel). Fitting results of all peaks (lower panel). The center of '0 ns' on the horizontal axis is expected TOF calibrated by the reference literature mass. The TOF value of ^{55}TiOH$^+$ is used as a mass reference for the conversion from TOF to atomic mass.
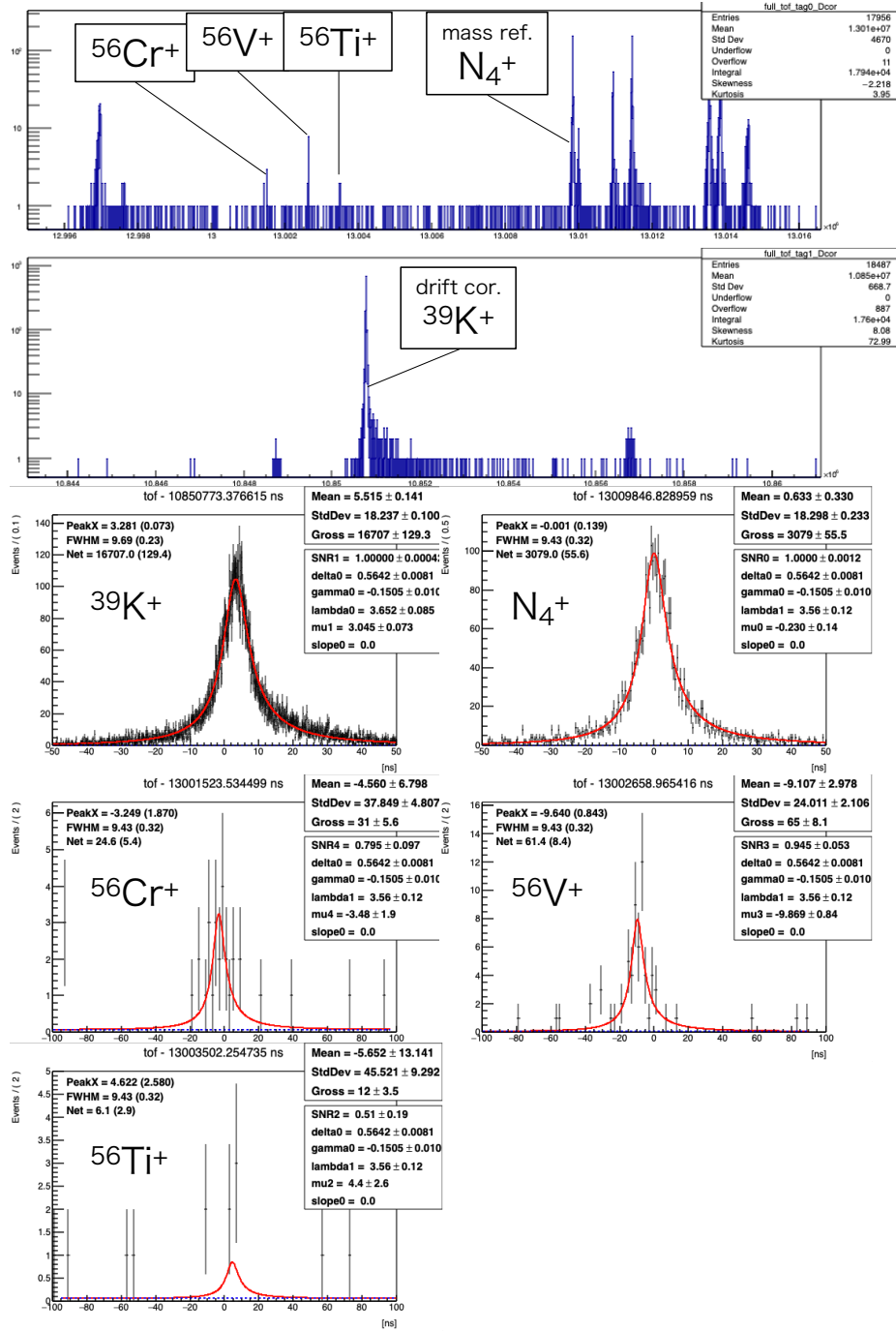
Figure A.2. TOF full spectrum obtained in the online experiment (upper panel). Fitting results of all peaks (lower panel).
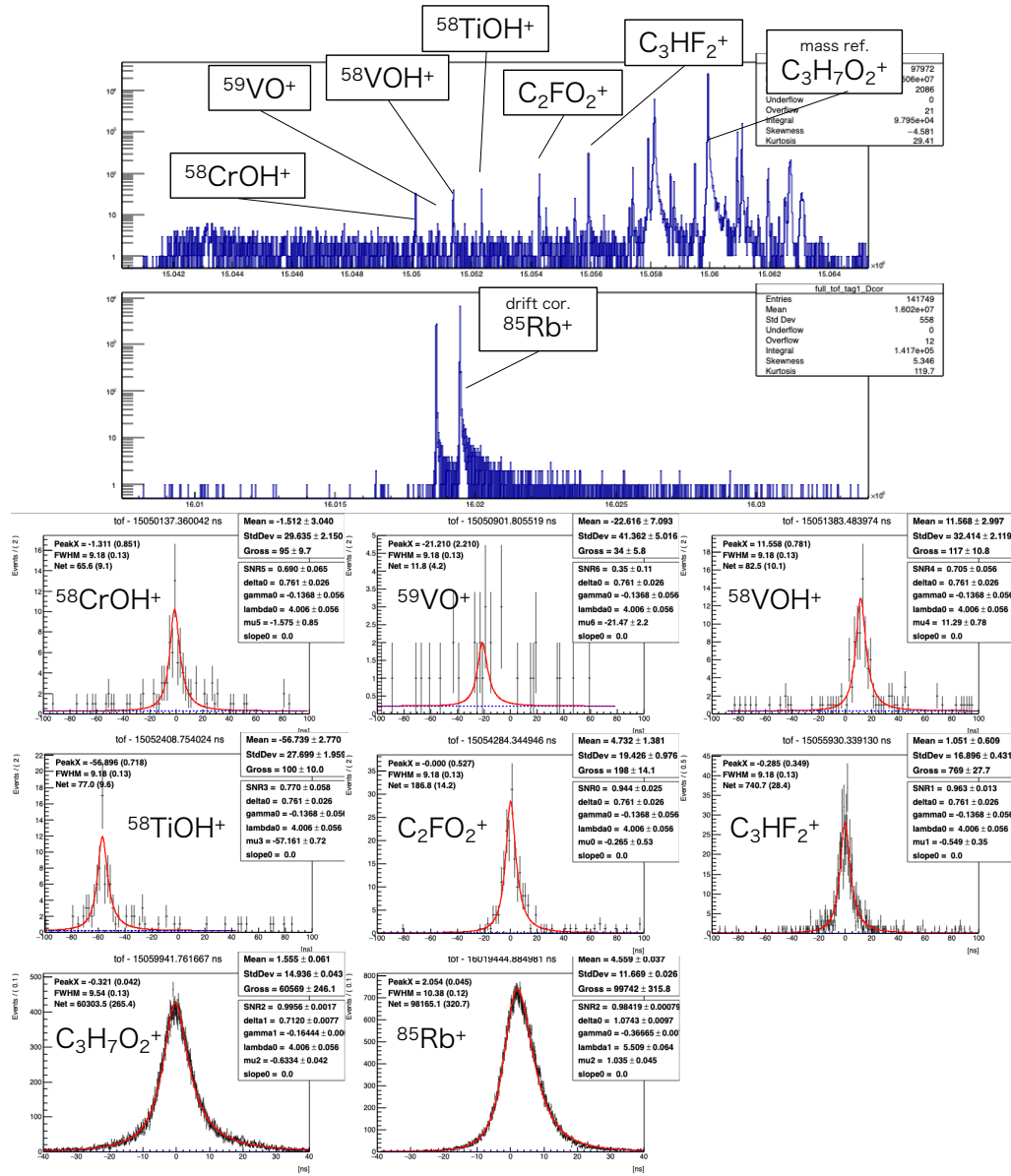
Figure A.3. TOF full spectrum obtained in the online experiment (upper panel). Fitting results of all peaks (lower panel).

Figure A.4. TOF full spectrum obtained in the online experiment (upper panel). Fitting results of all peaks (lower panel).

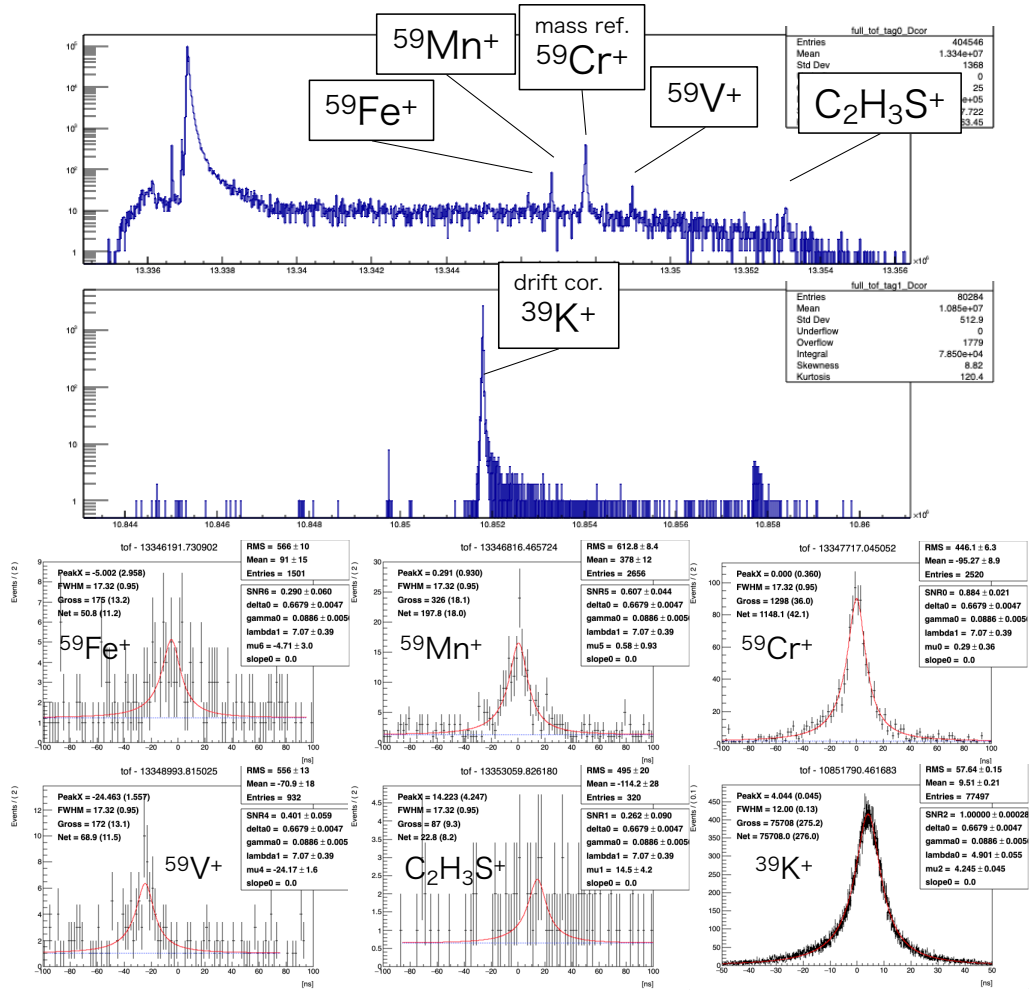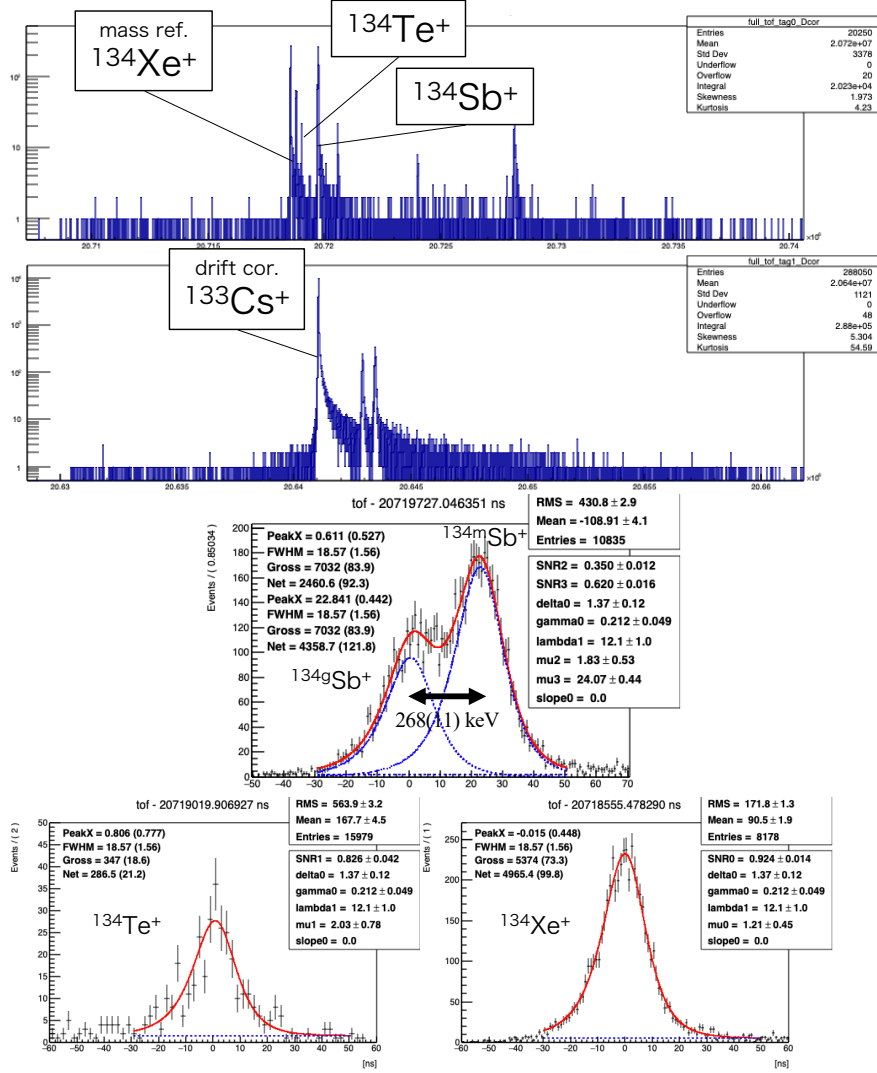**Figure A.5.** TOF full spectrum obtained in the online experiment (upper panel). Fitting results of all peaks (lower panel). The separation of the ground state and the isomeric states of ^{134g,m}Sb has been demonstrated reaching a resolving power of $R_m = 550k$ at that time.

One of the runs during the beam of mass number $A = 130\text{-}140$ region. Our ZD-MRTOF has succeeded in isomer separation (Fig. A.5). The literature value for the excitation energy of the isomeric state is 279(1) keV [21NN].

After extensive mirror potential tuning in off-line tests, we achieved a mass resolving power of 1.2 million. Drift corrections and peak fitting have been performed using a new analysis method introduced in this paper.
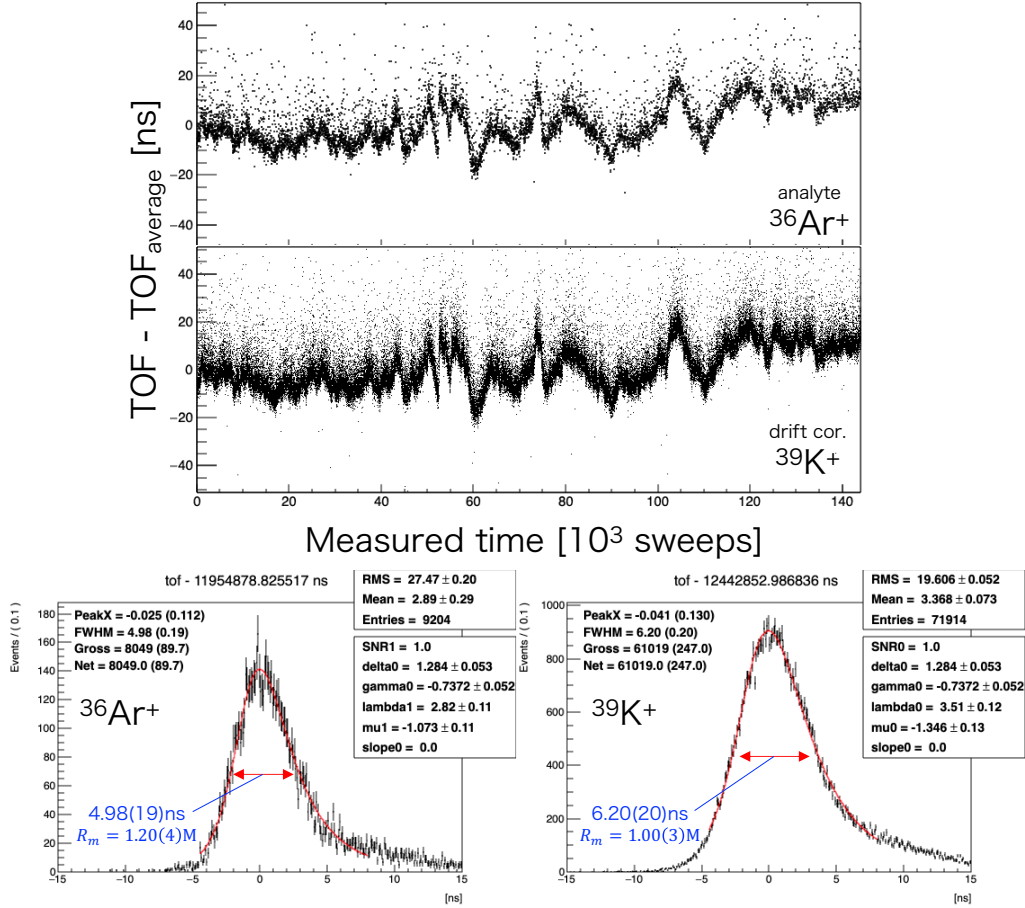

Figure A.6. TOF Spectra with the highest mass resolution ever achieved in the off-line experiment. Upper panel shows before drift correction, lower panel are fitting results of two peaks after drift correction.

Reference

[19As]   F. W. Aston, *Philos. Mag.* **38** 707 (1919).

[35We]   C. F. v. Weizsäcker, *Zeitschrift für Physik* **96** 431 (1935).

[49Jo]   N. L. Johnson, *Systems of Frequency Curves Generated by Methods of Translation.* Biometrika **36(1/2)**, 149–176 (1949).

[49Ma]   M. Goeppert Mayer. "On Closed Shells in Nuclei. II" *Phys. Rev.* **75** (1949).

[55MJ]   M. Goeppert-Mayer, and J. Jensen, *Elementary theory of nuclear shell structure*, New York, Wiley, 237, (1955).

[67De]   H.G. Dehmelt, *Radiofrequency spectroscopy of stored ions—I: Storage, Adv. At. Mol. Phys.* **3** 53 (1967).

[75Hu]   J. Hufner *et al.*, *Physical Review C*, **12**(6) 1888 (1975).

[85Hu]   A. Huck *et al.*, *Phys. Rev. C* **31**, 2226 (1985).

[85Wo]   J. M. Wouters et al., *Nucl. Instrum. Methods* A **240**, 77 (1985).

[87Fr]   B. Franzke, *Nucl. Instrum. Methods Phys. Res.* B **24/25** 18 (1987).

[89Mo]   D. Morrissey, *Physical Review C*, **39**(2) 460 (1989).

[90Ca]   R.F. Casten, *Nuclear Structure from a Simple Perspective*, Oxford University Press, (1990).

[90Tu]   X.L. Tu, X.G. Zhou, D.J. Vieira, J.M. Wouters, Z.Y. Zhou, H.L. Seifert, and V.G. Lind, *Z. Phys. A- Atomic Nuclei* **337**, 361-366 (1990).

[90Wa]   E. K. Warburton, J. A. Becker, and B. A. Brown, *Phys. Rev. C* **41**, 1147 (1990).

[90Wo]   H. Wollnik and M. Przewloka, *International Journal of Mass Spectrometry and Ion Processes* (1990).

[91Ga]   J. Gaimard and K. Schmidt, *Nuclear Physics A*, **531**(3) 709–745 (1991).

[94Se]   H.L. Seifert, J.M. Wouters, D.J. Vieira, H. Wollnik, X.G. Zhou, X.L. Tu, Z.Y. Zhou, G.W. Butler, *Z. Phys. A* **349**, 25-32 (1994).

[95Ge]   H. Geissel *et al.*, *Annual Review of Nuclear and Particle Science* **45**, 163-203 (1995).

[95Gr]   R. Grzywacz *et al.*, *Phys. Lett.* **B 355**, 439 (1995).

[96Bo]   G. Bollen *et al.*, *Nucl. Instrum. Methods Phys. Res.* A **368** 675 (1996).

[97Be]   M. Bernas et al., *Phys. Lett.* **B 415**, 111 (1997).

[97Br]   R. Brun and F. Rademakers, *ROOT: An object oriented data analysis framework, Nucl. Instrum. Methods Phys. Res.* **A389** (1997) 81.

[97Mi]   W. Mittig *et al.*, *Annual Review of Nuclear and Particle Science*, **47**(1) 27– 66 (1997).

[97Sa]   G. Savard *et al.*, *Nucl. Phys.* A **626** 353 (1997).

[98Ba]   Y. Bai, D.J. Vieira, H.L. Seifert, and J.M. Wouters, *AIP Conference Proceedings* **455**, 90 (1998).

[98Mu]   G. Munzenberg, *PHILOSOPHICAL TRANSACTIONS-ROYAL SOCIETY OF LONDON SERIES A MATHEMATICAL PHYSICAL AND ENGINEERING SCIENCES*, pages 2083–2104 (1998).

[98Sa]   W. Satuła, J. Dobaczewski, and W. Nazarewicz, *Physical Review Letters* **81**, 3599 (1998).

[99Ha]   M. Hannawald *et al., Phys. Rev. Lett.* **82** 1931 (1999).

[00Ha]   M. Hausmann *et al.*, *Nucl. Instrum. Methods Phys. Res.* A **446** 569 (2000).

[01Pr]   J. I. Prisciandaro *et al.*, *Physics Letters B* **510.1** 17 (2001).

[01Sa]   H. Savajols, *Atomic Physics at Accelerators: Mass Spectrometry*, 245 (2001).

[02Hi]   S. Hilaire *et al.*, *Physics Letters* B **531** 61 (2002).

[03Ko]   V. S. Kolhinen *et al.*, *Nucl. Instrum. Methods Phys. Res.* B **204** 502 (2003).

[03Ma]   P. F. Mantica *et al., Phys. Rev. C* **67** 014311 (2003).

[03Ma]   P. F. Mantica *et al., Phys. Rev. C* **68** 044311 (2003).

[03Sc]   S. Schwarz *et al.*, *Nucl. Instrum. Methods Phys. Res.* B **204** 507 (2003).

[03Si]   G. Sikler *et al.*, *Nucl. Instrum. Methods Phys. Res.* B **204** 482 (2003).

[03So]   O. Sorlin *et al., Eur. Phys. J. A* **16** 55 (2003).

[03Ve]   W. Verkerke and D.P. Kirkby, *The RooFit toolkit for data modeling, econf* **C0303241** (2003) MOLT007.

[03Wo]   H. Wollnik and A. Casares, *International Journal of Mass Spectrometry* **227** 217 (2003).

[04Li]   S. N. Liddick *et al., Phys. Rev. C* **70** 064303 (2004).

[04Ma]   M. Matos, Thesis, Giessen (2004).

[05Ko]   H. Koura, T. Tachibana, M. Uno and M. Yamada, *Prog. Theor. Phys.* **113** 305 (2005).

[05Li]   Yu. A. Litvnov *et al.*, *Nuclear Physics* A **756** 3 (2005).

[05Ta]   A. Takamine, *et al.*, *Review of Scientific Instruments* **76**, 103503 (2005).

[06De]   P. Dendooven et al., NIM A **558** 580 (2006).

[07Ba]   B. Bastin *et al.*, *Phys. Rev. Lett.* **99**, 022503 (2007).

[08Ad]   P. Adrich *et al., Phys. Rev. C* **77** 054306 (2008).

[08Oh]   T. Ohnishi et al., *J. Phys. Soc. Jpn.* **77**, 083201 (2008).

[08Ta]   O.B. Tarasov, D. Bazin, *Nucl. Inst. Meth.* B **266** 4657 (2008).

[09Ao] N. Aoi *et al., Phys. Rev. Lett.* **102** 012502 (2009).

[09Wa] M. Wang *et al.*, *In: Int. J. Mod. Phys.* E **18** 352 (2009).

[09We] R. Wester, *J. Phys. B: At. Mol. Opt. Phys.* **42** 154001 (2009).

[10Lj] J. Ljungvall *et al., Phys. Rev. C* **81** 061301(R) (2010).

[10Oh] T. Ohnishi et al., *J. Phys. Soc. Jpn.* **79**, 073201 (2010).

[11Sc] S. Schwarz, *International Journal of Mass Spectrometry* **299** 71 (2011).

[11Sh] K. Shibata *et al.*, *"JENDL-4.0: A New Library for Nuclear Science and Engineering," J. Nucl. Sci. Technol.*, **48**, 1 (2011).

[12Do] P. Doornenbal, *Progress of Theoretical and Experimental Physics 2012* (2012).

[12Ku] T. Kubo et al., *Prog. Theor. Exp. Phys.*, 03C003 (2012).

[12Na] S. Naimi *et al., Phys. Rev. C* **86** 014325 (2012).

[12Ue] T. Uesaka, S. Shimoura, and H. Sakai, *Prog. Theor. Exp. Phys.* **2012**, 03C007 (2012).

[12Wo] R. N. Wolf *et al.*, *Nucl. Instrum. Methods Phys. Res.* A **686** 82 (2012).

[13Cr] H. L. Crawford *et al., Phys. Rev. Lett.* **110** 242701 (2013).

[13It] Y. Ito et al., *Physical Review* C **88** 011306 (2013).

[13Pl] W. R. Plaß, T. Dickel, and C. Scheidenberger, *International Journal of Mass Spectrometry* **349-350**.1 134 (2013).

[13St] D. Steppenbeck *et al.*, *Nature* (London) **502**, 207 (2013).

[13Ya] Y. Yamaguchi et al., *Nucl. Instrum. Methods Phys. Res.* B **317** 629 (2013).

[14Sc] P. Schury *et al.*, *International Journal of Mass Spectrometry* **359**.19 (2014).

[15Di] T. Dickel *et al.*, *Nucl. Instrum. Methods Phys. Res.* A **777** 172 (2015).

[15Ro] M. Rosenbusch *et al.*, *Phys. Rev. Lett.* **114** 202501 (2015).

[15St] D. Steppenbeck *et al.*, *Phys. Rev. Lett.* **114** 252501 (2015).

[15Xu] X. Xu *et al.*, *Chinese Physics C* **39**, 104001 (2015).

[16Do] P. Doornenbal, *AIP Conf. Proc.* **1753**, 070002 (2016).

[16Hi] T. Hirsh *et al.*, *Nucl. Instrum. Methods Phys. Res.* B **376** 229 (2016).

[16Me] Z. Meisel *et al., Phys. Rev. C* **93** 035805 (2016).

[16My] Edmund G. Myers, *Nature Physics* 12 986 (2016).

[17Sc] P. Schury *et al.*, *Nucl. Instrum. Methods* B **407**, 160 (2017).

[17St] D. Steppenbeck *et al.*, *Physical Review C* **96** 064310 (2017).

[18Do] P. Doornenbal *et al.*, *RIKEN RIBF proposal* Np1812-ribf173 (2018).

[18Mi] S. Michimasa *et al.*, *Physical Review Letters* **121**, 022506 (2018).

[18Mo]   M. Mougeot *et al.*, *Physical Review Letters* **120**, 232501 (2018).

[19An]   S. Ayet San Andr′es *et al.*, *Phys. Rev.* C **99** 064313 (2019).

[19Lo]   K. Lodders, arXiv:1912.00844 (2019).

[19Ma]   Na-Na Ma *et al.*, *Chinese Phys. C* **43** 044105 (2019).

[19Ta]   A. Takamine *et al.*, *RIKEN Accel. Prog. Rep.* **52**, 139 (2019).

[20Ch]   S. Chen *et al.*, *RIKEN Accel. Prog. Rep.* **53** (2020).

[20Co]   M.L. Cortés *et al.*, *Physics Letters B* **800** 135071 (2020).

[20Me]   Z. Meisel *et al.*, *Physical Review C* **101**, 052801(R) (2020).

[20Mi]   S. Michimasa *et al.*, *Physical Review Letters* **125**, 122501 (2020).

[20Pe]   H. Penttil̈a *et al.*, *EPJ Web Conf.* **239** 17002 (2020).

[20Ro]   M. Rosenbusch *et al.*, *International Journal of Mass Spectrometry* **456**.116346 (2020).

[20Ta]   A.Takamine *et al.*, *RIKEN Accel. Prog. Rep.* **53** (2020).

[21Du]   E. Dunling, Thesis, York (2021).

[21Hu]   W.J. Huang, Meng Wang, F.G. Kondev, G. Audi, and S. Naimi, *Chinese Physics C* **45**, 030002 (2021).

[21Le]   E. Leistenschneider *et al.*, *Physical Review Letters* **126**, 042501 (2021).

[21NN]   NNDC On-Line Data Service from the ENSDF database.

[21Ro]   M. Rosenbusch *et al.*, *RIKEN Acc. Prog. Rep.* **55** (2021).

[21St]   S. R. Stroberg, J. D. Holt, A. Schwenk, and J. Simonis, *Physical Review Letters* **126**, 022501 (2021).

[21Wi]   K. Wimmer *et al.*, *RIKEN Acc. Prog. Rep.* **54** (2021).

[22Ro]   M. Rosenbusch *et al*., arXiv:2110.11507 (2022).